

# Statistical Analysis and Computer Modeling of Volcanic Eruptions

(Thesis format: Integrated Article)

by

Laura A. Sanchez

Graduate Program  
in  
Geophysics  
Earth Sciences

A thesis submitted in partial fulfillment  
of the requirements for the degree of  
Doctor of Philosophy

School of Graduate and Postdoctoral Studies  
The University of Western Ontario  
London, Ontario, Canada

© Laura A. Sanchez 2014

# Abstract

Volcanism is an important mechanism by which internal heat is transported to the Earth's surface and volcanic eruptions are the results of the dynamics of a complex system and are characterized by non-trivial temporal correlations. Understanding the processes involved in volcano formation and magma ascent are crucial to develop better hazard assessment techniques. This study focuses on three main points: understanding caldera and impact crater formation in the solar system, investigating the global temporal behavior of volcanic eruptions and understanding the nonlinear interactions taking place in the solid crust which lead to an eruption.

In chapter 2, I first examine the distribution of caldera diameters on Earth, Mars, Io and Venus by performing a scaling analysis using the mean caldera diameter as a scaling factor. I find that their probability densities can be described by a universal distribution that can be approximated by a Generalized Extreme Value distribution. This scaling implies that a similar process governs caldera formation throughout the solar system. In chapter 3, I investigate the size distribution of impact craters on Earth, Mars, Venus, Mercury and the Moon. Similarly to calderas, I observe a collapse of the distributions when rescaled using the mean diameter of each planetary body, implying common formation and evolution mechanisms.

In chapter 4, I investigate the distribution of interevent times between eruptions for active volcanoes on Earth. When rescaling the axis using the mean rate of volcanism, the distributions collapse into a single one, the log-normal distribution. This scaling implies that the processes governing volcanic eruptions on Earth are similar and are independent of the type of volcanism and location, which emphasizes the importance of studying volcanism by modeling a universal behavior.

In the last chapter, I take a modeling approach to study the interactions between the magma and the crust. I define a lattice gas cellular automata model where the magma is represented by discrete particles. In this model, magma propagates

through the crust and fracturing occurs until it reaches the top of the crust and an eruption or a cascade of eruptions occur. I study the statistical behavior of eruptions in the model and observe similar size and temporal behaviors that have been observed on active volcanoes.

**Keywords:** Statistical analysis, scaling, planetary calderas, impact craters, volcanic eruptions, cellular automata

## Co-Authorship Statement

This thesis is prepared in an integrated-article format and the following manuscripts were written by Laura Sanchez.

1. Sanchez, L. and Shcherbakov, R. (2012), Scaling properties of planetary calderas and terrestrial volcanic eruptions, *Nonlin. Proc. Geophys.*, *19(6):585-593*
2. Sanchez, L. and Shcherbakov, R. (2014), Statistical Analysis of the Size Distribution of Impact Craters, *submitted to Earth and Planetary Science Letters*
3. Sanchez, L. and Shcherbakov, R. (2012), Temporal Scaling of Volcanic Eruptions, *J. Volcanol. Geotherm. Res.*, *247-248:115121, 2012*
4. Sanchez, L. and Shcherbakov, R., A Cellular Automata to Model Magma-Crust Interactions and Volcanic Eruptions, *to be submitted*

The data collection and analysis was performed by Laura Sanchez for manuscripts 1, 2 and 3. The design of the model for manuscript 4 was done with Dr. Robert Shcherbakov. The work for these manuscripts was done under the supervision of Dr. Robert Shcherbakov with financial support from the NSERC.

## Acknowledgements

First, I would like express my deep appreciation to my supervisor Dr. Robert Shcherbakov. I am very grateful to have been part of his research group and I would like to thank him for his guidance, availability and patience with me during my PhD.

I would also like to express my gratitude to my committee members Dr. Gail Atkinson and Dr. Kristy Tiampo for their time and motivational words. I would also like to thank my examiners Dr. Gordon Osinski, Dr. Jean-Robert Grasso and Dr. M. Van De Wiel for taking the time out of their busy schedules to read and analyze my thesis.

I would have never been able to finish this endeavor without the precious help and support of the department staff members Marie Schell, Margaret Moulton, Katherine Johnson and Kevin Jordan. For all their advice and kind words, I am grateful.

I would like to thank my many reviewers who improved this thesis with every edit: Alexandra Pontefract, Marie Burford, Scott Colborne, Rachel Schwartz-Narbonne, Cassandra Marion, Jessica Stromberg. Your expertise of the English language was greatly appreciated!

For the stimulating discussions, I thank Dr. Pablo Gonzalez, Nelson Cho, Pathikrit Bhattacharya and David Edey. And for the general support, all my colleagues from office 1031, Andrea Prentice, Lola Wong (for introducing me to the pomodoro technique), Caitlin Atkinson, Meagan Pyper, Sonja Leal and all those I may have forgotten (you know who you are).

Lastly, I would like to thank my parents Irene and Pierre for their never failing support. I could never thank you enough for all the help you provided.

# Table of Contents

<b>Abstract</b> . . . . .	<b>ii</b>
<b>Co-Authorship Statement</b> . . . . .	<b>iv</b>
<b>Acknowledgements</b> . . . . .	<b>v</b>
<b>List of tables</b> . . . . .	<b>viii</b>
<b>List of figures</b> . . . . .	<b>x</b>
<b>1 Introduction</b> . . . . .	<b>1</b>
1.1 Preamble . . . . .	1
1.2 Overview of Volcanism . . . . .	3
1.2.1 Planetary Volcanism . . . . .	3
1.2.2 Terrestrial Volcanism . . . . .	5
1.3 Statistical Modeling of Volcanic Processes . . . . .	10
1.4 Modeling of Volcanic Processes . . . . .	15
1.4.1 Numerical Models . . . . .	16
1.4.2 Cellular Automata Models . . . . .	18
1.5 Thesis Outline . . . . .	22
1.5.1 Chapter 2: Scaling Properties of Planetary Calderas . . . . .	22
1.5.2 Chapter 3: Statistical Analysis of the Size Distribution of Impact Craters in the Solar System . . . . .	23
1.5.3 Chapter 4: Temporal Scaling of Volcanic Eruptions . . . . .	23
1.5.4 Chapter 5: A Cellular Automata to Model Magma/Crust Interactions and Volcanic Eruptions . . . . .	24
References . . . . .	25
<b>2 Scaling Properties of Planetary Calderas</b> . . . . .	<b>34</b>
2.1 Introduction . . . . .	34
2.2 Solar System Bodies . . . . .	37
2.3 The Earth . . . . .	43
2.4 Conclusions . . . . .	45
References . . . . .	46

*Table of Contents*

---

<b>3</b>	<b>Statistical Analysis of the Size Distribution of Impact Craters . . .</b>	<b>49</b>
3.1	Introduction . . . . .	49
3.2	Scaling Analysis . . . . .	53
3.3	Conclusions . . . . .	61
	References . . . . .	63
<b>4</b>	<b>Temporal Scaling of Volcanic Eruptions . . . . .</b>	<b>66</b>
4.1	Introduction . . . . .	66
4.2	Volcanic Eruption Data . . . . .	68
4.3	Results and interpretation . . . . .	70
4.4	Conclusions . . . . .	81
	References . . . . .	83
<b>5</b>	<b>A Cellular Automata to Model Magma-Crust Interactions and Vol-</b>	
	<b>canic Eruptions . . . . .</b>	<b>86</b>
5.1	Introduction . . . . .	86
5.2	The Model . . . . .	89
5.3	Results . . . . .	93
	5.3.1 Model 1 ( $300 \times 110$ ) . . . . .	94
	5.3.2 Model 2 ( $256 \times 256$ ) . . . . .	104
	5.3.3 Temporal behavior, eruption duration . . . . .	116
5.4	Conclusions . . . . .	122
	References . . . . .	124
<b>6</b>	<b>Discussion and Concluding Remarks . . . . .</b>	<b>128</b>
6.1	Landform formation in the solar system . . . . .	129
6.2	Temporal behavior of volcanic eruptions on Earth . . . . .	130
6.3	Modeling of volcanic eruptions . . . . .	131
6.4	Future work . . . . .	131
	References . . . . .	133

**Appendices**

<b>A</b>	<b>Tables of Volcanic Eruptions Time Series . . . . .</b>	<b>135</b>
<b>B</b>	<b>Curriculum Vitae . . . . .</b>	<b>142</b>

# List of Tables

2.1	Summary of the data used for the planetary caldera analysis. $D_n$ is the mean diameter and $A_n$ is the mean caldera area computed from the minimum and maximum diameters assuming an elliptic shape for each planetary body except for the Earth where some caldera areas are estimated using the actual shape [Geyer and Marti, 2008]. The errors are given at 95% confidence intervals. . . . .	41
2.2	The maximum values of the log-likelihood function ( $\ln L$ ) and the corresponding values of the Akaike Information Criterion (AIC) for the model distribution functions considered to fit the rescaled distributions given in Figure 2.2a. . . . .	41
2.3	The maximum values of the log-likelihood function ( $\ln L$ ) and the corresponding values of the AIC for the model distribution functions considered to fit a) the rescaled distributions given in Figure 2.2b and b) the rescaled distributions given in Figure 2.4. $k$ is the number of parameters for the considered distribution. The values correspond to the fitting analysis considering only calderas/paterae with an area above 30 km <sup>2</sup> . . . . .	41
3.1	Summary of the data used for the planetary impact crater analysis. $D_n$ is the mean diameter, $\text{Min}_n$ and $\text{Max}_n$ are the smallest and largest diameters respectively. The errors on the mean are given at 95% confidence intervals.	60
3.2	The maximum values of the log-likelihood function ( $\ln L$ ) and the corresponding values of the Akaike Information Criterion (AIC) for the model distribution functions considered to fit the rescaled distributions given in Figure 3.4 . . . . .	60
3.3	The maximum values of the log-likelihood function ( $\ln L$ ) and the corresponding values of the Akaike Information Criterion (AIC) for the model distribution functions considered to fit the rescaled distributions given in Figure 3.5 . . . . .	60
4.1	Summary of the eruption data used for the interevent time analysis of 26 prominent volcanoes. $\tau_n$ is the mean interevent time between eruptions computed for each volcanic data set. The last column gives the time span of the eruption history considered for each volcano. The errors are given at 95% confidence intervals . . . . .	71
4.2	Summary of the eruption data used for the interevent time analysis for the volcano types . . . . .	72



4.3	The maximum values of the log-likelihood function ( $\ln L$ ) and the corresponding values of the Akaike Information Criterion (AIC) for the model distribution functions considered to fit a) the rescaled distributions given in Fig. (4.2), b) the rescaled distributions given in Fig. (4.3) and c) the rescaled distributions given in Fig. (4.4). $k$ is the number of parameters for the considered distribution . . . . .	80
A.1	Summary of the eruption data used for the interevent time analysis for the world regions . . . . .	135
A.2	Summary of the data used for the Alaska region with the number of eruptions, the time span, the mean interevent time and the type of volcano. . . . .	135
A.3	Summary of the data used for the Aleutian islands with the number of eruptions, the time span, the mean interevent time and the type of volcano. . . . .	136
A.4	Summary of the data used for Central America with the number of eruptions, the time span, the mean interevent time and the type of volcano. . . . .	136
A.5	Summary of the data used for Iceland with the number of eruptions, the time span, the mean interevent time and the type of volcano. . .	137
A.6	Summary of the data used for Indonesia with the number of eruptions, the time span, the mean interevent time and the type of volcano. . .	138
A.7	Summary of the data used for Japan with the number of eruptions, the time span, the mean interevent time and the type of volcano. . .	139
A.8	Summary of the data used for Kamchatka with the number of eruptions, the time span, the mean interevent time and the type of volcano.	139
A.9	Summary of the data used for New Zealand with the number of eruptions, the time span, the mean interevent time and the type of volcano.	140
A.10	Summary of the data used for South America with the number of eruptions, the time span, the mean interevent time and the type of volcano. . . . .	140
A.11	Summary of the data used for the eruption of major calderas on Earth with the number of eruptions, the time span and the mean interevent time. . . . .	141

# List of Figures

1.1	Simplified map presenting the location of major cities, earthquakes and volcanoes. (modified after <a href="http://www.USGS.gov">www.USGS.gov</a> ) . . . . .	2
1.2	Sketch of the magma plumbing system. The magma chamber is located at a depth $H$ from the surface and the pressure within the chamber is a combination of the pressure due to the host rock $P_1(H)$ and the overpressure generated by the input of magma or the increase in gas content in the chamber $\Delta P_c$ . The eruption exit pressure is a combination of the atmospheric pressure $P_a$ and the excess pressure in the vent $\Delta P_e$ . The lithostatic pressure around the chamber $P_L(z)$ is a function of depth and the density of the host rock $\rho_r$ [Jaupart, 2000]. . . . .	7
1.3	Schematic steps of the use of experimental and numerical/mathematical modeling to validate hypotheses on volcanic processes . . . . .	16
1.4	Example of the evolution of the Wolfram CA from rule 30. The upper part displays the evolution rules for each possible configuration at time $t$ (from <a href="http://www.mathworld.wolfram.com">www.mathworld.wolfram.com</a> ) . . . . .	19
2.1	Distributions of caldera sizes for the Earth, Venus, Mars and Io. a) Caldera diameters in km, b) Caldera areas in km <sup>2</sup> . . . . .	39
2.2	Rescaled caldera/paterae distributions for Earth, Mars, Venus and Io according to Eq. (2.1): a) rescaled diameters, with the mean diameter $D_n$ computed for each planetary body (Table 2.1). The solid curve is a fit to the rescaled distributions and is given by the GEV distribution, Eq. (2.2), with $\theta = 0.22 \pm 0.06$ , $\mu = 0.64 \pm 0.04$ , and $\sigma = 0.42 \pm 0.03$ ; b) rescaled areas, with the mean area $A_n$ computed for each planetary body (Table 2.1). The solid curve is a fit to the rescaled distributions and is given by the GEV distribution, Eq. (2.2), with $\theta = 0.84 \pm 0.11$ , $\mu = 0.26 \pm 0.03$ , and $\sigma = 0.30 \pm 0.03$ . . . . .	42
2.3	Probability density functions of caldera areas for three separate crustal types on Earth. . . . .	44
2.4	Rescaled caldera areas distributions for the three crustal types according to Eq. (2.1) with the mean area $A_n$ computed for each crustal type (Table 2.1). The solid curve is a fit to the rescaled distributions and is given by the GEV distribution, Eq. (2.2), with $\theta = 0.94 \pm 0.16$ , $\mu = 0.22 \pm 0.04$ , and $\sigma = 0.28 \pm 0.05$ . . . . .	44

3.1	Distributions of crater diameters in km for Mars, Mercury, the Moon, Venus and Earth. . . . .	54
3.2	Rescaled distributions of crater diameters according to Eq. (3.1), with $D_n$ computed for each planetary body (see Table 3.1). . . . .	55
3.3	Distributions of crater diameters in km for Mars, Mercury, the Moon, Venus and Earth after size cutoff. . . . .	57
3.4	Rescaled distributions of crater diameters according to Eq. (3.1), with given size cutoff. The solid black curve is a fit to the rescaled distributions and is given by the log-normal distribution, Eq. (3.3), with $\mu = -0.23 \pm 0.03$ and $\sigma = 0.67 \pm 0.02$ . The solid red curve is a fit to the rescaled distribution and is given by the GEV distribution, Eq. (3.4), with $\theta = 0.25 \pm 0.04$ , $\mu = 0.65 \pm 0.02$ , and $\sigma = 0.40 \pm 0.02$ . . . . .	58
3.5	Rescaled distributions of crater diameters for Mars, Mercury, the Moon and Venus according to Eq. 3.1. The solid black curve is a fit to the rescaled distributions and is given by the GEV distribution, Eq. (3.4), with $\theta = 0.51 \pm 0.08$ , $\mu = 0.78 \pm 0.01$ , and $\sigma = 0.17 \pm 0.01$ . . . . .	59
4.1	Probability density functions of interevent times for the 26 volcanoes on Earth with the largest eruptive history . . . . .	72
4.2	Rescaled interevent time distributions for the 26 individual active volcanoes according to Eq. (4.1) with the mean interevent time $\tau_n$ computed for each volcano (Table 4.1). The solid curve is a fit to the rescaled distributions and is given by the log-normal distribution, Eq. (4.2), with $\mu = -0.66 \pm 0.05$ and $\sigma = 1.14 \pm 0.04$ . The errors on the parameters are given at the 95% confidence interval assuming a log-normal distribution. The error bars are not displayed for the sake of clarity . . . . .	73
4.3	The combined rescaled interevent time distributions of groups of volcanoes belonging to 9 different regions. Each individual volcano sequence was first rescaled with the mean interevent time and only after that the distributions were constructed. Data collapse was observed similar to the one shown in Figure 4.2. The solid curve is a fit to the rescaled distributions and is given by the log-normal distribution with $\mu = -0.70 \pm 0.05$ and $\sigma = 1.23 \pm 0.03$ . The errors on the parameters are given at the 95% confidence interval assuming a log-normal distribution . . . . .	74
4.4	The combined rescaled interevent time distributions of volcanoes grouped by type. Each individual volcano sequence was first rescaled with the mean interevent time and only after that the distributions were constructed. Data collapse was observed similar to the one shown in Figure 4.2. The solid curve is a fit to the rescaled distributions and is given by the log-normal distribution with $\mu = -0.70 \pm 0.04$ and $\sigma = 1.24 \pm 0.03$ . The errors on the parameters are given at the 95% confidence interval assuming a log-normal distribution . . . . .	75

4.5	The combined rescaled interevent time distributions of groups of volcanoes belonging to different regions. Each individual volcano sequence was first rescaled with the mean interevent time and only after that the distributions were constructed. The lower magnitude cutoff of eruptions was used: a) $VEI \geq 1.0$ ; b) $VEI \geq 2.0$ ; c) $VEI \geq 3.0$ . The solid curve is a fit to the rescaled distributions and is given by the log-normal distribution with a) $\mu = -0.70 \pm 0.05$ and $\sigma = 1.23 \pm 0.04$ ; b) $\mu = -0.67 \pm 0.06$ and $\sigma = 1.22 \pm 0.04$ ; c) $\mu = -0.59 \pm 0.15$ and $\sigma = 1.27 \pm 0.11$ . The errors on the parameters are given at the 95% confidence interval assuming a log-normal distribution. The error bars are not displayed for the sake of clarity . . . . .	76
4.5	Continued. . . . .	77
4.5	Continued. . . . .	77
4.6	Rescaled interevent time distributions for the 26 individual volcanoes according to Eq. (1) with the mean interevent time $\tau_n$ for each volcano. Lower magnitude cutoffs of eruptions were used: a) $VEI \geq 1.0$ ; b) $VEI \geq 2.0$ . The solid curve is a fit to the rescaled distributions by the log-normal distribution with a) $\mu = -0.68 \pm 0.08$ and $\sigma = 1.20 \pm 0.06$ ; b) $\mu = -0.68 \pm 0.07$ and $\sigma = 1.18 \pm 0.06$ . . . . .	78
4.2	Continued. . . . .	79
5.1	Different possible configurations for particle positions in the HPP model for the cases of 4, 3 and 2 particles on a node (a,b,c,d). Schematic view of the 2D lattice with the distinction between the magma chamber and the crust (e)	91
5.2	Collision and propagation rules for the different configuration of particles on the lattice . . . . .	92
5.3	Propagation directions for model 1 (left) and model 2 (right). . . . .	93
5.4	Example of the frequency-size distribution of eruptions for $d = 0.08$ and $h = 0.04$ . We note the peak at $3 \times 10^4$ . . . . .	95
5.5	Truncated power-law fit of the frequency-size distribution for the size range $V \in [30, 1000]$ with $\alpha = 1.36 \pm 0.03$ . . . . .	95
5.6	Frequency-size distributions of eruptions for $d = 0.5$ and $h = 0.2$ and varying thickness of the system. . . . .	96
5.7	Variation of the power-law exponent $\alpha$ with $h$ for small values of $d$ . . . . .	97
5.8	Variation of the power-law exponent $\alpha$ with $h$ for large values of $d$ (b). . . . .	98
5.9	Frequency size distributions of eruptions for $h = 0.5$ and large values of $d$ . . . . .	98
5.10	Truncated power-law fit of the frequency-size distribution for $d = 0.9$ and $h = 0.5$ for the size range $V \in [7, 100]$ with $\alpha = 4.36 \pm 0.72$ . . . . .	99
5.11	Example of the log-normal regime for the distribution of eruptions interevent times for $d = 0.5$ and $h = 0.2$ . . . . .	100
5.12	Truncated log-normal fit of the distribution for the time range $\tau \in [60, 300]$ with $\mu = 3.48 \pm 0.61$ and $\sigma = 0.54 \pm 0.14$ . . . . .	101

5.13	Example of the exponential regime for the distribution of eruptions interevent times for $d = 0.5$ and $h = 0.4$ . . . . .	101
5.14	Truncated exponential fit of the distribution for the time range $\tau \in [50, 200]$ with $\lambda = 26.27 \pm 2.11$ . . . . .	102
5.15	Example of the power-law regime for the distribution of eruptions interevent times for $d = 0.5$ and $h = 0.6$ . . . . .	102
5.16	Truncated power-law fit of the distribution for the time range $\tau \in [30, 300]$ with $\alpha = 1.51 \pm 0.05$ (b) . . . . .	103
5.17	Phase diagram representing the best model to describe the interevent data for varying values of $d$ and $h$ . . . . .	104
5.18	Truncated log-normal fit of the distribution for the size range $V \in [100, 10000]$ with $\mu = 3.52 \pm 0.58$ and $\sigma = 1.46 \pm 0.17$ (model 2) . . . . .	105
5.19	Truncated power-law fit of the distribution for the size range $V \in [100, 10000]$ with $\alpha = 1.96 \pm 0.03$ (model 2) . . . . .	106
5.20	Phase diagram representing the best model to describe the frequency-size distributions from model 2 for varying values of $d$ and $h$ . The label "other" corresponds to cases where the 3 distributions considered were not a good fit	106
5.21	Phase diagram representing variations in the $\mu$ parameter for the truncated log-normal fit of the size distribution of events for $C = 0.6$ . . . . .	107
5.22	Phase diagram representing variations in the $\sigma$ parameter for the truncated log-normal fit of the size distribution of events for $C = 0.6$ . . . . .	107
5.23	Phase diagram representing variations in the $\alpha$ parameter for the truncated power-law fit of the size distribution of events for $C = 0.6$ . . . . .	108
5.24	Phase diagram representing the best model to describe the frequency-size distributions from model 2 for varying values of $d$ and $h$ for $C = 0.55$ . . .	109
5.25	Phase diagram representing the best model to describe the frequency-size distributions from model 2 for varying values of $d$ and $h$ for $C = 0.65$ . . .	109
5.26	Truncated exponential fit of the distribution for the time range $\tau \in [300, 10000]$ with $\lambda = 215.4 \pm 11$ . . . . .	110
5.27	Truncated log-normal fit of the distribution for the time range $\tau \in [100, 10000]$ with $\mu = 3.53 \pm 0.22$ and $\sigma = 1.42 \pm 0.07$ . . . . .	110
5.28	Truncated power-law fit of the distribution for the time range $\tau \in [100, 10000]$ with $\alpha = 1.92 \pm 0.02$ . . . . .	111
5.29	Phase diagram representing the best model to describe the interevent distributions from model 2 for varying values of $d$ and $h$ for $C = 0.60$ . . . .	111
5.30	Phase diagram representing variations in the $\mu$ parameter for the truncated log-normal fit of the size distribution of events for $C = 0.6$ . . . . .	112
5.31	Phase diagram representing variations in the $\sigma$ parameter for the truncated log-normal fit of the size distribution of events for $C = 0.6$ . . . . .	113
5.32	Phase diagram representing variations in the $\lambda$ parameter for the truncated exponential fit of the size distribution of events for $C = 0.6$ . . . . .	113

5.33	Phase diagram representing variations in the $\alpha$ parameter for the truncated power-law fit of the size distribution of events for $C = 0.6$ . . . . .	114
5.34	Phase diagram representing the best model to describe the interevent distributions from model 2 for varying values of $d$ and $h$ for $C = 0.50$ . . . . .	114
5.35	Phase diagram representing the best model to describe the interevent distributions from model 2 for varying values of $d$ and $h$ for $C = 0.55$ . . . . .	115
5.36	Phase diagram representing the best model to describe the interevent distributions from model 2 for varying values of $d$ and $h$ for $C = 0.65$ . . . . .	115
5.37	Truncated exponential fit of the distribution for the time range $t \in [100, 10000]$ with $\lambda = 163.5 \pm 6.9$ . . . . .	117
5.38	Truncated log-normal fit of the distribution for the time range $t \in [100, 10000]$ with $\mu = 5.7 \pm 0.18$ and $\sigma = 0.81 \pm 0.13$ . . . . .	117
5.39	Truncated power-law fit of the distribution for the time range $t \in [200, 10000]$ with $\alpha = 4.23 \pm 0.75$ . . . . .	118
5.40	Phase diagram representing the best model to describe the duration distributions from model 2 for varying values of $d$ and $h$ for $C = 0.60$ . . . . .	118
5.41	Phase diagram representing variations in the $\mu$ parameter for the truncated log-normal fit of the distribution of durations for $C = 0.60$ . . . . .	119
5.42	Phase diagram representing variations in the $\sigma$ parameter for the truncated log-normal fit of the distribution of durations for $C = 0.60$ . . . . .	119
5.43	Phase diagram representing variations in the $\alpha$ parameter for the truncated power-law fit of the distribution of durations for $C = 0.60$ . . . . .	120
5.44	Phase diagram representing the best model to describe the duration distributions from model 2 for varying values of $d$ and $h$ for $C = 0.50$ . . . . .	120
5.45	Phase diagram representing the best model to describe the duration distributions from model 2 for varying values of $d$ and $h$ for $C = 0.55$ . . . . .	121
5.46	Phase diagram representing the best model to describe the duration distributions from model 2 for varying values of $d$ and $h$ for $C = 0.65$ . . . . .	121

# Chapter 1 Introduction

## 1.1 Preamble

Volcanic processes are the surface expression of a planetary body's internal activity. They constitute an efficient mechanism to dissipate internal heat. Volcanism is or was present on rocky planetary bodies in our solar system such as Earth, Mars, Venus, Mercury, the Moon, Io and several other planetary satellites [Wilson, 2009, Prockter et al., 2010]. On Earth, volcanic eruptions constitute a major natural hazard and with currently around 500 million people living in the vicinity of active volcanoes, the potential effects of an eruption on population and goods is becoming greater every day [Kusky, 2008] (Figure 1.1 shows a World map of the major cities and the location of volcanoes and earthquakes). Large explosive eruptions can have local effects such as land destruction through pyroclastic flows, but also global environmental effects through the dissemination of ashes and aerosols in the atmosphere from eruption plumes [Gilbert and Sparks, 1998].

Volcanoes are complex dynamical systems and the interactions between the magma and the host rock occurring within the edifice result in eruptions. These nonlinear interactions lead to the stochastic character of eruptions. Volcanic processes have been extensively studied through field and numerical analysis providing us with some quantitative understanding of the main physical mechanisms. However, our current knowledge remains insufficient to explain and forecast the temporal behavior of eruptions. The deterministic character of the modeling fails at reproducing the temporal patterns observed. Therefore, understanding the mechanisms responsible for volcano formation and the nonlinear interactions that lead to eruptions alongside with being able to reproduce the observed temporal patterns are crucial steps in the field of volcanology and hazard assessment.

This thesis focuses on three primary areas of concern:

- Understanding landform formation and evolution in the solar system using comparative planetology, with a focus on volcanic features and impact craters,

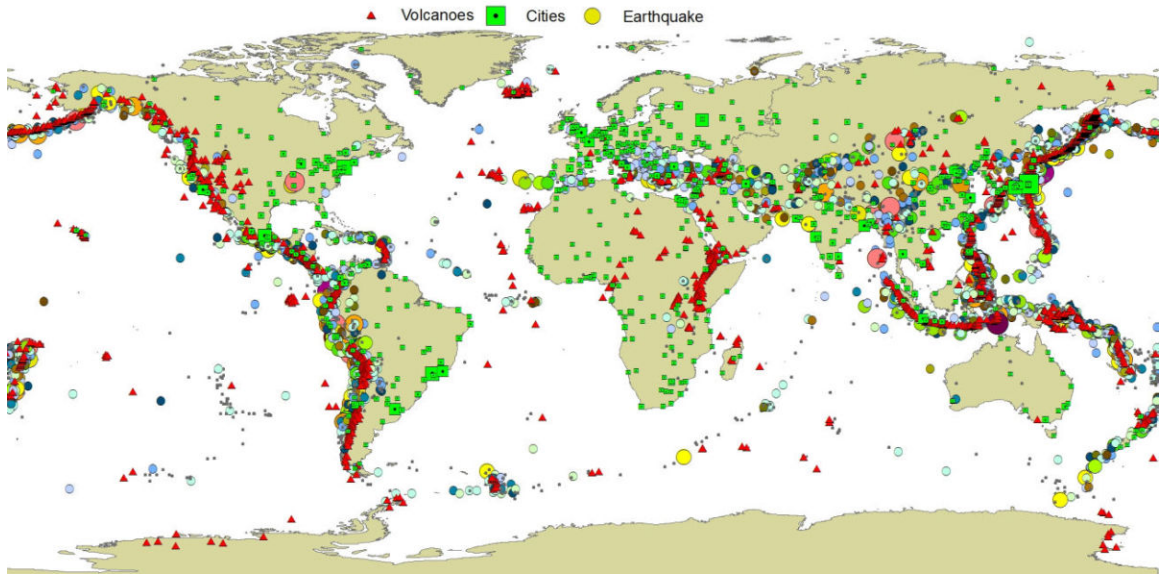


Figure 1.1: Simplified map presenting the location of major cities, earthquakes and volcanoes. (modified after [www.USGS.gov](http://www.USGS.gov))

- Investigating the global temporal behavior of volcanic eruptions on Earth,
- Understanding the nonlinear interactions taking place in the solid crust which lead to an eruption.

In order to investigate similarities in volcanic processes throughout the solar system, we compare the size distribution of volcanic features on Earth and other planetary bodies to infer common formation mechanisms. Particularly, we investigate the statistical properties of circular shaped depressions called calderas on Earth, Mars, Venus and Io. This type of feature is associated with the collapse of the volcanic edifice into a drained or partially drained magma chamber and can be used as a proxy to estimate the potential size of eruptions [Lipman, 2000]. Using the same statistical method, we also investigated the size distribution of impact craters in the solar system to further our understanding on formation and evolution mechanisms for planetary landforms.

The current knowledge on eruption processes, paired with the numerous monitoring tools available for volcano surveillance and historical records allow us to have access to a large wealth of data. Utilizing this data through statistical analysis is a powerful approach to determine temporal and spatial patterns in volcanic activ-



ity. This thesis relies on statistical approaches investigating the temporal behavior of eruptions throughout the World [Siebert and Simkin, 2002-].

Using a computer modeling approach, we study the complex magma/crust interactions in volcanic settings. More specifically, a cellular automaton model is used in order to reproduce the statistics observed in the empirical eruption data for volcanoes on Earth. The goal is to reproduce the statistical behavior of eruptions using the least amount of parameters to capture essential physical mechanisms of volcanic eruptions.

## 1.2 Overview of Volcanism

### 1.2.1 Planetary Volcanism

Volcanism is an inevitable consequence of planetary differentiation and crustal generation by magmatic processes. The heat present in the solar system planetary bodies is mostly generated by accretional energy and the decay of short and long lived radioactive nuclides. The release of planetary body's internal energy creates internal temperature gradients and allows for partial melting and the rise of hotter material towards the surface, which leads to volcanism. Tidal stresses induced on satellites by the presence of a large body is also considered a considerable source of heat that can enable volcanism. Space exploration has allowed remote access to most planetary bodies in our solar system. While it is difficult to make any kind of observations below the thick atmosphere of the gas giants, satellite observations from terrestrial planets have indicated the presence of radioactive elements. Planetary exploration has also directly shown that volcanism is or was operational on other solar system bodies such as the Moon, Venus, Mars, Mercury, Io, and several other planetary satellites [Wilson, 2009, Prockter et al., 2010]. Volcanic processes are therefore a typical heat dissipation mechanism on terrestrial planetary bodies. The resultant landforms depend on parameters such as the bulk chemistry of the parent magma, the nature of fractures and feeders and their study can lead to a better understanding of the planet's internal dynamics.

Volcanism on the Moon is mostly characterized by large basaltic flows called *mares*. In its early history, portions of the mantle experienced partial melting and the melt was lead to rise through cracks and fractures created by the large impact

craters and basins at the surface. The large flows filled those craters and ended up covering around 20% of the surface of the Moon [Spudis, 2000]. When smaller volumes of magma are involved in the eruptive processes, smaller volcanic features can form such as domes and cones. Their shape depends on the style and rate of eruption rather than on the magma composition [Head, 1976, Head and Gifford, 1980]. Some pyroclastic materials were collected from the surface of the Moon by the Apollo 15 and 17 missions, suggesting that some lava fountain type of eruptions may have occurred in the satellite's past [Spudis, 2000].

One of the solar system's planetary bodies that is the closest to the Earth as far as composition, density and size is Venus. Because of those analogies, the thermal evolution of Venus and the Earth is similar and they both experienced extensive volcanic activity. However, the style of volcanism on Venus is very different from the one observed on Earth. Where mantle convection and plate tectonics are the main causes for volcanic activity on Earth, major resurfacing events involving flood basalts seem to be taking place on Venus [Nimmo and McKenzie, 1998]. The centres for volcanic activity seem to be scattered at the surface, similarly to intraplates volcanic centers on Earth [Wilson, 2009]. The type of features present on Venus include small and large shields, lava flows, dike swarms and flood basalt provinces. Some do not have terrestrial analogs such as coronae which are circular features exhibiting concentric radial fractures [Crumpler and Aubele, 2000], arachnoids (named after their resemblance to spider webs) and novae. These unusual features might be the product of how differently the Venusian crust handles deformation [Parfitt and Wilson, 2009].

Mars is one of the terrestrial planets in our solar system that exhibits great geological diversity alongside with the Earth. No active tectonics has been observed on this body as there is no evidence of active ridge and trench systems. The planet is divided into two main areas: the highlands, covered with extensive lava flows; and the lowlands, where volcanic plains cover most of the surface [Wilson, 2009]. Two volcanic provinces contain most of the erupted volcanic materials: Tharis and Elysium. In these areas, large shield volcanoes can be observed, including the highest mountain in the solar system: Olympus Mons [Parfitt and Wilson, 2009]. These large shields are the result of basaltic flows and can be compared to intraplate volcanoes on Earth. Cones of various sizes are also present on Mars and have been compared to cinder cones on Earth [Frey and Jarosewich, 1982].

Mercury is the smallest planet in our solar system and also the densest. This

very high density reflects the presence of a large iron core (compared to the size of the planet) which could potentially provide a considerable heat source to enable volcanism [Parfitt and Wilson, 2009]. Up until 2008, with the return of images from the fly-by of Messenger, our knowledge of the surface of the planet came from images made by Mariner 10 during its fly-bys in 1974. Messenger was able to image an additional 21% of the planet and the hypothesis about the volcanic nature of intercrater plains [Strom et al., 1975] was confirmed. Volcanic vents were observed and identified as the source for effusive eruptions and the formation of shield volcanoes and lava flows [Head et al., 2009]. Some evidence for explosive volcanism was also gathered from the images [Prockter et al., 2010].

Io is one of Jupiter's satellite and is the most volcanically active planetary body in the solar system. Unlike most of the other bodies, the source for internal heating for Io comes from the colossal tidal force that Jupiter applies on its satellite. More than 300 vents have been identified at the surface and no signs of plate tectonics have been detected. Silicate volcanism seems to be the main type of volcanism present and the identified hot spots exhibit two types of activity: persistent and sporadic [Lopes-Gautier et al., 1999]. The main types of feature present at the surface are lava flows, lava fountains, high mountains and an analog to terrestrial caldera called paterae [Radebaugh et al., 2001].

Comparative planetology aims at comprehending the physical factors governing the shape of planetary landforms as well as the styles and patterns of eruption. Past studies have attempted to compare volcanic structures on Earth to similar features on other planetary bodies with some success. Similarities have been found between Martian cones and cinder cones on Earth [Frey and Jarosewich, 1982] and also between small Venusian domes, shields and cones and terrestrial sea floor volcanoes [Smith, 1996, Bulmer and Wilson, 1999]. Because of the relationship between caldera diameter and magma chamber dimensions and depth, the comparative study of planetary calderas constitute a great tool to gain a better understanding of planetary subsurfaces [Wood, 1984].

## 1.2.2 Terrestrial Volcanism

Volcanic eruptions on Earth are the result of complex interactions between magma (molten rock) and the crust, and volcanoes are non randomly distributed across the

surface, being primarily located at plate boundaries (subduction zones or mid-ocean ridges, see Figure 1.1). Around subduction zones, hydration of the mantle is caused by the release of water from the subducting plate, which facilitates partial melting and subsequent rise of magma into the crust. At divergent margins, decompression of the mantle under a thinning plate enables partial melting. Active volcanism can also be found in the middle of tectonic plates and is characterized by hot spots volcanoes. In this case, melting is allowed by the presence of high temperature zones deeper in the mantle. A plume is generated and feeds the volcanoes at the surface.

Within the crust, magma rises due to density differences. When a depth where the magma is neutrally buoyant is reached, the latter accumulates forming a continuous body called a magma chamber. The depth of magma chambers ranges from about 2 km to 10 km, depending on the magma composition (Pinkerton et al. [2002] and references therein). Once in this storage area, the magma starts to evolve. Cooling will bring its temperature below the liquidus, allowing successive minerals to form. This process is referred to as fractional crystallization [Parfitt and Wilson, 2009]. As the magma cools and crystallizes in the chamber, volatiles such as water and halogens will appear in the residual melt, according to the magma composition. When their concentration reaches a saturation level, gas is exsolved to form bubbles in the chamber. This process induces a sudden reduction in density, which increases the buoyancy of the material in the magma chamber. This presence of bubbles is also responsible for a pressure increase in the magma chamber. Once this pressure  $P$  becomes larger than the lithostatic pressure  $P_L$  by an amount larger than the value of the tensile strength of the chamber walls, the creation of cracks, or dykes, above the chamber is possible and the magma starts rising [Blake, 1981]. This gas bubbles formation process, alongside with the addition of new magma in the chamber are considered as two of the main causes for initiating eruptions. Figure 1.2 presents a schematic view of the magmatic plumbing system.

Scandone et al. [2007] proposed a conceptual model to describe magmatic processes. They divided the magma system into four different regions. The supply system is located at the crust/mantle boundary and provides the primary deep source of magma. For small eruptions, this area is not involved directly in the eruption process. The intermediate storage system is located at mid to shallow depths in the crust and constitute what we previously defined as the magma chamber. There, the magma can stop or rise due to density differences and will start to cool and evolve.

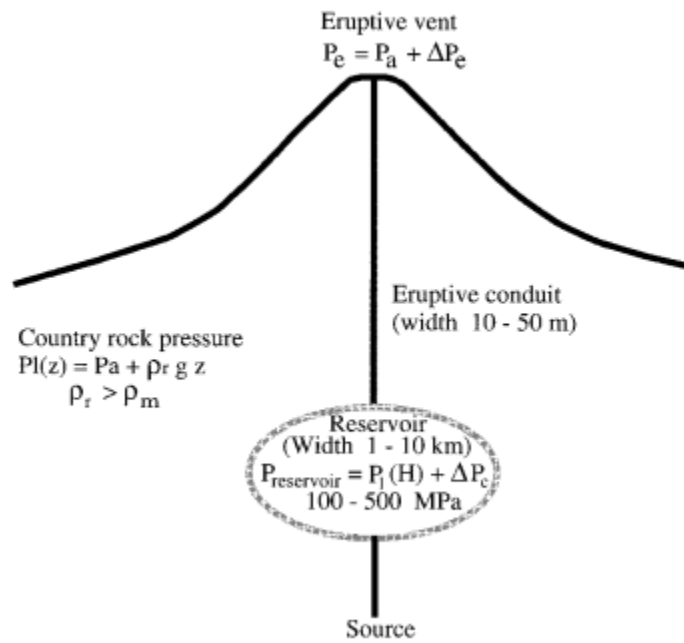


Figure 1.2: Sketch of the magma plumbing system. The magma chamber is located at a depth  $H$  from the surface and the pressure within the chamber is a combination of the pressure due to the host rock  $P_l(H)$  and the overpressure generated by the input of magma or the increase in gas content in the chamber  $\Delta P_c$ . The eruption exit pressure is a combination of the atmospheric pressure  $P_a$  and the excess pressure in the vent  $\Delta P_e$ . The lithostatic pressure around the chamber  $P_L(z)$  is a function of depth and the density of the host rock  $\rho_r$  [Jaupart, 2000].

The third region is the transport system. As previously described, when the magma starts cooling, crystallization will occur as well as bubble formation. This will create local stress field changes and density unbalance that allows the magma to propagate through a fracture system. The last component of Scandone et al. [2007]’s system is the eruptive system, a shallow region in the crust from where the magma is erupted. Depending on the magma composition and therefore the volatile content ( $\text{H}_2\text{O}$ ,  $\text{CO}_2$ ,  $\text{SO}_2$ ,  $\text{H}_2\text{S}$ ) in the chamber, different styles of eruptions will be initiated.

The overpressure in the magma chamber initiated by the input of new magma or the increase in volatile content leads to the formation of dikes. Dikes are hydraulic fractures within the crust that allow the magma to rise from one reservoir to another, and ultimately to the surface [Tait and Taisne, 2013]. Almost all eruptions are supplied with magma from the chamber to the surface through dikes. The propagation and evolution of dikes depend on the stress state surrounding the volcano [Gudmundsson, 2006]. Understanding the formation, propagation and arrest of dikes between the magma chamber and the surface is therefore one of the requirements to understand the temporal pattern of eruptions. Theoretical models have considered the effects of overpressure or buoyancy in an existing crack. The flow in the magma filled crack can be described using fluid dynamics non linear equations [Lister, 1990]. Many analogue experiments have also been carried out to link theoretical models of dike propagation and geological observations. Acocella et al. [2008] investigated the dike patterns of Somma-Vesuvius and Etna using a laboratory experiment. The crust and magma were modeled using respectively gelatin and water. The water was injected in the cone and the formation of dikes was studied. The results of that experiment showed that, in that case, dikes at the surface exhibited a radial pattern while tangential and oblique dikes were observed at depth. These results have implications for the prediction of the location of future eruptions on the volcanic edifice. As stated before, the stress state within the volcano influences the formation and propagation of dikes. Many studies using analytical models have investigated the stress field around a volcano by considering the host rock as a homogeneous and isotropic system with an elastic behavior ([Gudmundsson, 2006] and references therein).

Volcanoes can exhibit explosive and effusive activity. The type of eruption depends largely on the magma’s silica content. Silica rich magmas can contain up to 6% of water and the eruptions associated will be characterized as explosive. With a high silica content comes a large volume of gas bubbles in the chamber. When this vol-

ume is large enough, a continuous phase will be initiated from the bubbles connecting together. This process is referred to as fragmentation [Cashman et al., 2000]. An explosive eruption can be manifested by several outputs. Strombolian eruptions exhibit small and discrete explosions of ashes, gas and magma. Hawaiian eruptions display intense and near continuous fire fountains [Vergnolle and Mangan, 2000], while Plinian eruptions are infrequent but extremely explosive and sustained and characterized by stable eruption clouds [Cioni et al., 2000]. As stated before, fragmentation is one of the processes responsible for explosive eruptions and has therefore been extensively studied. This mechanism corresponds to the transformation process of bubbly magma into gas-pyroclast dispersion [Papale, 1999]. Laboratory experiments have been designed to study the mechanisms responsible for bubble nucleation, acceleration of the flow and the process of fragmentation. Mader et al. [1994] proposed to simulate explosive eruptions by generating supersaturation of CO<sub>2</sub> in a liquid phase (water in this case). Phillips et al. [1995], used a gum-rosin acetone solution to simulate the conduit flow that leads to fragmentation. Both these models were able to demonstrate that decompression in a supersaturated liquid is the starting point of the fragmentation process. Going further in the investigation of the fragmentation process, Stix and Phillips [2012] studied the role of the speed of pressure changes in the process of fragmentation. Using the same gum rosine acetone system, they showed that fragmentation is induced by only fast decompression conditions.

Basaltic magma, with a significantly lower silica content, will result in effusive eruptions. The main products of basaltic eruptions are lava flows, lava fountains and the creation of volcanic fields. When the silica content increases, the magma becomes more viscous and blocky flows and domes are generated. Volcanoes can display different types of activity during their eruptive history. During an eruption, the degree of explosivity will decrease with time. The volatile rich magma is mostly concentrated at the top of the chamber and erupts first, leaving the magma available for the rest of the eruption poor in volatiles. The reduced pressure in the chamber due to the loss of magma from the eruption also has an effect on the ascent velocity, which also controls the explosivity of the eruption [Pinkerton et al., 2002]. There seem to be a transition between effusive and explosive activity when a critical ascent rate of  $0.2 \text{ ms}^{-1}$  is reached [Rutherford and Gardner, 2000].

The different styles of volcanic activity give birth to different volcanic landforms [Lockwood and Hazlett, 2010]. Here, we only overview the most common and

prominent types of features. Shield volcanoes are the product of effusive activity characterized by low discharge basaltic flows. The lava flows involved in building such structures have a very low viscosity and are initiated at shallow depth. Composite volcanoes, or stratovolcanoes, are the result of a complex eruptive history. The edifice is built from the deposition of multiple eruptive layers. Cinder cones are a smaller volcanic feature resulting from Strombolian type, basaltic eruptions. When large eruptions occur, the drained magma chamber can collapse and form a multi-kilometer wide, quasi-circular depression called a caldera [Lipman, 2000]. This type of feature can be observed on top of shield or stratovolcanoes.

There are approximately 1500 volcanoes on land on Earth [Tilling, 1989]. The most active volcanoes are currently extensively monitored using a wide variety of tools such as seismic sensors, GPS measurements, to mention a few. Historical data are also very rich in information and allow us to have access to a significant amount of data on the temporal evolution of eruptions. This wealth of data allows us to study volcanic processes from a statistical point of view in order to identify patterns in their activity.

### 1.3 Statistical Modeling of Volcanic Processes

Statistical analysis is a powerful tool to study the characteristics of natural processes and to infer the physical mechanisms underlying those processes. One of the first statistical analysis carried out on volcanic data was performed by Wickman [1966] on Hawaiian volcanoes. One of the main statistical models used to describe the observed temporal patterns of eruptions was the Poisson process.

A homogeneous Poisson process is a mathematical model that describes a series of random events. Events in that case are stationary and independent from each other [Ho, 1991]. The main characteristics of such a model are the following [Cox and Lewis, 1966]:

- The probabilities of an event happening or not, do not change in time, and therefore, the time series does not display a trend.
- Two events have negligible chances of happening together.



- The probability of an event happening at time  $t + h$  is independent on what happened at time  $t$ . The probability of an event happening at  $t + h$  does not depend on the time elapsed since the preceding event.

When studying natural hazards time series, one useful characteristic to investigate is the distribution of intervals between events, or interevent times  $\tau$ . The interevent times for a homogeneous Poisson process are exponentially distributed with parameter  $\lambda$ . This parameter represents the rate of events, or how many events can occur per unit time. In this case,  $\lambda$  is a constant. The events are independently distributed and occur at a constant average rate.

The hypothesis of volcanic eruptions behaving as a Poisson process has been tested on a wide range of datasets. As previously stated, Wickman [1966] investigated the temporal behavior of Mauna Loa and Kilauea volcanoes. He found that the eruptive activity of Mauna Loa can be approximated by a Poisson process but that the activity of Kilauea showed a non-constant event rate. Reymont [1969] studied the activity of 3 Japanese volcanoes, Etna, 3 Indonesian volcanoes and Mauna Loa. He was able to show the random behavior of Mauna Loa and Bromo volcanoes. His study led him to conclude that some eruption time series could be approximated by a Poisson process but that this model was not universal for all volcanoes.

The activity of Stromboli volcano was examined through the eruption sequence of 3 different vents [Settle and Mcgetchin, 1980]. It was found that the interevent time distributions for 2 of the 3 vents could be fitted by an exponential distribution, and therefore their activity could be modeled by a Poisson process. The eruption mechanism at the remaining vent could be characterized by a normal (Gaussian) process. A correlation was observed between the temporal behavior of vents 2 and 3 with vent 1. This dependency suggested that vents 2 and 3 were directly connected to the magma reservoir beneath vent 1.

Another study of the activity of the Hawaiian volcanoes defined the interevent times of volcanic events as the time elapsed from one eruption onset to the other, Klein [1982] investigated flank and summit eruptions. Again, a Poisson process was concluded to be a good fit, despite some departure from the model was observed for the distribution of interevent times between large eruptions and eruptions of any size following them. This discrepancy was explained by the finite character of the magma supply in the volcano. De la Cruz-Reyna [1991] investigated the temporal patterns of global volcanic activity. It was found that for large eruptions, the distribution

of interevent times between eruptions could be modeled by a homogeneous Poisson process. Volcanoes were concluded to be systems capable of storing a large amount of energy while releasing it in small amounts at a constant rate.

In all of the aforementioned works, the hypothesis of volcanic events being a series of independent random events has been validated but it was also often noticed that this model was not universal for all of the datasets considered. The introduction of the non-homogeneous Poisson process as a generalization of the model has allowed some of the behaviors to be better explained. A non-homogeneous Poisson process, or time-dependent Poisson process, satisfies the same assumptions than a homogeneous Poisson process, but  $\lambda$  is now a function  $\lambda(t)$  of time. When the randomness of events implies that several processes are combined to trigger eruptions, having a non-homogeneous Poisson process implies that the balance between those processes changes with time.

Ho [1991] tested the non-homogeneous model on 5 individual volcanoes. In that study, he considered an eruptive rate  $\lambda(t)$  such as  $\lambda(t) = \beta\theta^{-\beta}t^{\beta-1}$  where  $\beta$  and  $\theta$  are constant parameters and  $t$  is the time since a predefined origin. Bebbington and Lai [1996a] argued that this approach was unsatisfactory and proposed a more general approach. They proposed a Weibull renewal model to describe the occurrence of volcanic eruptions on New Zealand volcanoes. A renewal process comprises interevent times that are identically and independently distributed that have a common distribution  $D$ . For the homogeneous Poisson process,  $D$  is an exponential distribution. For the Weibull renewal process, used by Bebbington and Lai [1996b],  $D$  is a Weibull distribution. This type of renewal model was used in order to issue prediction on the eruptive activity of Mount Vesuvius, where  $D$  was defined as Gamma distribution [Ho, 1992]. Using this very same non-homogeneous Poisson process approach, Dzierma and Wehrmann [2010] investigated the interevent time distributions for volcanoes in the south Chile volcanic zone using several distributions such as the Weibull, the log-logistic and the exponential distributions to describe  $D$ . All the examples show that the non-homogeneous Poisson process can be successful at describing eruption time series. The nature of  $D$  seems to be different depending on the volcanoes considered. Other methods have been developed with the same goal of fitting the interevent times distribution of eruptions, such as a mixture of exponential distributions [Mendoza-Rosas and De la Cruz-Reyna, 2009].

When examining the temporal patterns with the goal of mitigating volcanic

risks, it is important to consider the return period of large eruptions since they tend to be more destructive. From a statistical approach, extreme events are located at the tail of the distributions describing their probability of occurrence [Albeverio et al., 2006]. The statistics of extremes have been originally developed by Gumbel [1958] and the goal is to gather as much information as possible on the temporal and spatial distributions describing these large events. Being able to characterize the statistical distribution of extreme events is one of the biggest challenges that researchers have been trying to overcome. The main goal is to predict the size of the next largest event, or the probability that the largest event will occur in a certain time window and at a certain location [Gumbel, 1958]. The interoccurrence time of extreme events, which is the time between two consecutive extremes, is also a powerful tool in characterizing the temporal properties that can be used to predict such events [Altmann and Kantz, 2005].

Pyle [1998] used the rank-ordering method in order to define the likely size of extreme volcanic eruptions. This method was introduced in statistics by Gumbel [1958] and has been applied to a large number of problems since then. The concept of the method is simple. The sizes of eruptions are ordered where the largest event has the first rank, the next largest the second and so on. The analysis is done by plotting the size of the events versus their rank [Pyle, 1998]. One of the reasons for carrying out this analysis was to try and place an upper limit on the size of future extreme eruptions. For this study, several datasets were used: data for large volcanic eruptions since A.D 1815 and data from the Taupo volcano in New Zealand for the last 25 000 years. This method allowed them to predict the size of the next largest events and the longest time interval between events for the catalogs considered.

Coles and Sparks [2006] applied extreme value statistics to a 2000-year eruption catalog. The goal of the analysis was to determine the parameters associated with intensity function  $\lambda(t)$ , and ultimately deriving the return period associated with a certain magnitude  $m$ :  $r(m)$ . This analysis raised the issue of the choice of a magnitude threshold when using extreme value statistics. If a high threshold is chosen for the analysis, the results will be truly representative of extreme events but the quality of the statistics will be poor since extremes are, by definition, rare. On the other hand, choosing a lower threshold will increase the quality of the statistics but the events sampled are not all extremes events. In addition, the fact that the catalog used for this study only covers the last 2000 years makes it difficult to make inferences on

return periods over very long time scales. To address this problem, Deligne et al. [2010] applied the same method to a new database of Holocene explosive volcanism. They showed that the model, due to a large amount of under reporting in the data, was predicting maximum eruption magnitudes that were too small because of the sampling biases. The likely explanation is that the data available only samples the high end of "ordinary" eruptions (characterized as Plinian) and that the mechanism behind "super eruptions" is different. The method used in that study was only able to predict recurrence rates for the upper limit of Plinian-type eruptions and not for the super-eruptions.

We have provided an overview of the type of common statistical analyses that have been done on volcanic eruptions. Like many natural hazards, eruptions have also been considered as a self-organized process [Grasso and Bachelery, 1995]. Such a process is characterized by a slowly driven dynamical system which organizes itself in a critical state. Once this state is reached, dissipation occurs in the form of avalanches of all sizes that are regular in time, but not periodic [Bak et al., 1988]. One example of this kind of system is described by the sandpile model: when constantly adding sand grains to a small sandpile, small and big avalanches will rapidly form in order to decrease the local slope whenever they reached a critical angle. The frequency size distribution of those avalanches is described as a power-law in the case of a self-organized system [Bak et al., 1988]. The distribution of magnitudes and/or Volcanic Explosivity Index (VEI) of volcanic eruptions, displays scale-invariant characteristics [Newhall and Self, 1982, De la Cruz-Reyna, 1991, Simkin, 1993, Gusev et al., 2003]. The cumulative distribution of the annual amount of tephra produced by eruptions also exhibits power-law behavior [Turcotte, 1997]. Power laws were also observed from the spatial distribution of volcanic fields [Pelletier, 1999]. Gusev [2008] observed self-similar clustering in time and size for eruptions. It was also observed that large eruptions tend to occur during the most volcanically active periods. These characteristics of global volcanic activity lead to the conclusion that a global mechanism was responsible for the time/size clustering. Marzocchi and Zaccarelli [2006] observed two different regimes concerning interevent times: short times are clustered and can be explained by an open conduit system while long interevent times show random behavior that can be characterized by a Poisson process and explained by a closed conduit system. These two regimes were also associated with different rhythms in magmatic intrusions [Dubois and Cheminee, 1991].

The latter statistical analyses have in common the consideration of volcanic eruptions on a global scale, using worldwide data. Investigating natural hazards such as earthquakes on a worldwide basis has proven to be a successful approach to understand the triggering mechanisms of the system's avalanches. In the case of earthquakes, the constant loading is due to tectonic forces acting on faults while the earthquakes constitute the avalanches. Several scaling laws, implying that the triggering mechanism operates the same way at broad spatial and temporal scales have been proposed in studies of seismicity [Corral, 2003], forest fires [Corral et al., 2008], solar flares [Baiesi et al., 2006], tropical cyclones [Corral et al., 2010] and in the occurrence of rock fracturing [Davidsen et al., 2007, Åström et al., 2006]. In this thesis, we focus on a global approach to understand the temporal patterns of volcanic eruptions.

## 1.4 Modeling of Volcanic Processes

Field based observations of volcanic processes are often incomplete and/or uncertain due to the infrequent nature of eruptions in most cases. One way to overcome this issue and study volcanic processes is to formulate models that can describe the empirical data collected in the field. The advantage of laboratory and numerical modeling is the possibility to produce a large number of repetitions to validate the results, and measurable outcomes. Magma processes follow the laws of physics and many subdisciplines are involved in the modeling of volcanic processes such as thermodynamics, fluid dynamics, solid mechanics, wave theory [Fagents et al., 2013]. A better understanding of the processes can be achieved through experimental, theoretical or numerical modeling. All approaches aim at describing processes such as dike propagation, bubble formation and ascent, magma chamber formation and collapse. The combination of the different types of modeling enables volcanologists to refine our knowledge on the processes acting in the crust and leading to eruptions (see Figure 1.3).

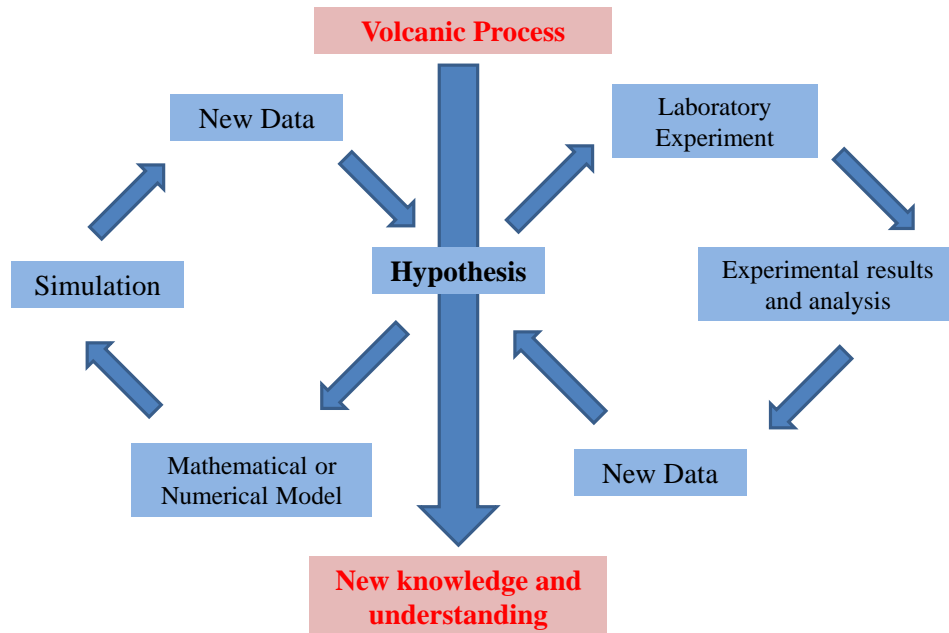


Figure 1.3: Schematic steps of the use of experimental and numerical/mathematical modeling to validate hypotheses on volcanic processes

As seen in Figure 1.3, laboratory experiments are a major component of the methodology used to understand volcanic processes. The empirical determination of some important parameters happened through laboratory experiments. They can be designed using natural or analog materials, according to the type of processes investigated. Small scale processes allow for the use of natural materials and a view of the whole system, while large scale dynamics are studied using magma analogues [Mader et al., 2004]. In the latter case, the full range of behavior is rarely captured and scaling the system becomes a main concern. This thesis will not focus on laboratory experiments, but rather on numerical methods.

### 1.4.1 Numerical Models

With the technological advances and the development of supercomputers, numerical modeling has become an essential tool of most science disciplines. The approach used to formulate a numerical model comprises three main steps. The first step encompasses the formulation of the mathematical description of the phenomenon studied which captures its essential physics. The second steps consists in finding the

optimal method to solve the previously defined equations. Many physical systems are described using sets of partial differential equations and numerical approximation is often the only approach available to solve them. Methods such as finite differences of finite elements are already widely used and emergent approaches such as Monte Carlo methods or cellular automata keep increasing the capabilities of numerical modeling. The last step involves comparing the numerical results with real data in order to ensure that the model reproduces the behavior of the system investigated. This entails a large qualitative understanding of the processes [Allen et al., 1988]. The use of numerical modeling in the field of volcanology has permitted the study of complex processes in the magma chamber.

As stated in the overview of volcanism Section 2.2, laboratory experiments and theoretical modeling have been successful at describing some key volcanic processes such as magma fragmentation. Numerical models using continuum mechanics have also been developed in order to further our understanding of this transition from bubbly magma to pyroclasts in an explosive eruption. Using a non-equilibrium two phase flow fluid dynamics model, Papale [1999] introduced a "fragmentation criterion" in order to show the possibility of a strain-induced brittle fragmentation. The advantage here was the possibility to account for many variables such as friction, viscosity, density, etc. The results from this analysis are in accordance with the experimental results on the amount of the gas volume fraction needed for fragmentation to occur. This study also showed that strain induced fragmentation is a feasible process for explosive volcanic eruptions. In order to further our understanding of the process, Melnik [2000] developed a model considering the pressure difference between the bubbles and the melt and later also considered vertical gas escape through the magma [Melnik et al., 2005]. From this formulation, the critical overpressure between the bubbles and the melt was shown to be a new requirement for fragmentation.

Considering dike formation and propagation, analytical models assume isotropic and homogeneous systems to allow calculations of the fissure opening and propagation. However, the host rock is usually anisotropic and heterogeneous. These characteristics imply that the derivation of simple analytical solutions is not possible and numerical models provide a powerful tool to investigate the effect of anisotropy and heterogeneity for the propagation of dikes. Investigating the elastic deformation of the host rock and the effect of magma fragmentation on the formation of dikes using a numerical approach, Taisne and Jaupart [2011] showed that fragmentation slows

down the speed of dike formation. These results were tested against a Mount Saint Helens eruptive unrest episode where the episode of slow progression of the magma to the surface was attributed to fragmentation within the dike.

These models are non exhaustive examples of the necessity and complementarity of laboratory experiments, analogues and numerical models in understanding volcanic processes. In all the cases presented, the models focus on describing one specific process or set of processes that take place in the volcanic system using sets of equations. The field of modeling have seen the emergence of different kinds of models, such as Monte Carlo methods, random walkers or cellular automata. These methods are classified as stochastic and are characterized by the use of random numbers [Rappaz et al., 2003]. The Monte Carlo method entails the calculation of averages through the generation of a large amount of random numbers and therefore allows for the determination of probabilities. This kind of model was used to generate configurations of atoms or magnetic moments at the microscopic scale in order to obtain information at the macroscopic scale for example. Cellular automata methods aim, similarly to Monte Carlo methods, at replicating a complex behavior through the use of simple rules defined at the microscopic level [Rappaz et al., 2003]. In this thesis, we will focus on the application of this type of model on volcanic eruptions.

### 1.4.2 Cellular Automata Models

Volcanic eruptions can be considered as outcomes of complex interactions between the magma and the host rock within the crust. In order to simulate eruptions, it is important to formulate models that account for the complexity of the system as a whole. One class of models that have been successful at simulating the behavior of complex systems are the cellular automata models (we will refer to the as CA from now on). CAs are an idealization of a physical system where time and space are discrete and the physical characteristics described are represented by only a set of values. The dynamics of physical systems are often described using nonlinear partial differential equations. Due to nonlinearities, the solutions of these equations are strongly sensitive to the initial conditions. The same type of complications can occur in discrete dynamical systems such as CAs [Chopard and Droz, 1998].

One of the first CA was formulated by Von Neumann in 1940 but the most famous one is the *Game of Life* by John Conway in 1970 ([Chopard and Droz, 1998]



and references therein). In this two-dimensional model, simple rules are designed to model a dynamical system. Live and dead cells (characterized by a value of respectively 1 or 0) are located on a 2D lattice and their state depends on the state of the cells in their neighborhood. Live cells can die of overcrowdness or isolation if surrounded by too many or too little live cells, and dead cells can come back to life if surrounded by enough live cells. This system ended up displaying a complex behavior where distinctive complex structures would emerge and develop.

Wolfram [1986] defined and studied the simplest class of one-dimensional CA. Each cell has a possible value of 0 or 1 and the rules for the time evolution of the system are defined only according to the state of the nearest neighbor (see Figure 1.4).

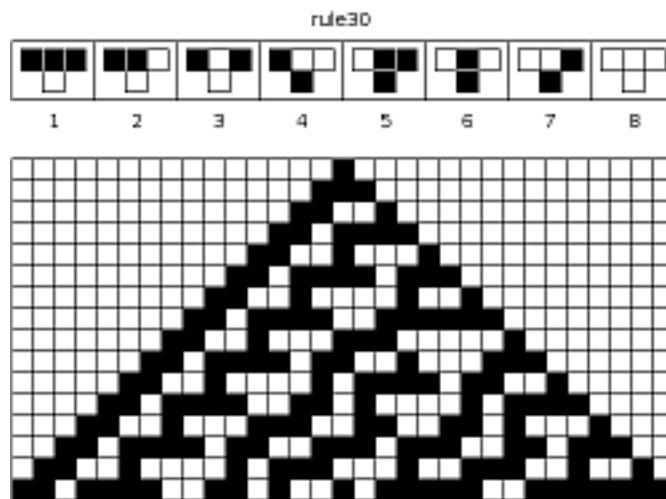


Figure 1.4: Example of the evolution of the Wolfram CA from rule 30. The upper part displays the evolution rules for each possible configuration at time  $t$  (from [www.mathworld.wolfram.com](http://www.mathworld.wolfram.com))

The extensive study of this model led to the conclusion that despite the discrete character of CAs, they were successful at reproducing behaviors of continuous systems. It was also found that the Boolean nature of this type of model (the values describing the physical characteristics of the model can only take integer values) allowed for exact numerical calculations, making the investigation of complex systems more accessible. Because of these characteristics, cellular automata have been used to describe physical systems.

Since then, the use of cellular automata has largely increased in the field of natural sciences and models have been successful at reproducing the complex behav-

ior of some natural hazards such as earthquakes [Ogata, 1992, Olami et al., 1992, Helmstetter et al., 2004] and forest fires [Bak et al., 1990]. In order to model fluid behavior, Hardy et al. [1976] formulated the so-called HPP model. This type of CA is classified as a lattice-gas model and describes fluid behavior on a microscopic level. Particles interact with each other through collisions in a two-dimensional lattice in way that allows conservation of momentum and energy. The use of CAs in the field of volcanology is a new approach and has been mainly applied to model the flow of erupted lava in order to improve the determination of hazardous zones on specific volcanoes [Vicari et al., 2007, Crisci et al., 2003, Del Negro et al., 2008]. Lahaie and Grasso [1998] developed a CA composed of fluid and rock cells interacting with each other in order to reproduce the behavior of the eruptive activity of the Piton de la Fournaise volcano. They were able to show that the behavior of the volcano can be explained by a combination of multiple magma storages rather than a main magma chamber. Pelletier [1999] combined a model of fluid migration in a disordered porous media developed by Buldyrev et al. [1992] with eruption dynamics. His goal was to describe magmatic upwelling through the continental crust. When analyzing the synthetic history of volcanism produced by this model, Pelletier found that the spatial and temporal pair-correlation functions were consistent with the functions obtained from real data.

Interested in investigating the temporal and size distribution of volcanic events in closed conduit systems, Piegari et al. [2008] designed a CA that models magma ascent through the crust. The model is incorporating in a series of simple rules, the key processes responsible for magma ascent such as buoyancy, the control of the ascent by the ambient stress field, the injection of magma through preformed cracks, and the magma induced formation of new cracks. In a two-dimensional lattice, the initial stress level of each site is assigned randomly while a slow constant loading is applied to each site following the rule of the model developed by Olami et al. [1992]. Fractures are initiated when the stress level at one site exceeds the maximum shear stress of the rock and stress is redistributed to the site's neighbors, creating a chain reaction and the formation of crack networks. Magma feeding is initiated in the magma reservoir at the bottom of the lattice and is allowed to rise in an upward direction when in contact with a crack. An eruption occurs when a batch of magma reaches the surface (top of the lattice) and the volume  $V$  of the eruption is defined by the number of magma filled sites connected to the surface. From this model, Piegari et al. [2008] computed the

probability distributions of eruption volume  $P(V)$  and interevent time  $P(t)$ . It was found that the size distribution of eruptions exhibits a power-law behavior consistent with the behavior observed in nature by using the Volcanic Explosivity Index (VEI) scale for eruptions [Newhall and Self, 1982, Simkin, 1993]. Concerning the interevent time distribution  $P(t)$ , the model results exhibit an exponential behavior for large eruptions, implying that the major events are independent and occur at a constant rate, while small events are better fitted by a stretched exponential distribution.

Expanding this model, Piegari et al. [2011] incorporated the effect of the water content of the magma. When saturation pressure was reached in the chamber, the magma exsolves water and this exsolution process affects the explosivity of the eruption. From this model, it was found that magma that has been completely degassed during ascent was most likely to produce eruptions than magma that was still gas-rich. Low explosivity eruptions were more frequent but smaller in volume than high explosivity ones, which was in agreement with observations. In another formulation of the model, Piegari et al. [2013] introduced a rock density layered structure in order to approximate the density structure of mount Vesuvius. The density differences between the magma and the host rock determined whether or not the magma was allowed to rise, or had to stop and started cooling and solidifying. This solidification process will also alter the density of the layer. The interevent time distributions produced by the model is in agreement with the data from Vesuvius. A characteristic interevent time arose when the model got reset after large eruptions, which was interpreted as the time it took for the magma to reach the surface from the reservoir at the bottom. This model showed that the temporal pattern observed for Vesuvius as well as the style of eruptions could be explained by the presence of density barriers within the crust.

These cellular automata have shown that the use of a simple model implementing a minimal number of rules and including a small amount of parameters is a powerful tool to study the statistical properties of volcanic eruptions. In this thesis, we formulate a CA model that investigates the magma/crust interactions in order to further our understanding of the several volcanic temporal regimes in open and closed conduit systems. We focus on using a minimal amount of parameters in order to investigate universality in eruption processes. We compare the results of the CA with temporal data obtained from worldwide catalogs.

## 1.5 Thesis Outline

The main goals of this thesis are:

- Understanding landform formation and evolution in the solar system using comparative planetology, with a focus on volcanic features and impact craters,
- Investigating the global temporal behavior of volcanic eruptions on Earth,
- Understanding the nonlinear interactions taking place in the solid crust which lead to an eruption.

To address these goals, I divided the rest of this thesis into four chapters. The first two chapters focus on comparative planetology and the investigation of landform formation mechanisms in the solar system. In chapter 4 and 5, the analysis is focused on volcanism on Earth, and more specifically on the investigation of eruption mechanisms on a global scale.

### 1.5.1 Chapter 2: Scaling Properties of Planetary Calderas

Comparative planetology is important in understanding the formation mechanisms of planetary volcanic structures. One surface feature that is common to Mars, Venus and Io is the paterae. This landform is described as an irregular volcanic crater with scalloped edges. The general consensus in the interpretation of paterae on Venus and Mars is that they are analogs for calderas [Sigurdsson et al., 2000]. This argument has been supported by the comparison of the distributions and morphology of paterae on Io to calderas on Earth and paterae on Mars and Venus [Radebaugh et al., 2001]. A planetary definition of a caldera is a multi-kilometer wide, quasi-circular depression, not of impact origin, formed in volcanic terrain by the collapse of the volcanic edifice into a partially drained magma chamber [Lipman, 2000].

In this chapter, we first investigate the statistical properties of the size distributions of calderas and paterae on Earth, Mars, Venus and Io using a scaling analysis technique [Bak et al., 2002, Corral, 2003]. We compiled datasets of caldera/paterae diameters and areas of those planetary bodies and performed a scaling analysis using the mean diameter/area as a scaling factor. Second, using the same method, we investigate the scaling properties of calderas dimensions on Earth, according to various crustal settings: continental sillicic crust, basaltic oceanic crust and transitional

crust. We propose a scaling law to quantify the distribution of caldera sizes on Earth, Mars, Venus, and Io, as well as the distribution of calderas on Earth depending on their surrounding crustal properties.

### **1.5.2 Chapter 3: Statistical Analysis of the Size Distribution of Impact Craters in the Solar System**

In Chapter 3, using the same statistical method, we investigate the scaling properties of frequency-size distributions of impact craters on the Moon, Earth, Mars, Mercury and Venus. Our goal is to find a common distribution to describe the population of impact craters throughout the inner solar system.

We find that large impact craters on Mars, the Moon, Mercury and Venus have the same statistical characteristics while large craters on Earth seem to deviate from this common distribution. We conclude that large impact craters on Mars, the Moon, Mercury and Venus possess the same formation and evolution characteristics. Small craters on Venus behave differently due to an important atmospheric filtering effect. Impact craters on Earth seem to evolve differently. We hypothesize that the active tectonics and heavy erosional processes found on Earth are responsible for the difference in crater size distributions.

The results from chapters 2 and 3 lead us to emphasize the importance of comparative planetology to understand planetary volcanism and landform formation in our solar system.

### **1.5.3 Chapter 4: Temporal Scaling of Volcanic Eruptions**

In Chapter 4, we focus on the temporal behavior of volcanic eruptions throughout the World. We compile the eruptive history of 26 of the most active volcanoes as well as eruptions of 163 less active volcanoes that we group into 9 volcanic regions. We also compare the temporal activity of volcanoes by grouping them into four different volcano types: shield volcanoes, strato volcanoes, complex volcanoes and calderas. We find that probability density functions have a similar functional form when they are rescaled with the corresponding sample averages. The obtained scaling law for interevent times can be modeled using the log-normal distribution and signifies that the dynamics of volcanic eruptions on Earth is similar and quite independent of the type of volcanism and the geographical location of volcanoes. The phenomenon of

triggering volcanic eruptions operates in a similar way for all volcano types, which emphasizes the importance of studying volcanism as a universal process.

### 1.5.4 Chapter 5: A Cellular Automata to Model Magma/Crust Interactions and Volcanic Eruptions

In Chapter 4, we showed that the interevent time distributions of volcanic eruptions are characterized by a universal behavior, independent of the type of volcanism and geographical location. The distribution for eruptions with a large interevent time seems to deviate from the simple Poisson statistics.

In Chapter 5, we propose to use a lattice gas cellular automata (LGCA), which have been proven efficient to simulate fluid flow behavior. This type of cellular automaton is a discrete dynamical model in space and time, where the fluid is represented at the microscopic level by discrete particles. We define a 2-dimensional model which consists of a square lattice where particles interact with one another mimicking magma movements through the crust. In this model, magma propagates through the host rock, and fracturing occurs on the walls of the chamber. When magma reaches the top of the crust, an eruption or a cascade of eruptions occur. We record the size of each event and the number of time steps between consecutive events (or interevent time). The model simulation results for a large number of realizations are compared with observed data. We observe several regimes of eruptions that could be representative of close and open conduits systems. This model allows us to describe the dynamics of complex magma interactions using a minimum number of parameters.

In this thesis, we aim at showing that by using statistical analysis, we can identify global characteristics for volcanic landforms and patterns of volcanic eruptions. These results, integrated with our qualitative knowledge on volcanic processes and landform formation, will lead to a better understanding of physical mechanisms of volcanism and ultimately to improved volcanic hazard assessment methods on Earth.

## References

- V. Acocella, M. Neri, and R. Sulpizio. Dike propagation within active central volcanic edifices: constraints from Somma-Vesuvius, Etna and analog models. *Bull. Volcanol.*, 71(2):219–223, 2008.
- S. Albeverio, V. Jentsch, and H. Kantz. *Extreme Events in Nature and Society*. Springer, 2006.
- M.B. Allen, I. Herrera, and G.F. Pinder. *Numerical Modeling in Science and Engineering*. Wiley New York, 1988.
- E.G. Altmann and H. Kantz. Recurrence time analysis, long-term correlations, and extreme events. *Phys. Rev. E*, 71(5):56106, 2005.
- J. Åström, PCF Di Stefano, F. Pröbst, L. Stodolsky, J. Timonen, C. Bucci, S. Cooper, C. Cozzini, F. Feilitzsch, H. Kraus, et al. Fracture processes observed with a cryogenic detector. *Phys. Lett. A*, 356(4):262–266, 2006.
- M. Baiesi, M. Paczuski, and A.L. Stella. Intensity threshold and the statistics of the temporal occurrence of solar flares. *Phys. Rev. Lett.*, 96(5):051103, 2006.
- P. Bak, C. Tang, K. Wiesenfeld, et al. Self-organized criticality. *Phys. Rev. A*, 38(1):364–374, 1988.
- P. Bak, K. Chen, and C. Tang. A forest fire model and some thoughts on turbulence. *Phys. Lett. A*, 147:297–300, 1990.
- P. Bak, K. Christensen, L. Danon, and T. Scanlon. Unified scaling law for earthquakes. *Phys. Rev. Lett.*, 88(17):178501, 2002.
- M. S. Bebbington and C. D. Lai. On nonhomogeneous models for volcanic eruptions. *Math. Geol.*, 28(5):585–600, 1996a.
- M. S. Bebbington and C. D. Lai. Statistical analysis of New Zealand volcanic occurrence data. *J. Volcanol. Geotherm. Res.*, 74(1-2):101–110, 1996b.
- S. Blake. Volcanism and the dynamics of open magma chambers. *Nature*, 289:783–785, 1981.

- S.V. Buldyrev, A.L. Barabási, F. Caserta, S. Havlin, H.E. Stanley, and T. Vicsek. Anomalous interface roughening in porous media: Experiment and model. *Phys. Rev. A*, 45(12):8313–8316, 1992.
- M. H. Bulmer and J. B. Wilson. Comparison of flat-topped stellate seamounts on Earth’s seafloor with stellate domes on Venus using side-scan sonar and Magellan synthetic aperture radar. *Earth Planet. Sci. Lett.*, 171(2):277–287, 1999.
- K.V. Cashman, B. Sturtevant, P. Papale, and O. Navon. Magmatic fragmentation. In H. Sigurdsson, B. F. Houghton, S. R. McNutt, H. Rymer, and J. Stix, editors, *Encyclopedia of Volcanoes*, pages 421–430. Academic Press, San Fransisco, 2000.
- B. Chopard and M. Droz. *Cellular Automata Modeling of Physical Systems*, volume 122. Springer, 1998.
- R. Cioni, P. Marianelli, R. Santacroce, and A. Sbrana. Plinian and subplinian eruptions. In H. Sigurdsson, B. F. Houghton, S. R. McNutt, H. Rymer, and J. Stix, editors, *Encyclopedia of Volcanoes*, pages 477–494. Academic Press, San Fransisco, 2000.
- S.G Coles and R.S.J Sparks. Extreme value methods for modeling historical series of large volcanic magnitudes. In H.M. Mader, editor, *Statistics in Volcanology*, volume 1. Geological Society, 2006.
- Á. Corral. Local distributions and rate fluctuations in a unified scaling law for earthquakes. *Phys. Rev. E*, 68(3):035102, 2003. doi: 10.1103/PhysRevE.68.035102.
- Á. Corral, L. Telesca, and R. Lasaponara. Scaling and correlations in the dynamics of forest-fire occurence. *Phys. Rev. E*, 77(1):016101, 2008.
- Á. Corral, A. Ossó, and J.E. Llebot. Scaling of tropical-cyclone dissipation. *Nat. Phys.*, 6(9):693–696, 2010.
- D.R. Cox and P.A.W. Lewis. *The Statistical Analysis of Series of Events*. John Wiley and Sons, 1966.
- G.M. Crisci, S. Di Gregorio, R. Rongo, M. Scarpelli, W. Spataro, and S. Calvari. Revisiting the 1669 Etnean eruptive crisis using a cellular automata model and



- implications for volcanic hazard in the Catania area. *J. Volcanol. Geotherm. Res.*, 123(1-2):211–230, 2003. ISSN 0377-0273.
- L.S. Crumpler and J.C. Aubele. Volcanism on venus. In H. Sigurdsson, B. F. Houghton, S. R. McNutt, H. Rymer, and J. Stix, editors, *Encyclopedia of Volcanoes*, pages 697–708. Academic Press, San Fransisco, 2000.
- J. Davidsen, S. Stanchits, and G. Dresen. Scaling and universality in rock fracture. *Phys. Rev. Lett.*, 98(12):125502, 2007. doi: 10.1103/PhysRevLett.98.125502.
- S. De la Cruz-Reyna. Poisson-distributed patterns of explosive eruptive activity. *Bull. Volcanol.*, 54(1):57–67, 1991. doi: 10.1007/BF00278206.
- C. Del Negro, L. Fortuna, A. Herault, and A. Vicari. Simulations of the 2004 lava flow at Etna volcano using the magflow cellular automata model. *Bull. Volcanol.*, 70(7):805–812, 2008. ISSN 0258-8900.
- N. I. Deligne, S. G. Coles, and R. S. J Sparks. Recurrence rates of large explosive volcanic eruptions. *J. Geophys. Res.*, 115(B6):B06203, 2010.
- J. Dubois and J.L. Cheminee. Fractal analysis of eruptive activity of some basaltic volcanoes. *J. Volcanol. Geotherm. Res.*, 45(3-4):197–208, 1991.
- Y. Dzierma and H. Wehrmann. Statistical eruption forecast for the chilean southern volcanic zone: typical frequencies of volcanic eruptions as baseline for possibly enhanced activity following the large 2010 concepción earthquake. *Nat. Hazards. Earth Sys. Sci.*, 10:2093–2108, 2010.
- S.A. Fagents, T.K.P. Gregg, and R.M.C. Lopes. *Modeling Volcanic Processes: the Physics and Mathematics of Volcanism*. Cambridge University Press, 2013.
- H. Frey and M. Jarosewich. Subkilometer Martian volcanoes: Properties and possible terrestrial analogs. *J. Geophys. Res.*, 87(B12):9867–9879, 1982.
- J.S. Gilbert and R.S.J. Sparks. Future research directions on the physics of explosive volcanic eruptions. *Geol. Soc. London Spec. Publ.*, 145(1):1–7, 1998.
- J.R. Grasso and P. Bachelery. Hierarchical organization as a diagnostic approach to volcano mechanics: Validation on Piton de la Fournaise. *Geophys. Res. Lett.*, 22(21):2897–2900, 1995.

- A. Gudmundsson. How local stresses control magma chamber ruptures, dyke injections, and eruptions in composite volcanoes. *Earth Sci. Rev.*, 79(1):1–31, 2006.
- E.J. Gumbel. *Statistics of extremes*. Dover Pubns, 1958.
- A. A. Gusev. Temporal structure of the global sequence of volcanic eruptions: Order clustering and intermittent discharge rate. *Phys. Earth Planet. Inter.*, 166(3-4): 203–218, 2008. doi: 10.1016/j.pepi.2008.01.004.
- A. A. Gusev, V.V. Ponomareva, O. A. Braitseva, I. V. Melekestsev, and L. D. Sulerzhitsky. Great explosive eruptions on Kamchatka during the last 10,000 years: Self-similar irregularity of the output of volcanic products. *J. Geophys. Res.*, 108 (B2):2126, 2003. doi: 10.1029/2001JB000312.
- J. Hardy, O. De Pazzis, and Y. Pomeau. Molecular dynamics of a classical lattice gas: Transport properties and time correlation functions. *Phys. Rev. A*, 13(5):1949, 1976.
- J. W. Head. Lunar volcanism in space and time. *Rev. Geophys.*, 14(2):265–300, 1976.
- J. W. Head and A. Gifford. Lunar mare domes: Classification and modes of origin. *Moon Planets*, 22(2):235–258, 1980. doi: 10.1007/BF00898434.
- J.W. Head, S.L. Murchie, L.M. Prockter, S.C. Solomon, C.R. Chapman, R.G. Strom, T.R. Watters, D.T. Blewett, J.J. Gillis-Davis, C.I. Fassett, et al. Volcanism on mercury: Evidence from the first messenger flyby for extrusive and explosive activity and the volcanic origin of plains. *Earth Planet. Sci. Lett.*, 285(3):227–242, 2009.
- A. Helmstetter, S. Hergarten, and D. Sornette. Properties of foreshocks and aftershocks of the nonconservative self-organized critical Olami-Feder-Christensen model. *Phys. Rev. E*, 70(4):046120, 2004.
- C.H. Ho. Non homogeneous Poisson model for volcanic eruptions. *Math. Geol.*, 23 (2):167–173, 1991.
- C.H. Ho. Predictions of volcanic eruptions at mt vesuvius, italy. *J. Geodyn.*, 15(1): 13–18, 1992.

- C. Jaupart. Magma ascent at shallow levels. In H. Sigurdsson, B. F. Houghton, S. R. McNutt, H. Rymer, and J. Stix, editors, *Encyclopedia of Volcanoes*, pages 448–461. Academic Press, San Fransisco, 2000.
- F. W. Klein. Patterns of historical eruptions at Hawaiian volcanos. *J. Volcanol. Geotherm. Res.*, 12(1-2):1–35, 1982.
- T. Kusky. *Volcanoes: Eruptions and Other Volcanic Hazards*. Infobase Publishing, 2008.
- F. Lahaie and J.R. Grasso. A fluid-rock interaction cellular automaton of volcano mechanics: Application to the Piton de la Fournaise. *J. Geophys. Res.*, 103(B5): 9637–9649, 1998. ISSN 0148-0227.
- P. W. Lipman. Calderas. In H. Sigurdsson, B. F. Houghton, S. R. McNutt, H. Rymer, and J. Stix, editors, *Encyclopedia of Volcanoes*, pages 643–662. Academic Press, San Fransisco, 2000.
- J.R. Lister. Buoyancy-driven fluid fracture: Similarity solutions for the horizontal and vertical propagation of fluid-filled cracks. *J. Fluid Mech.*, 217:213–239, 1990.
- J.P. Lockwood and R. W. Hazlett. *Volcanoes: global perspectives*. John Wiley & Sons, 2010.
- R. Lopes-Gautier, A.S. McEwen, W.B. Smythe, P.E. Geissler, L. Kamp, A.G. Davies, J.R. Spencer, L. Keszthelyi, R. Carlson, F.E. Leader, et al. Active volcanism on Io: Global distribution and variations in activity. *Icarus*, 140(2):243–264, 1999.
- H.M. Mader, Y. Zhang, J.C. Phillips, R.S.J. Sparks, B. Sturtevant, and E. Stolper. Experimental simulations of explosive degassing of magma. *Nature*, 1994.
- H.M. Mader, M. Manga, and T. Koyaguchi. The role of laboratory experiments in volcanology. *J. Volcanol. Geotherm. Res.*, 129(1):1–5, 2004.
- W. Marzocchi and L. Zaccarelli. A quantitative model for the time-size distribution of eruptions. *J. Geophys. Res.*, 111(B4):B04204, 2006.
- O. Melnik. Dynamics of two-phase conduit flow of high-viscosity gas-saturated magma: large variations of sustained explosive eruption intensity. *Bull. of Volcano.*, 62(3):153–170, 2000.

- O. Melnik, A.A. Barmin, and R.S.J. Sparks. Dynamics of magma flow inside volcanic conduits with bubble overpressure buildup and gas loss through permeable magma. *J. Volcanol. Geotherm. Res.*, 143(1):53–68, 2005.
- A. T. Mendoza-Rosas and S. De la Cruz-Reyna. A mixture of exponentials distribution for a simple and precise assessment of the volcanic hazard. *Nat. Hazards Earth Syst. Sci.*, 9(2):425–431, 2009.
- C. G. Newhall and S. Self. The volcanic explosivity index (VEI) – An estimate of explosive magnitude for historical volcanism. *J. Geophys. Res.*, 87(C2):1231–1238, 1982.
- F. Nimmo and D. McKenzie. Volcanism and tectonics on venus. *Annu. Rev. Earth Pl. Sc.*, 26(1):23–51, 1998.
- Y. Ogata. Detection of precursory relative quiescence before great earthquakes through a statistical-model. *J. Geophys. Res.*, 97(B13):19845–19871, 1992.
- Z. Olami, H.J.S. Feder, and K. Christensen. Self-organized criticality in a continuous, nonconservative cellular automaton modeling earthquakes. *Phys. Rev. Lett.*, 68(8):1244, 1992.
- P. Papale. Strain-induced magma fragmentation in explosive eruptions. *Nature*, 397(6718):425–428, 1999.
- L. Parfitt and L. Wilson. *Fundamentals of physical volcanology*. John Wiley & Sons, 2009.
- J. D. Pelletier. Statistical self-similarity of magmatism and volcanism. *J. Geophys. Res.*, 104(B7):15425–15438, 1999.
- J.C. Phillips, S.J. Lane, A-M. Lejeune, and M. Hilton. Gum rosin-acetone system as an analogue to the degassing behaviour of hydrated magmas. *Bull. Volcanol.*, 57(4):263–268, 1995.
- E. Piegari, V. Cataudella, R. Di Maio, L. Milano, M. Nicodemi, and R. Scandone. A model of volcanic magma transport by fracturing stress mechanisms. *Geophys. Res. Lett.*, 35(6):L06308, 2008.

- E. Piegari, R. Di Maio, R. Scandone, and L. Milano. A cellular automaton model for magma ascent: Degassing and styles of volcanic eruptions. *J. Volcanol. Geotherm. Res.*, 202(1):22–28, 2011.
- E. Piegari, R. Di Maio, and R. Scandone. Analysis of the activity pattern of volcanoes through self-organized crack networks: The effect of density barriersan application to Vesuvius activity in the period 1631–1944. *Earth Planet. Sci. Lett.*, 2013.
- H. Pinkerton, L. Wilson, and R. MacDonald. The transport and eruption of magma from volcanoes: a review. *Contemp. Phys.*, 43(3):197–210, 2002.
- L.M. Prockter, C.M. Ernst, B.W. Denevi, C.R. Chapman, J.W. Head III, C.I. Fassett, W.J. Merline, S.C. Solomon, T.R. Watters, R.G. Strom, et al. Evidence for young volcanism on Mercury from the third MESSENGER flyby. *Science*, 329(5992): 668–671, 2010.
- D. M. Pyle. Forecasting sizes and repose times of future extreme volcanic events. *Geology*, 26(4):367–370, 1998.
- J. Radebaugh, L. P. Keszthelyi, A. S. McEwen, E. P. Turtle, W. Jaeger, and M. Mizzazzo. Paterae on Io: A new type of volcanic caldera? *J. Geophys. Res.*, 106(E12): 33005–33020, 2001.
- M. Rappaz, M. Bellet, M.O. Deville, and R. Snyder. *Numerical modeling in materials science and engineering*. Springer, 2003.
- R.A. Reyment. Statistical analysis of some volcanologic data regarded as series of point events. *Pure Appl. Geophys.*, 74(1):57–77, 1969.
- M.J. Rutherford and J.E. Gardner. Rates of magma ascent. In H. Sigurdsson, B. F. Houghton, S. R. McNutt, H. Rymer, and J. Stix, editors, *Encyclopedia of Volcanoes*, pages 207–218. Academic Press, San Fransisco, 2000.
- R. Scandone, K.V. Cashman, and S.D. Malone. Magma supply, magma ascent and the style of volcanic eruptions. *Earth Planet. Sci. Lett.*, 253(3):513–529, 2007.
- M. Settle and T.R. Mcgetchin. Statistical analysis of persistent explosive activity at stromboli, 1971: Implications for eruption prediction. *J. Volcanol. Geotherm. Res.*, 8(1):45–58, 1980.

- L. Siebert and T. Simkin. *Volcanoes of the World: An Illustrated Catalog of Holocene Volcanoes and their Eruptions*. Smithsonian Institution, Global Volcanism Program Digital Information Series, GVP-3, 2002-. <http://www.volcano.si.edu/world/>.
- H. Sigurdsson, B. F. Houghton, S. R. McNutt, H. Rymer, and J. Stix. *Encyclopedia of Volcanoes*. Academic Press, New York, 2000.
- T. Simkin. Terrestrial volcanism in space and time. *Annu. Rev. Earth Planet. Sci.*, 21:427–452, 1993.
- D. K. Smith. Comparison of the shapes and sizes of seafloor volcanoes on Earth and "pancake" domes on Venus. *J. Volcanol. Geotherm. Res.*, 73(1-2):47–64, 1996.
- P.D. Spudis. Volcanism on the moon. In H. Sigurdsson, B. F. Houghton, S. R. McNutt, H. Rymer, and J. Stix, editors, *Encyclopedia of Volcanoes*, pages 697–708. Academic Press, San Fransisco, 2000.
- J. Stix and J.C. Phillips. An analog investigation of magma fragmentation and degassing: Effects of pressure, volatile content, and decompression rate. *J. Volcanol. Geotherm. Res.*, 211:12–23, 2012.
- R.G. Strom, N.J. Trask, and J.E. Guest. Tectonism and volcanism on mercury. *J. Geophys. Res.*, 80(17):2478–2507, 1975.
- B. Taisne and C. Jaupart. Magma expansion and fragmentation in a propagating dike. *J. Volcanol. Geotherm. Res.*, 301(1):146–152, 2011.
- S. Tait and B. Taisne. The dynamics of dike propagation. In S.A. Fagents, T.K.P. Gregg, and R.M.C. Lopes, editors, *Modeling volcanic processes: the physics and mathematics of volcanism*, pages 32–54. Cambridge University Press, 2013.
- R.I. Tilling. Volcanic hazards and their mitigation: progress and problems. *Rev. Geophys.*, 27(2):237–269, 1989.
- D. L. Turcotte. *Fractals and Chaos in Geology and Geophysics*. Cambridge Univ. Press, Cambridge, 2nd edition, 1997.
- S. Vergnolle and M. Mangan. Hawaiian and strombolian eruptions. In H. Sigurdsson, B. F. Houghton, S. R. McNutt, H. Rymer, and J. Stix, editors, *Encyclopedia of Volcanoes*, pages 448–461. Academic Press, San Fransisco, 2000.

- 
- A. Vicari, H. Alexis, C. Del Negro, M. Coltelli, M. Marsella, and C. Proietti. Modeling of the 2001 lava flow at Etna volcano by a Cellular Automata approach. *Environ. Model. Softw.*, 22(10):1465–1471, 2007. ISSN 1364-8152.
- F. E. Wickman. Repose period patterns of volcanoes. I. Volcanic eruptions regarded as random phenomena. *Ark. Kem. Mineral. Geol.*, 4(4):291, 1966.
- L. Wilson. Volcanism in the solar system. *Nat. Geosci.*, 2(6):388–396, 2009. doi: 10.1038/ngeo529.
- S. Wolfram. *Theory and applications of cellular automata*. Advanced Series on Complex Systems, Singapore: World Scientific Publication, 1986.
- C. A. Wood. Calderas: A planetary perspective. *J. Geophys. Res.*, 89(B10):8391–8406, 1984.

# Chapter 2 Scaling Properties of Planetary Calderas<sup>1</sup>

## 2.1 Introduction

The formation of volcanoes and their corresponding eruption dynamics is a complex phenomenon and a major natural hazard on Earth. The surface expression of volcanism is a mirror to magma composition, eruption processes and tectonic processes [Wood, 1984]. Planetary exploration has shown that volcanism is or was operational on other solar system bodies such as Mars, Venus, Mercury, the Moon, Io, and several other planetary satellites [Wilson, 2009, Prockter et al., 2010].

Comparative planetology is the study of the morphology of geological features and their genesis, utilizing knowledge of analogous landforms on Earth. Past studies have attempted to compare volcanic structures on Earth to similar features on other planetary bodies with some success. Frey and Jarosewich [1982] investigated the size distributions of volcanic cones on Mars. By comparing their base diameters with volcanoes on Earth, they were able to conclude that small Martian cones could be analogs for Icelandic pseudocraters; while larger cones can be compared to terrestrial cinder cones. The size of flat topped "pancake" domes on Venus and flat topped seamount volcanoes on Earth were statistically compared and showed some differences, implying different formation conditions (magma composition, effusive rate, pressure, etc) [Smith, 1996]. Focusing more specifically on stellate planforms on Venus and flat-topped seamounts on Earth, Bulmer and Wilson [1999] were able to find some formation similarities. An important feature that is present on planetary bodies such as Mars, Venus, Earth and Io is the caldera. The importance of considering calderas in comparative planetology was emphasized by Wood [1984].

The definition for terrestrial caldera is "a large collapse depression, more or less circular or cirque-like in form, the diameter of which is many times greater than any

---

1. Published in *Nonlin. Proc. Geophys.*, 19(6):585-593, 2012



included vent” [Williams and McBirney, 1979]. They form from a roof collapse into a shallow magma chamber and their diameter is highly correlated with the volume of volcanic material involved in the eruption [Lipman, 2000]. Three main types of calderas can be identified on Earth [Wood, 1984]:

- Shield calderas result from a partial drainage of the chamber into a rift zone
- Stratocone calderas form by collapse of the magma chamber roof after a large eruption
- Ash flow calderas formation follows extremely large eruptions

Calderas can exhibit a large panel of features such as rings faults or collapse collar in response to the collapse process [Cole et al., 2005]. Those volcanic depressions are recognized in all volcanic environments: intraplate, convergent plate boundaries and mid-ocean ridges [Cole et al., 2005]. Their size on Earth can range from less than 1 km to 40 \* 75 km for the largest ones observed [Lipman, 2000].

An equivalent volcanic feature, which is found on Mars, Venus, and Io, and described as an irregular volcanic crater with scalloped edges is a patera. The general consensus in the interpretation of paterae on Venus and Mars is that they are analogs for calderas [Sigurdsson et al., 2000] and the largest known caldera/patera has been observed on Olympus Mons on Mars and displays a size of 80 \* 65 km [Mouginis-Mark and Robinson, 1992]. The morphology and the size distribution of paterae on Io have been compared to calderas on Earth, Mars and Venus and some similarities have been observed, indicating that paterae on Io might also be an analog for calderas. While our understanding of the formation mechanisms of these features remains at its early stage, Radebaugh et al. [2001] concluded that these paterae could be a hybrid between basaltic shield and mafic ash-flow calderas.

The increase in space remote sensing data has allowed planetary calderas to be studied and compared throughout the solar system in order to understand their formation processes. The geomorphology of Olympus Mons caldera was studied using high resolution images [Mouginis-Mark and Rowland, 2001]. Signs of extensional features at the boundaries of the caldera and compressional features at the center were used to infer that the related magma chamber was shallow [Mouginis-Mark and Rowland, 2001]. Using the Magellan satellite data, Cook et al. [1998] investigated large

landforms on Venus and the presence of calderas alongside with lava flows allowed them to infer rough volumes and geometries of magma chambers.

Important characteristics of calderas/paterae is their diameter and area which are related to the size of the underlying magma chamber and can be used as a proxy for estimating the potential of volcanic eruptions [Lipman, 2000]. The distribution of magma chamber sizes for planetary bodies is directly related to the crustal thickness and the properties of magma material such as density, concentration of volatiles, etc. [Mouginis-Mark and Rowland, 2001]. As a result, constraining the volcano forming and eruption processes would lead to a better understanding of the dynamical evolution of planetary interiors [Sobradelo et al., 2010]. Several numerical and analog models have been proposed to analyze and understand caldera-forming eruptions in the solar system [Kieffer, 1995, Acocella, 2007, and references therein].

Statistical studies have been carried out to analyze calderas on Earth. Sobradelo et al. [2010] performed ANOVA (analysis of variance) on the distribution of caldera areas in order to relate the size of calderas with various geodynamical settings. The analysis was successful at determining three distinct geodynamical environments that host small, medium and large calderas. Hughes and Mahood [2011] studied the spatial distribution of calderas in arc settings and were able to correlate the spatial distribution of calderas with the tectonic properties of arcs.

An alternative approach to statistically study volcanic processes is to look at the phenomenon as a whole, in order to develop a general framework applicable to all the volcanoes on Earth and in the solar system, independent of the volcano's crustal surrounding and geographical location. This type of global approach has been proven successful at defining scaling laws for the occurrence of other natural hazards such as forest fires [Corral et al., 2008], earthquakes [Corral, 2003, Shcherbakov et al., 2005], solar flares [Baiesi et al., 2006] and tropical cyclones [Corral et al., 2010]. This approach was also successfully used in analyzing the fracture of rocks [Davidsen et al., 2007]. Despite their complexity, volcanic processes can also be approximated by a point process in space and time. Using this approach several studies were undertaken to analyze global eruption time series. Gusev [2008] observed self-similar clustering in time and size for eruptions. It was also observed that large eruptions tend to occur during the most volcanically active periods. These characteristics of global volcanic activity lead to the conclusion that a global mechanism was responsible for the time/size clustering.

In this chapter, we investigate the universal properties of the size distribution of calderas in the solar system. Particularly, we consider the four planetary bodies: Earth, Mars, Venus, and Io. We also investigate the statistical properties of caldera sizes on Earth, by grouping them according to their surrounding crustal properties. We show that these distributions of caldera diameters and areas can be approximated by a universal functional form when they were rescaled with the corresponding sample averages. This approach allows us to conclude that the caldera formation is governed by similar processes throughout the solar system and is independent of crustal properties on Earth.

## 2.2 Solar System Bodies

For our analysis, we consider that paterae are analogs of volcanic calderas and therefore, we use the term caldera in the rest of the text. We extracted caldera size data from the Collapse Caldera Database (CCDB) [Geyer and Marti, 2008] for Earth, from the Magellan Venus volcanic feature catalog [Crumpler et al., 1997], and from the USGS astrogeology research program [<http://planetarynames.wr.usgs.gov/>, last consulted in December 2013]. For all the databases mentioned, we were able to obtain diameter values in kilometers. For the caldera diameters on Earth and Venus two measurements (minimum and maximum diameter) were reported in the catalogs whereas for Mars and Io only one measurement was reported assuming that calderas were circular in shape. In our analysis, we used the mean diameters for each caldera and also computed the areas of each caldera by assuming that they can be approximated by an ellipse except for the Earth where some actual areas of calderas were reported in the CCDB (see Table 2.1). When the minimum and the maximum diameters were given in the catalog, we computed the average value between the two.

To analyze the statistics of caldera sizes we constructed the probability density functions of caldera diameters and areas for each planetary body. Because multiple scales were involved (from a few kilometers to  $10^3$  kilometers and from hundreds of square meters to  $10^3$  square kilometers), we used logarithmically increasing bins over which we calculated the probability densities. We defined as  $x_n$  the coordinate of the right end of the  $n$ th bin ( $n = 0, 1, 2, \dots$ ). The coordinate  $x_{n+1}$  of the  $(n + 1)$ th bin was calculated recursively,  $x_{n+1} = bx_n$ , where  $b$  was a bin factor. The length of the  $n$ th bin was given by  $\Delta x_n = x_0(b^n - b^{n-1})$ . In our analysis the number of bins was

chosen for each distribution and the corresponding bin factors  $b$  were computed. The normalized probability density functions were calculated by dividing the number of occurrences within each bin by the corresponding bin length and the total number of data points considered. Due to the limited number of data points available for the Martian calderas the distribution contained only a few points. The distributions of diameters and areas for each planetary body considered are presented in Figure 2.1.

The constructed distributions display a similar behavior for all four bodies. There is a general power-law trend for large calderas and rollover and plateau for small diameters/areas. This change in the distributions can be attributed to different types of calderas present on those planetary bodies [Lipman, 2000]. Large calderas are usually formed through a plate (piston) or downsag subsidence, while small calderas frequently have funnel geometry and are associated with explosive eruptions through the central vent and a subsequent subsidence [Lipman, 2000, Acocella, 2007]. It is evident from Figure 2.1 that the distribution of caldera sizes on Earth is shifted to the left indicating the presence of smaller caldera sizes compared to the other planetary bodies. An explanation for this discrepancy can be related to the different caldera forming processes operating on those planetary bodies: on Earth, most calderas are formed around subduction zones and after large explosive (silicic) eruptions. On Mars, for example, there are no evidence of subduction zones and most volcanism is thought to be basaltic (non silicic). These factors can affect the size of the resulting calderas [Wood, 1984].

In order to compare the distributions, we performed a scaling analysis. We first calculated the sample averages  $D_n$  and  $A_n$  of caldera diameters and areas, where  $n$  enumerated a planetary body (the Earth, Mars, Venus, and Io). We then rescaled the individual probability density functions,  $P(d)$  and  $P(a)$ , according to

$$\bar{x} P(x) = f\left(\frac{x}{\bar{x}}\right), \quad (2.1)$$

where  $x \equiv d$  and  $\bar{x} \equiv D_n$  for the diameters and  $x \equiv a$  and  $\bar{x} \equiv A_n$  for the caldera areas, and  $f(y)$  is a scaling function. Figure 2.2 shows the resulting plots of the rescaled distributions. After rescaling the distributions using the mean diameter/area according to Eq. (2.1), we observed a good collapse of the data into a single functional form. In order to model this functional form, we tested 3 different heavy tailed distributions: the generalized Pareto distribution, the log-normal distribution and

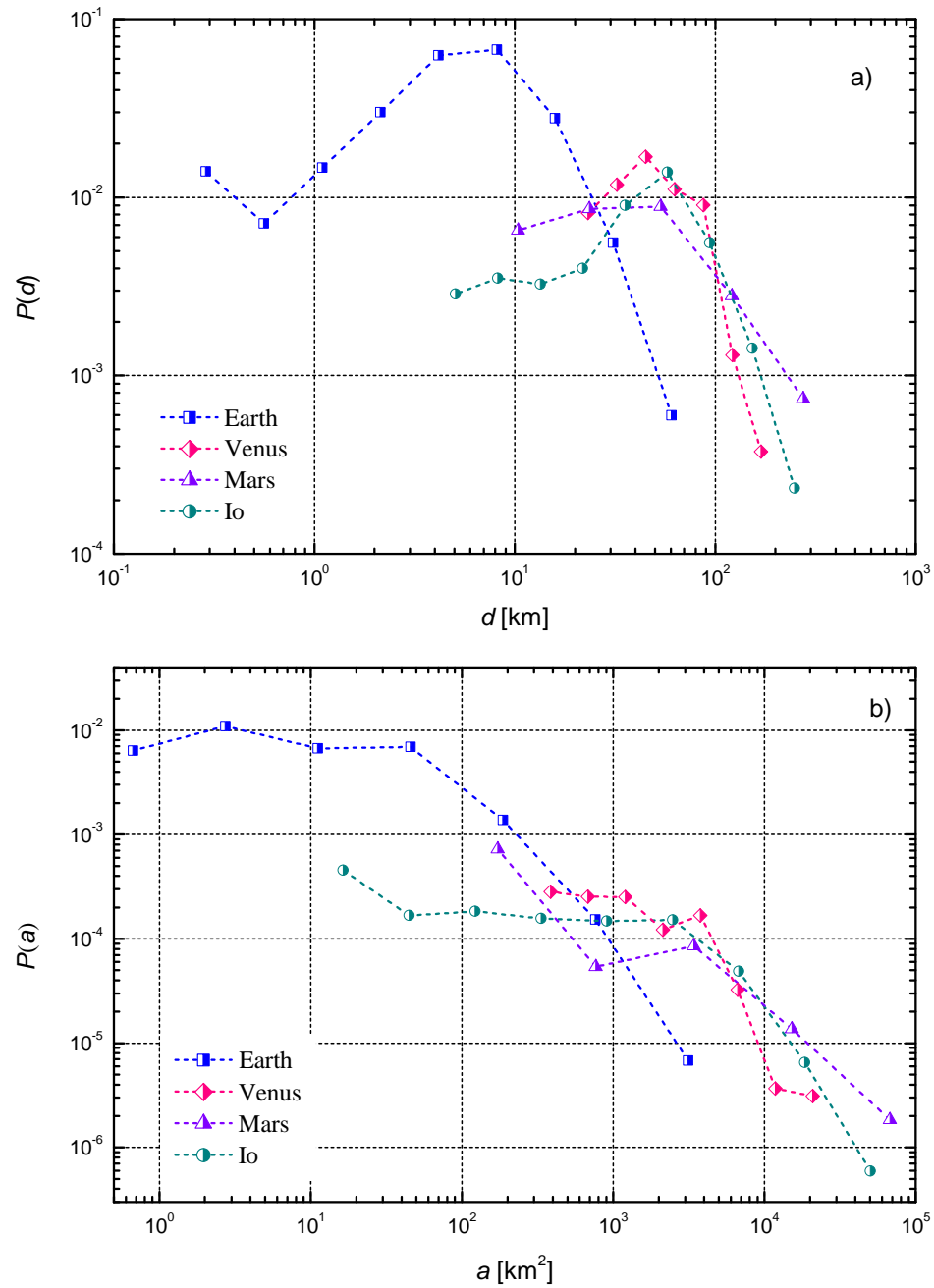


Figure 2.1: Distributions of caldera sizes for the Earth, Venus, Mars and Io. a) Caldera diameters in km, b) Caldera areas in  $\text{km}^2$ .

the generalized extreme value distribution (GEV). We estimated the parameters for each of them using the maximum likelihood method which is not affected by the varying bin sizes of the distributions. The maximum likelihood estimation was done using the Matlab software. In order to determine best fitting distribution to model the scaling function  $f(y)$ , we computed the Akaike information criterion (AIC) which provides a relative goodness of fit, taking into account the number of parameters in each model [Akaike, 1974]. If  $L$  is the maximum value of the likelihood function for a model described by  $k$  different parameters, then  $AIC = -2 \ln L + 2k$ . Smaller values of the AIC indicate a better fit.

The Earth data set contains significantly smaller caldera areas compared to the other planetary bodies considered. Because of erosion processes and vegetation on Earth, measuring and locating small features can be a difficult task which can lead to the underreporting of small calderas. We also observed a divergence of the data from the collapse for the small caldera areas. For these reasons, we performed the goodness of fit test for calderas/paterae with areas larger than  $30 \text{ km}^2$ . This cutoff only affects the Earth and Io data sets. The results of this test are given in Tables 2.2 and 2.3.

The obtained AIC values suggest that the GEV distribution provides the best fit for the collapsed data:

$$f(y) = \frac{1}{\sigma} u(y)^{-1-1/\theta} \exp \left[ -u(y)^{-1/\theta} \right], \quad (2.2)$$

where  $u(y) = 1 + \theta(y - \mu)/\sigma$  with the shape parameter  $\theta = 0.22 \pm 0.06$ , the location parameter  $\mu = 0.64 \pm 0.04$ , and the scale parameter  $\sigma = 0.42 \pm 0.03$  for the diameters (Figure 2.2a) and  $\theta = 0.84 \pm 0.11$ ,  $\mu = 0.26 \pm 0.03$ ,  $\sigma = 0.30 \pm 0.03$  for the areas (Figure 2.2b). The estimates of the parameters were calculated with a 95% confidence interval. The value of the shape parameter for the GEV distribution characterizes the tail of the distribution: if  $\theta > 0$ , the distribution displays heavy tail behavior as opposed to a light tail behavior when  $\theta = 0$  or a bounded tail if  $\theta < 0$ . Here, both distributions, for the diameters and the areas are heavy tail distributions. The mean value of the GEV distribution is defined as:  $\mu + \sigma \left[ \frac{\Gamma(1-\theta)-1}{\theta} \right]$  and is equal to 1 for both distributions by definition, because of the normalization process. The standard deviation is defined as:  $\sqrt{\frac{\sigma^2(g_2-g_1^2)}{\theta^2}}$  where  $g_k = \Gamma(1-k\theta)$  ( $\Gamma$  is the Gamma function) and is equal to 0.81 for the distribution of diameters and is undefined for the

Planetary body	#calderas	$D_n$ [km]	$A_n$ [km <sup>2</sup> ]
Earth	386	$12.6 \pm 1.1$	$205.6 \pm 48.4$
Venus	83	$62.3 \pm 6.8$	$3741.0 \pm 947.0$
Mars	19	$102.0 \pm 44.8$	$14615.0 \pm 1285.0$
Io	144	$72.7 \pm 7.4$	$5715.0 \pm 1430.0$
Continental crust	209		$289.7 \pm 42.3$
Oceanic crust	44		$111.3 \pm 57.0$
Transitional crust	85		$98.5 \pm 12.4$

Table 2.1: Summary of the data used for the planetary caldera analysis.  $D_n$  is the mean diameter and  $A_n$  is the mean caldera area computed from the minimum and maximum diameters assuming an elliptic shape for each planetary body except for the Earth where some caldera areas are estimated using the actual shape [Geyer and Marti, 2008]. The errors are given at 95% confidence intervals.

Distribution	$k$	$\ln L$	AIC
Generalized Pareto	2	-627.15	1258.29
Log-normal	2	-539.72	1083.45
Generalized Extreme Value	3	-521.85	1049.70

Table 2.2: The maximum values of the log-likelihood function ( $\ln L$ ) and the corresponding values of the Akaike Information Criterion (AIC) for the model distribution functions considered to fit the rescaled distributions given in Figure 2.2a.

Distribution	$k$	a) $\ln L$	AIC	b) $\ln L$	AIC
Generalized Pareto	2	-462.0	928.1	-213.8	431.6
Log-normal	2	-442.4	888.8	-192.6	389.2
Generalized Extreme Value	3	-435.4	876.9	-185.4	376.9

Table 2.3: The maximum values of the log-likelihood function ( $\ln L$ ) and the corresponding values of the AIC for the model distribution functions considered to fit a) the rescaled distributions given in Figure 2.2b and b) the rescaled distributions given in Figure 2.4.  $k$  is the number of parameters for the considered distribution. The values correspond to the fitting analysis considering only calderas/paterae with an area above 30 km<sup>2</sup>.

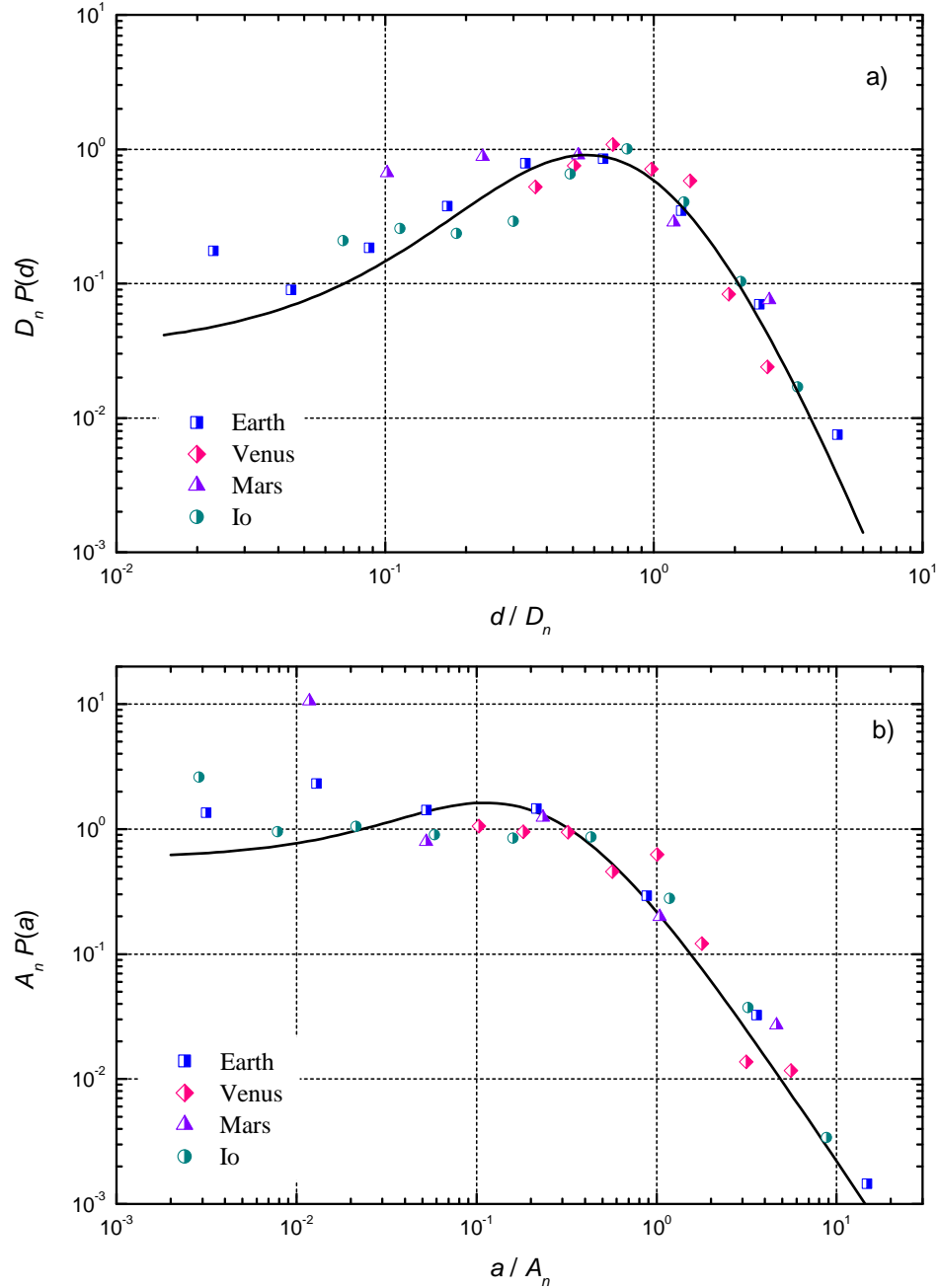


Figure 2.2: Rescaled caldera/paterae distributions for Earth, Mars, Venus and Io according to Eq. (2.1): a) rescaled diameters, with the mean diameter  $D_n$  computed for each planetary body (Table 2.1). The solid curve is a fit to the rescaled distributions and is given by the GEV distribution, Eq. (2.2), with  $\theta = 0.22 \pm 0.06$ ,  $\mu = 0.64 \pm 0.04$ , and  $\sigma = 0.42 \pm 0.03$ ; b) rescaled areas, with the mean area  $A_n$  computed for each planetary body (Table 2.1). The solid curve is a fit to the rescaled distributions and is given by the GEV distribution, Eq. (2.2), with  $\theta = 0.84 \pm 0.11$ ,  $\mu = 0.26 \pm 0.03$ , and  $\sigma = 0.30 \pm 0.03$



distribution of areas since  $\theta > 0.5$ . We observed a deviation from the data collapse for small values of diameters and areas. This discrepancy can be explained by the small number of data in the Martian catalog and by a possible misinterpretation of the smaller landforms for Io. Another explanation for this deviation from the collapse could be a different scaling form that applies to small caldera areas. It is important to note that a similar type of distribution, displaying a power-law tail and an exponential rollover was used to fit the distributions of three different landslides inventories [Malamud et al., 2004].

## 2.3 The Earth

We also investigated the scaling properties of caldera sizes on Earth according to their surrounding crustal properties. The CCDB provides size data for calderas worldwide as well as other characteristics such as plate tectonic settings, crustal type, world region, and rock type [Geyer and Marti, 2008]. For our analysis, we grouped the calderas according to 3 distinct crustal types: continental silicic crust, oceanic basaltic crust and transitional crust (see Table 2.1).

Using the same methodology, we computed the probability density distributions for each of the 3 data sets (Figure 2.3). We performed the scaling analysis using the mean caldera area as a scaling factor for each distribution (Figure 2.4). Comparably to planetary calderas, we observed a good collapse of all the distributions into a single functional form. Similarly to planetary calderas, we only focused on areas larger than  $30 \text{ km}^2$ . After testing the generalized Pareto distribution, the log-normal distribution and the GEV distribution as fits for the rescaled distributions (see Table 2.3), we found that the best AIC value was obtained for the GEV distribution, Eq. (2.2) with  $\theta = 0.94 \pm 0.16$ ,  $\mu = 0.22 \pm 0.04$ , and  $\sigma = 0.28 \pm 0.05$ . The estimates of the parameters were calculated with a 95% confidence interval. We note that for this scaling analysis and for the one using the planetary data sets, the GEV parameters are similar within the error limits. We observe a departure from the collapse for small values in the case of the Earth calderas, which could be explained by incompleteness of the catalog or by a different scaling form for small calderas.

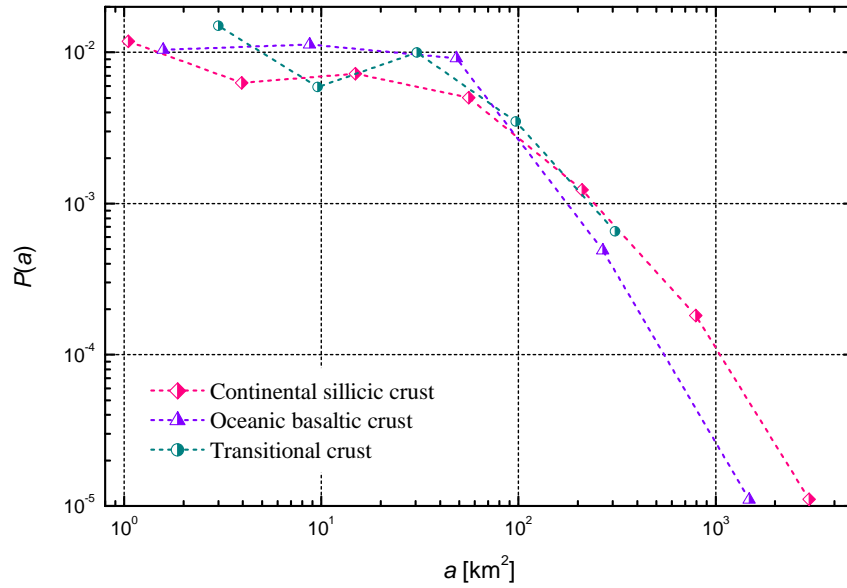


Figure 2.3: Probability density functions of caldera areas for three separate crustal types on Earth.

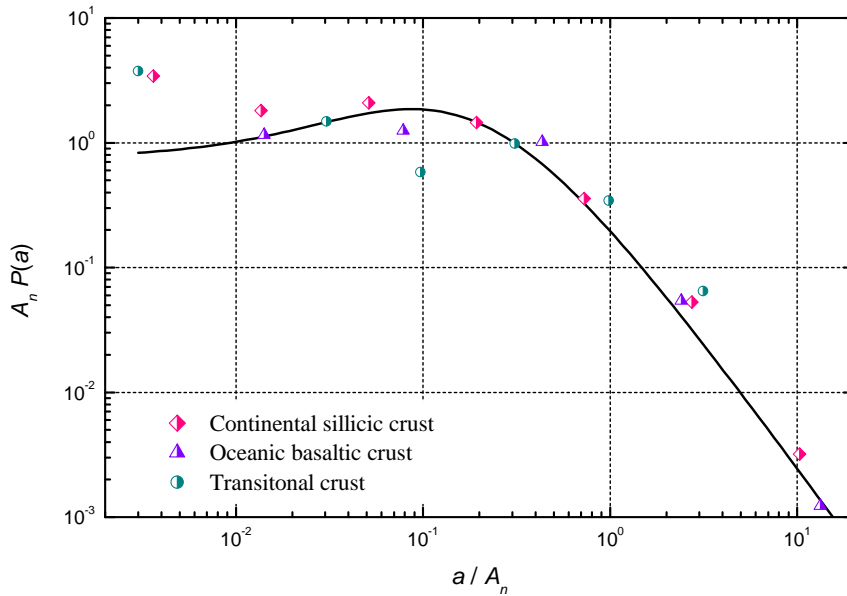


Figure 2.4: Rescaled caldera areas distributions for the three crustal types according to Eq. (2.1) with the mean area  $A_n$  computed for each crustal type (Table 2.1). The solid curve is a fit to the rescaled distributions and is given by the GEV distribution, Eq. (2.2), with  $\theta = 0.94 \pm 0.16$ ,  $\mu = 0.22 \pm 0.04$ , and  $\sigma = 0.28 \pm 0.05$ .

## 2.4 Conclusions

Calderas are formed by the collapse of the edifice of the erupting volcanoes into partially drained magma chambers. Their sizes are related to the complex processes that build the original volcanoes, to the propagation of the rising magma through the host crustal rock, and to the size of the magma chamber itself. Therefore, the caldera size distribution is an important characteristics that can be used to infer and constrain the geodynamical processes operating on planetary bodies.

Using the proposed scaling analysis, we have shown that the distributions of caldera diameters and areas on Earth, Mars Venus and Io can be described as a universal function, the Generalized Extreme Value (GEV) distribution. We also analyzed the distribution of caldera sizes on Earth by grouping them into 3 distinct crustal types: continental silicic crust, oceanic basaltic crust and transitional crust. We showed that their distributions were described by the same GEV distribution. The obtained parameters of the GEV distribution for planetary calderas and for the calderas on Earth with distinct crustal types were similar within error limits. This inferred scaling implies that the dynamic processes responsible for caldera formation are similar for the Earth, Mars, Venus, and Io and are quite independent of the crustal settings on Earth. The mean caldera/patera diameters and areas play the role of characteristic sizes for each of the distributions. This result has important implications for physical constraints on any realistic model describing the volcano formation and eruption. In this context, the comparative planetology is a powerful approach that can help to further understand caldera formation in the solar system.

## References

- V. Acocella. Understanding caldera structure and development: An overview of analogue models compared to natural calderas. *Earth. Sci. Rev.*, 85(3-4):125–160, 2007.
- H. Akaike. A new look at the statistical model identification. *IEEE Trans. Autom. Contr.*, 19(6):716–723, 1974.
- M. Baiesi, M. Paczuski, and A.L. Stella. Intensity threshold and the statistics of the temporal occurrence of solar flares. *Phys. Rev. Lett.*, 96(5):051103, 2006.
- M. H. Bulmer and J. B. Wilson. Comparison of flat-topped stellate seamounts on Earth’s seafloor with stellate domes on Venus using side-scan sonar and Magellan synthetic aperture radar. *Earth Planet. Sci. Lett.*, 171(2):277–287, 1999.
- J.W. Cole, D.M. Milner, and K.D. Spinks. Calderas and caldera structures: a review. *Earth Sci. Rev.*, 69(1):1–26, 2005.
- D.L. Cook, D.L Chambers, N.W. Grosfils, L. Reinen, M.J. Gilmore, and S.J. Kozak. Volume, geometry, and depth of magma chambers associated with large volcanoes on venus. volume 29. Lunar and Planetary Science Conference, 1998.
- Á. Corral. Local distributions and rate fluctuations in a unified scaling law for earthquakes. *Phys. Rev. E*, 68(3):035102, 2003. doi: 10.1103/PhysRevE.68.035102.
- Á. Corral, L. Telesca, and R. Lasaponara. Scaling and correlations in the dynamics of forest-fire occurrence. *Phys. Rev. E*, 77(1):016101, 2008.
- Á. Corral, A. Ossó, and J.E. Llebot. Scaling of tropical-cyclone dissipation. *Nat. Phys.*, 6(9):693–696, 2010.
- L. S. Crumpler, J. C. Aubele, and J. W. Head III. The tabulated Magellan Venus volcanic feature catalog, 1997. [http://www.planetary.brown.edu/planetary/databases/venus\\_cat.html](http://www.planetary.brown.edu/planetary/databases/venus_cat.html).
- J. Davidsen, S. Stanchits, and G. Dresen. Scaling and universality in rock fracture. *Phys. Rev. Lett.*, 98(12):125502, 2007. doi: 10.1103/PhysRevLett.98.125502.

- H. Frey and M. Jarosewich. Subkilometer Martian volcanoes: Properties and possible terrestrial analogs. *J. Geophys. Res.*, 87(B12):9867–9879, 1982.
- A. Geyer and J. Marti. The new worldwide collapse caldera database (CCDB): A tool for studying and understanding caldera processes. *J. Volcanol. Geotherm. Res.*, 175(3):334–354, 2008. doi: 10.1016/j.jvolgeores.2008.03.017.
- A. A. Gusev. Temporal structure of the global sequence of volcanic eruptions: Order clustering and intermittent discharge rate. *Phys. Earth Planet. Inter.*, 166(3-4): 203–218, 2008. doi: 10.1016/j.pepi.2008.01.004.
- <http://planetarynames.wr.usgs.gov/>. USGS astrogeological program, last consulted in December 2013.
- G.R. Hughes and G.A. Mahood. Silicic calderas in arc settings: Characteristics, distribution, and tectonic controls. *Geol. Soc. Am. Bull.*, 123(7-8):1577–1595, 2011.
- S. W. Kieffer. Numerical models of caldera-scale volcanic eruptions on Earth, Venus, and Mars. *Science*, 269(5229):1385, 1995.
- P. W. Lipman. Calderas. In H. Sigurdsson, B. F. Houghton, S. R. McNutt, H. Rymer, and J. Stix, editors, *Encyclopedia of Volcanoes*, pages 643–662. Academic Press, San Fransisco, 2000.
- B.D. Malamud, D.L. Turcotte, F. Guzzetti, and P. Reichenbach. Landslide inventories and their statistical properties. *Earth Surf. Proc. Land.*, 29(6):687–711, 2004.
- Peter J Mouginiis-Mark and Mark S Robinson. Evolution of the olympus mons caldera, mars. *Bull. Volcanol.*, 54(5):347–360, 1992.
- P.J. Mouginiis-Mark and S.K Rowland. The geomorphology of planetary calderas. *Geomorphology*, 37:201–223, 2001.
- L.M. Prockter, C.M. Ernst, B.W. Denevi, C.R. Chapman, J.W. Head III, C.I. Fassett, W.J. Merline, S.C. Solomon, T.R. Watters, R.G. Strom, et al. Evidence for young volcanism on Mercury from the third MESSENGER flyby. *Science*, 329(5992): 668–671, 2010.

- J. Radebaugh, L. P. Keszthelyi, A. S. McEwen, E. P. Turtle, W. Jaeger, and M. Mizzotto. Paterae on Io: A new type of volcanic caldera? *J. Geophys. Res.*, 106(E12): 33005–33020, 2001.
- R. Shcherbakov, G. Yakovlev, D. L. Turcotte, and J. B. Rundle. Model for the distribution of aftershock interoccurrence times. *Phys. Rev. Lett.*, 95:218501, 2005. doi: 10.1103/PhysRevLett.95.218501.
- H. Sigurdsson, B. F. Houghton, S. R. McNutt, H. Rymer, and J. Stix. *Encyclopedia of Volcanoes*. Academic Press, New York, 2000.
- D. K. Smith. Comparison of the shapes and sizes of seafloor volcanoes on Earth and "pancake" domes on Venus. *J. Volcanol. Geotherm. Res.*, 73(1-2):47–64, 1996.
- R. Sobradelo, A. Geyer, and J. Martí. Statistical data analysis of the CCDB (collapse caldera database): Insights on the formation of caldera systems. *J. Volcanol. Geotherm. Res.*, 198(1-2):241–252, 2010.
- H. Williams and A.R. McBirney. *Volcanology*. Freeman, Cooper, San Francisco, Calif, 1979.
- L. Wilson. Volcanism in the solar system. *Nat. Geosci.*, 2(6):388–396, 2009. doi: 10.1038/ngeo529.
- C. A. Wood. Calderas: A planetary perspective. *J. Geophys. Res.*, 89(B10):8391–8406, 1984.

# Chapter 3 Statistical Analysis of the Size Distribution of Impact Craters<sup>1</sup>

## 3.1 Introduction

High velocity impacts of asteroids or comets onto the surface of a rocky planetary body result in the formation of craters [Grieve, 2006]. A large amount of energy is transferred from the impactor to the surface of the impacted body and is divided between kinetic energy and internal energy, which lead to crater formation and shock metamorphism, respectively [Grieve, 2006]. The cratering process induces the excavation of deep materials in the form of ejecta and uplifts, making impact craters a unique site to explore planetary subsurfaces [Osinski and Pierazzo, 2012]. The increase in space exploration activities enabled the collection of a large amount of data on impact craters, allowing extensive studies on this type of landform. Space missions such as Magellan (Venus, 1989 to 1994), Messenger (Mercury, launches in 2004), Lunar Reconnaissance Orbiter (LRO, 1966 to 1967) and Mars Reconnaissance Orbiter (MRO, 2005) complemented the already large datasets of impact craters characteristics obtained from ground based telescope observations [<http://nssdc.gsfc.nasa.gov/planetary/projects.html>, last consulted in January 2014].

Impact craters constitute the most common surface landform on rocky planetary bodies, with the exception of Earth [Osinski and Pierazzo, 2012]. They can exhibit several morphological types: simple, transitional and complex craters. Simple craters are defined by a characteristic bowl shape and a small diameter [Stöffler et al., 2006]. Larger diameter craters, or complex craters, have a smaller depth to diameter ratio than simple craters and display a topographic high at their center. They are also characterized by complex rims affected by faulting from gravitational adjustments [Osinski and Pierazzo, 2012]. Transitional craters can be found on the Moon and Mars. While they do not display the central topographic high, they show

---

1. Submitted to Earth and Planetary Science Letters

some precursors of structures that are well developed in complex craters [Stöffler et al., 2006]. The largest impact craters take the form of multi-ring basins, where concentric scarps surround the structure [Osinski and Pierazzo, 2012]. The statistical study of the size and spatial distribution of impact craters in the solar system helps to find information on the planetary surface such as age, evolution and erosion, but also history of impactors in the solar system [Hartmann, 1995]. Impact craters are governed by the laws of physics and acting processes are the same for all targets [Melosh, 1989], but some differences arise for different planetary bodies due to drastically different planetary environments. Planetary gravity for example will have an effect on the size of craters, with a lower gravity leading to deeper and larger diameter structures [Stöffler et al., 2006].

On the Moon, the absence of an atmosphere and the low acting gravity increases the impact efficiency for a given impact [Stöffler et al., 2006]. Simple craters have a diameter  $D < 15$  km, complex craters are found in the range  $15 < D < 375$  km and impact basins have a diameter  $D > 400$  km [Stöffler et al., 2006]. One of the earliest statistical studies on lunar craters examined the cumulative distribution function of diameters in several regions and found that the distribution displayed a power-law behavior of the form  $N \sim D^\alpha$  where  $N$  is the number of craters with a diameter larger than  $D$  and  $\alpha$  is a constant [Young, 1940]. The exponent  $\alpha$  of the power-law was found to be dependent on the diameter with a value of  $-3$  for large diameters and  $-1.5$  for small diameters. Using data from the lunar orbiters Ranger 7, 8 and 9, Cross [1966] investigated the frequency size distribution of crater diameters in the size range 1 m to 70 km. The results suggested a single power-law behavior for all diameters considered, with an exponent of  $-2$ . The difference in values for the power-law exponent was explained by the magnification limits of the photographs used by Young [1940]. Arguing the fitting method in the previous studies, Chapman and Haefner [1967] showed a continuing variation in the exponent value with increasing diameter, results which were supported by Neukum et al. [1972]. Using an adapted database which accounts for the factors modifying crater sizes (effects of flooding, secondary cratering, etc), Neukum et al. [1975] defined a unified expression for the frequency size distribution of craters. This law was described by a power-law where the slope is a function of crater size,  $\alpha(D)$ . Taking advantage of the increase in planetary data quality, Head et al. [2010] used the high precision topographic measurements acquired by the Lunar Orbiter Laser Altimeter (as part of the Lunar Reconnaissance Orbiter,



<http://nssdc.gsfc.nasa.gov/planetary/projects.html> [last consulted in January 2014]) in order to produce a complete catalog of large lunar impact craters ( $D \geq 20$  km). Analyzing their population statistics, they found that the frequency size distributions of craters displayed different characteristics between the older highland and younger mare regions. This supports the hypothesis that two distinct categories of impactors affected the lunar surface [Strom et al., 2005]. The impacts occurring during the Late Heavy Bombardment (LHB) seem to be responsible for the distribution characterizing the oldest regions. The youngest regions display a different distribution, which corresponds to craters formed after the LHB [Strom et al., 2005, Head et al., 2010]. All the studies point toward the possibility of a power-law distribution of crater diameters, but no consensus has been reached as to how the exponent evolves for craters of all diameters and regions.

There are currently 184 confirmed impact structures on Earth (Earth Impact Database, [www.passc.net/EarthImpactDatabase/](http://www.passc.net/EarthImpactDatabase/), last consulted January 2014). Simple and complex craters have been found on Earth and the transition between those two features seems to occur for diameters between 2 and 4 km [Osinski and Pierazzo, 2012]. Active tectonics and extensive erosion erases surface records of impacts [Osinski and Pierazzo, 2012]. The smallest structures are often buried or completely removed from the geological record. The shielding effect of the atmosphere also prevents small impactors to reach the surface [Neukum and Ivanov, 1994]. These processes introduce a bias in the frequency size distribution of terrestrial impact craters. Grieve [2006] investigated the frequency size distribution of craters on Earth and uncovered a power-law relationship similar to the one found for the Moon ( $N \sim D^\alpha$ ) with an exponent  $\alpha = -2$ . This relationship seems to only hold for  $D > 20$  km, the distribution falls off for smaller craters. This rollover behavior can be explained by the removal or burial of smaller craters by erosion processes.

The atmosphere on Mars is thinner than the one on Earth but complex geological processes can modify the cratering record [Carr, 2006]. Similarly to the Moon, there seems to be no definite agreement in the literature about the shape of the frequency-size distribution of craters on Mars [Neukum and Ivanov, 1994]. A power-law distribution with  $\alpha = -2$  was observed by Hartmann [1973], only for a small range of diameters. The distribution displays a steeper slope ( $\alpha > -3$ ) for small craters [Carr, 2006]. A possible reason for the absence of a uniform frequency size distribution is the difference in upper crustal rocks composition, which could affect

the distribution of Martian geological features [Carr and Clow, 1981].

The frequency size distribution of craters on Mercury displays similarities with Lunar and Martian crater size distributions [Strom and Neukum, 1988, Strom et al., 2008]. More specifically, two main components emerge from these frequency size distributions. One follows a power-law distribution with  $\alpha = -2$ , interpreted to describe the population of craters formed during the LHB, the other one displays a slope of  $-3$  and is believed to represent latter events [Strom et al., 2008]. Acting processes such as faulting and volcanism degrade crater shapes on Mercury [Strom et al., 2008].

With its high gravity and thick atmosphere, the cratering efficiency on Venus is much lower than on the Moon, Mars and Mercury [Schultz, 1993]. Analysis from the early Venera mission data pointed out the lack of small craters on the Venusian surface [Ivanov et al., 1986]. Data obtained from the Magellan mission's radar confirmed this deficiency and Phillips et al. [1991] proposed the thick atmosphere as a possible cause. Indeed, the kinetic energy of small impactors can largely decrease during their travel through the thick atmosphere. Phillips et al. [1992] proposed a transit model in order to estimate the smallest crater diameter affected by the numbers deficiency due to the effect of the atmosphere. It was found that craters with a diameter  $D > 30$  km were not affected by atmospheric filtering. Neukum and Ivanov [1994] investigated the frequency size distribution of Venusian craters and found a power-law distribution similar to the one for lunar craters for  $D > 20$  km. The distribution of smaller sizes displayed a rollover.

From all aforementioned studies, it is clear that some power-law distribution can be used to approximate the frequency size distribution of impact craters. There seems to be no clear consensus as to what size ranges in the crater size distribution are behaving as a power-law. In this chapter, we investigate the scaling properties of impact craters frequency size distributions for the Moon, Earth, Mars, Mercury and Venus. We aim at finding a common distribution to describe the population of impact craters for a large size range throughout the inner solar system. This type of global approach has been proven successful at defining scaling laws for the occurrence of other natural hazards such as forest fires [Corral et al., 2008], earthquakes [Corral, 2003, Shcherbakov et al., 2005], solar flares [Baiesi et al., 2006] and tropical cyclones [Corral et al., 2010]. The size of planetary calderas has also been investigated using a statistical scaling analysis and a common distribution was found to describe this

landform on several planetary bodies [Sanchez and Shcherbakov, 2012]. Strom et al. [2008] pointed out that the frequency size distributions of impact craters on Mars, Mercury and the Moon "match each other better if shifted somewhat in diameter". Here, we use the mean diameter of each distribution as a scaling factor: we rescale both axes using this quantity in order to obtain dimensionless axes. We observe a shift and a reasonable collapse of all the distributions into a single one, with some deviation for small craters. In order to lower this deviation from the single distribution, we investigate the value of a diameter cutoff. We find that large impact craters on Mars, the Moon, Mercury and Venus present the same statistical characteristics while large craters on Earth seem to deviate from this common distribution. We conclude that large impact craters on Mars, the Moon, Mercury and Venus possess the same formation and evolution characteristics. Small craters on Venus behave differently due to an important atmospheric filtering effect. Impact craters on Earth seem to evolve dissimilarly. We hypothesize that the active tectonics and heavy erosional processes found on Earth are responsible for the difference in crater size distributions.

## 3.2 Scaling Analysis

For the statistical analysis of crater sizes, we extracted impact crater diameters from the USGS astrogeology research program [<http://planetarynames.wr.usgs.gov/>, last consulted in December 2013] for Mars, Mercury, Venus and the Moon. The Earth Impact Database [<http://www.passc.net/EarthImpactDatabase/>, last consulted in December 2013] provided us with impact diameters on Earth defined as the length from rim to rim of the impact structure. All the diameters collected were recorded in kilometers. A summary of the data is presented in Table 3.1.

In most of the previous analyses of impact crater sizes, the cumulative size distribution function was used in order to determine the statistical characteristics of this planetary feature. Here, we will investigate the probability density function (normalized histogram, or PDF). Because multiple scales are involved (from a few meters to hundreds of kilometers), we used logarithmically increasing bins over which we calculated the probability densities. We defined as  $x_n$  the coordinate of the right end of the  $n$ th bin ( $n = 0, 1, 2, \dots$ ). The coordinate  $x_{n+1}$  of the  $(n + 1)$ th bin was calculated recursively,  $x_{n+1} = bx_n$ , where  $b$  was a bin factor. The length of the  $n$ th bin was given by  $\Delta x_n = x_0(b^n - b^{n-1})$  [Sanchez and Shcherbakov, 2012]. In order

to compute the probability density function for each planetary body, we counted the number of craters within each diameter bin and divided this number by the bin length and the total number of craters in the dataset. The number of bins was chosen individually for each dataset. The probability density functions for the five planetary bodies considered and all crater sizes is presented in Figure 3.1.

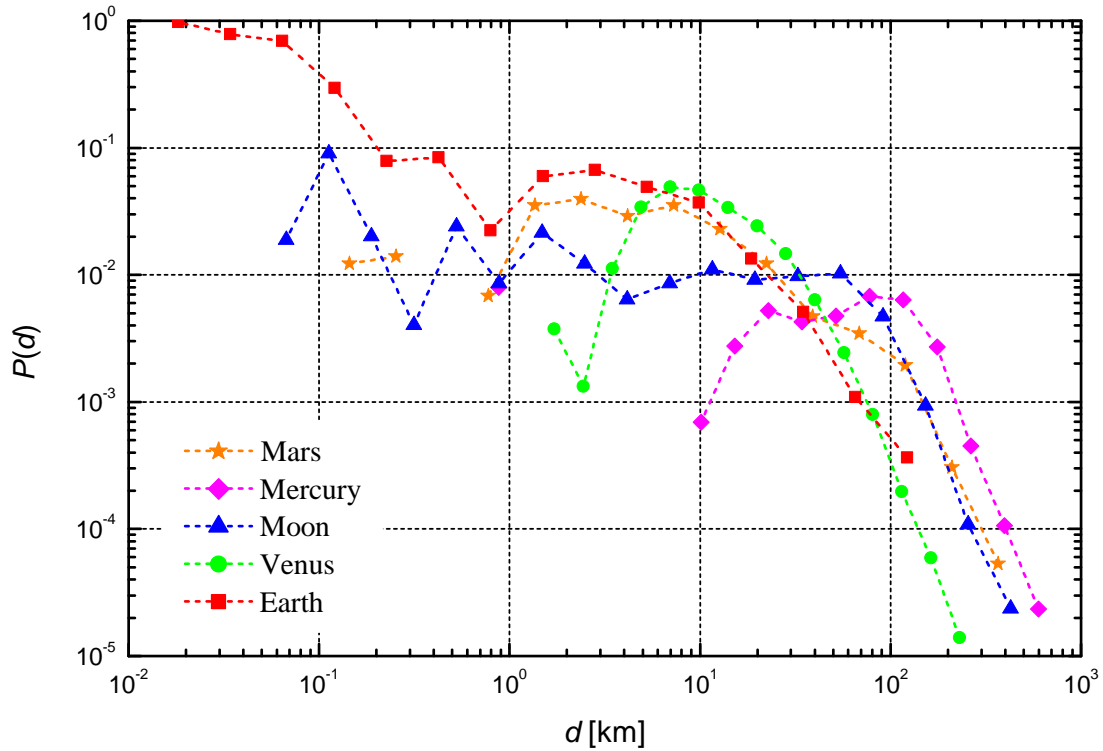


Figure 3.1: Distributions of crater diameters in km for Mars, Mercury, the Moon, Venus and Earth.

We can observe a common trend in all the distributions, with a power-law regime for large impact craters and a more complex behavior for smaller features. The curves for Mars, Mercury and Venus exhibit a rollover for small craters. The distribution of small craters on Earth displays a rollover for intermediate sizes and an increase in the probability of smaller craters ( $D < 1$  km). This transition might be representative of the change in distribution between simple and complex craters on Earth which is hypothesized to occur between 2 and 4 km [Osinski and Pierazzo, 2012]. The PDF

of impact craters on the Moon displays a similar "disrupted rollover" for diameters smaller than approximately 10 km. This behavior might also be explained by the transition between simple and complex craters which may occur around  $D = 15$  km [Stöffler et al., 2006].

In order to perform the scaling analysis and compare all the distributions together, we calculated the sample averages  $D_n$  for each of the distributions considered where  $n$  is the planetary body and rescaled each PDF  $P(d)$  individually according to:

$$D_n P(d) = f\left(\frac{d}{D_n}\right), \quad (3.1)$$

where  $d$  is the diameter and  $D_n$  is the mean diameter for each distribution  $n$  and  $f(x)$  is a scaling function. The result of this scaling is presented in Figure 3.2.

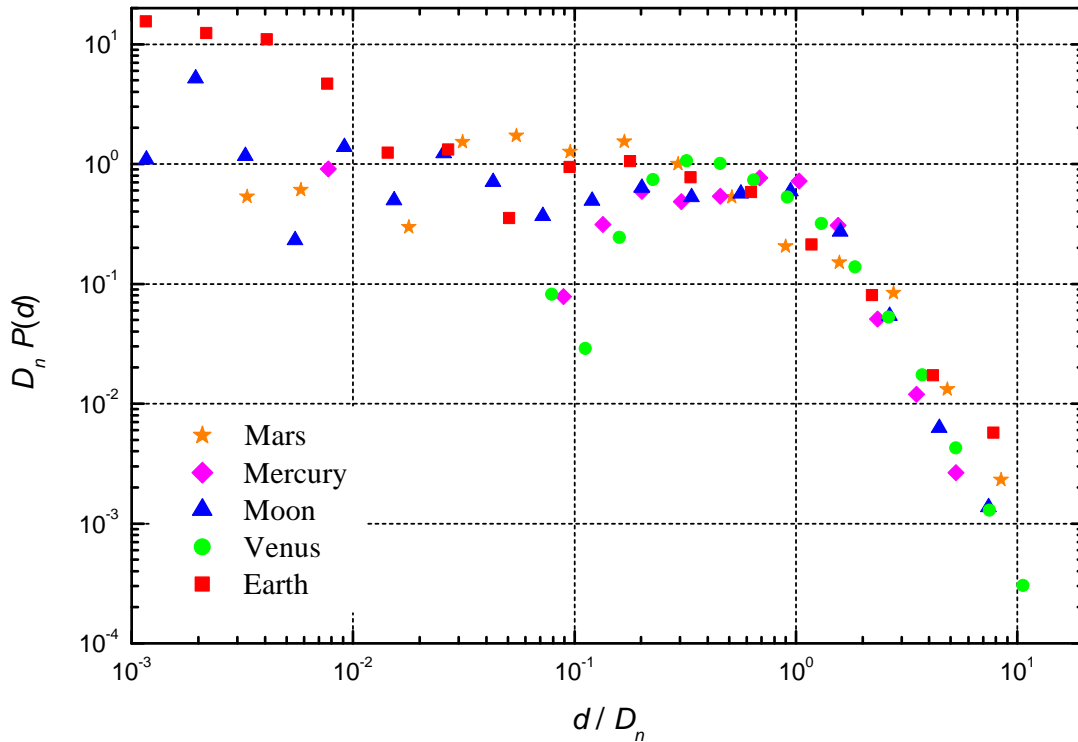


Figure 3.2: Rescaled distributions of crater diameters according to Eq. (3.1), with  $D_n$  computed for each planetary body (see Table 3.1).

After scaling, we observe a good collapse of all the distributions for large diameter values and a large deviation from this collapse for the smaller diameter values. This behavior shows that the processes responsible for the formation and the evolution of large impact craters on the bodies considered are similar while small impact craters seem to undergo different formation and evolution mechanisms. The deviation from the collapse for small features might also be due to the statistical bias introduced by the destruction of small craters from erosion and tectonic processes.

In order to investigate the similarities in the statistical properties of impact craters for the 5 bodies considered and the characteristics of the scaling function  $f(x)$ , we isolated the large craters according to previous studies. We introduced a size cutoff for each dataset. For the Earth, the value of the size cutoff was chosen at 5 km in order to consider the PDF of complex craters as opposed to a mix between simple and complex features. For Venus, the cutoff was set at 30 km in order to consider craters unaffected by the atmospheric effects [Phillips et al., 1992]. A threshold of 10 km was chosen for Mars and Mercury according to results from Hartmann [1973] and Strom et al. [2008] showing a change in statistical behavior for larger craters. The smallest diameters considered for the Moon was set at 30 km for the same reasons [Head et al., 2010] and also to ensure that we considered only complex craters [Stöffler et al., 2006]. Figure 3.3 shows the probability density function for each planetary body for the diameters above the defined cutoffs.

Figure 3.4 displays the rescaled distributions according to Eq. (3.1). We observe a better collapse of all the distributions together with still some deviation for smaller diameter values, specially for the Earth dataset. In order to find the scaling function  $f(x)$ , we tested three heavy tailed distributions:

- the generalized Pareto distribution (with  $\theta = 0$ ):

$$f(x) = \frac{1}{\sigma} \left[ 1 + \theta \left( \frac{x - \mu}{\sigma} \right) \right]^{-\frac{1}{\theta+1}}, \quad (3.2)$$

- the log-normal distribution:

$$f(x) = \frac{1}{x \sigma \sqrt{2\pi}} \exp \left[ -\frac{(\ln(x) - \mu)^2}{2\sigma^2} \right], \quad (3.3)$$

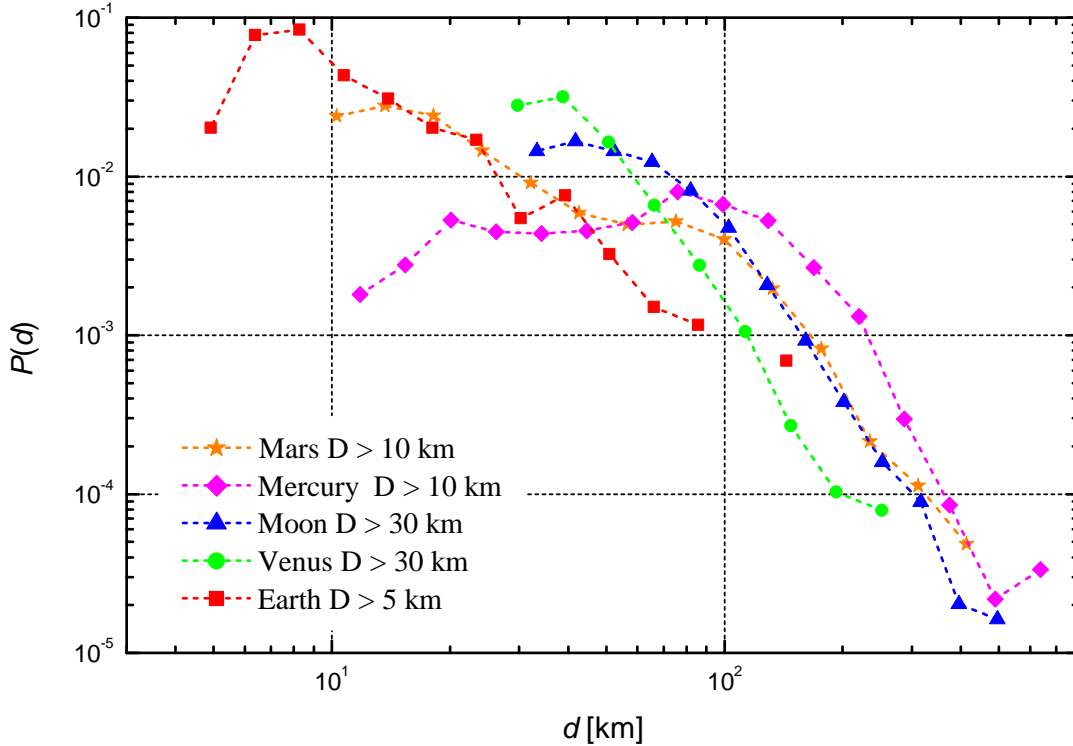


Figure 3.3: Distributions of crater diameters in km for Mars, Mercury, the Moon, Venus and Earth after size cutoff.

- the Generalized Extreme Value distribution (GEV)

$$f(x) = \frac{1}{\sigma} u(x)^{-1-1/\theta} \exp \left[ -u(x)^{-1/\theta} \right], \quad (3.4)$$

(where  $u(x) = 1 + \theta(x - \mu)/\sigma$  )

We estimated the parameters for each of them using the maximum likelihood method which is not affected by the varying bin sizes of the distributions. In order to determine the best fitting distribution to model the scaling function  $f(x)$ , we computed the Akaike information criterion (AIC) which provides a relative goodness of fit, taking into account the number of parameters in each model [Akaike, 1974]. If  $L$  is the maximum value of the likelihood function for a model described by  $k$  different parameters, then  $AIC = -2 \ln L + 2k$ . Smaller values of the AIC indicate a better

fit. The results of the test are compiled in Table 3.2.

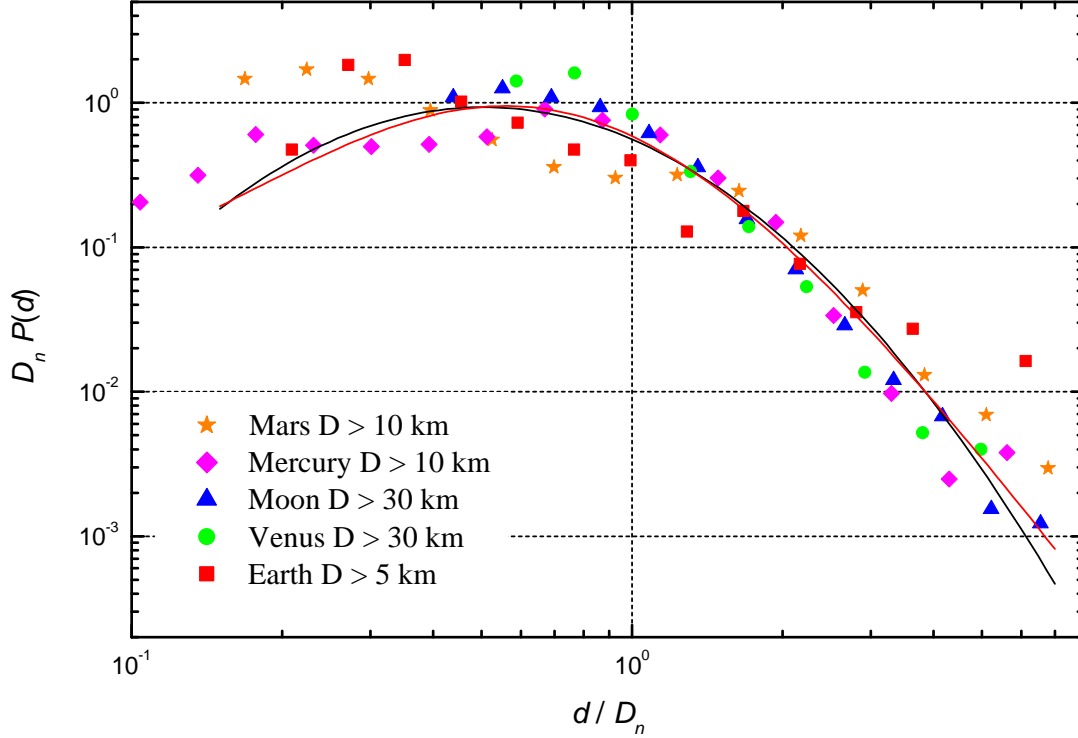


Figure 3.4: Rescaled distributions of crater diameters according to Eq. (3.1), with given size cutoff. The solid black curve is a fit to the rescaled distributions and is given by the log-normal distribution, Eq. (3.3), with  $\mu = -0.23 \pm 0.03$  and  $\sigma = 0.67 \pm 0.02$ . The solid red curve is a fit to the rescaled distribution and is given by the GEV distribution, Eq. (3.4), with  $\theta = 0.25 \pm 0.04$ ,  $\mu = 0.65 \pm 0.02$ , and  $\sigma = 0.40 \pm 0.02$ .

The results of the fitting analysis imply that the log-normal distribution is the best fit for the scaling function with  $\mu = -0.23 \pm 0.03$  and  $\sigma = 0.67 \pm 0.02$ . The parameters were calculated with a 95% confidence interval. It is important to notice that the AIC values are very close for the log-normal and the GEV fits and the tail of these two functions are very similar.

As noted by Strom et al. [2008], the distributions of impact crater sizes are very similar for Mars, Mercury and the Moon, specially for large diameters. From Figure 3.3, we can observe that these distributions are particularly close for craters larger than 100 km. The size distribution of impact craters larger than 30 km on



Venus (therefore not affected by the atmospheric effect) is also very similar to Mars, Mercury and the Moon. We performed the scaling analysis on those 4 bodies with  $D > 100$  km for Mars, Mercury and the Moon and  $D > 30$  km for Venus (the number of craters with  $D > 100$  km was insufficient for the Venus dataset). The results of the scaling are presented in Figure 3.5 and the results of the fitting analysis are presented in Table 3.3.

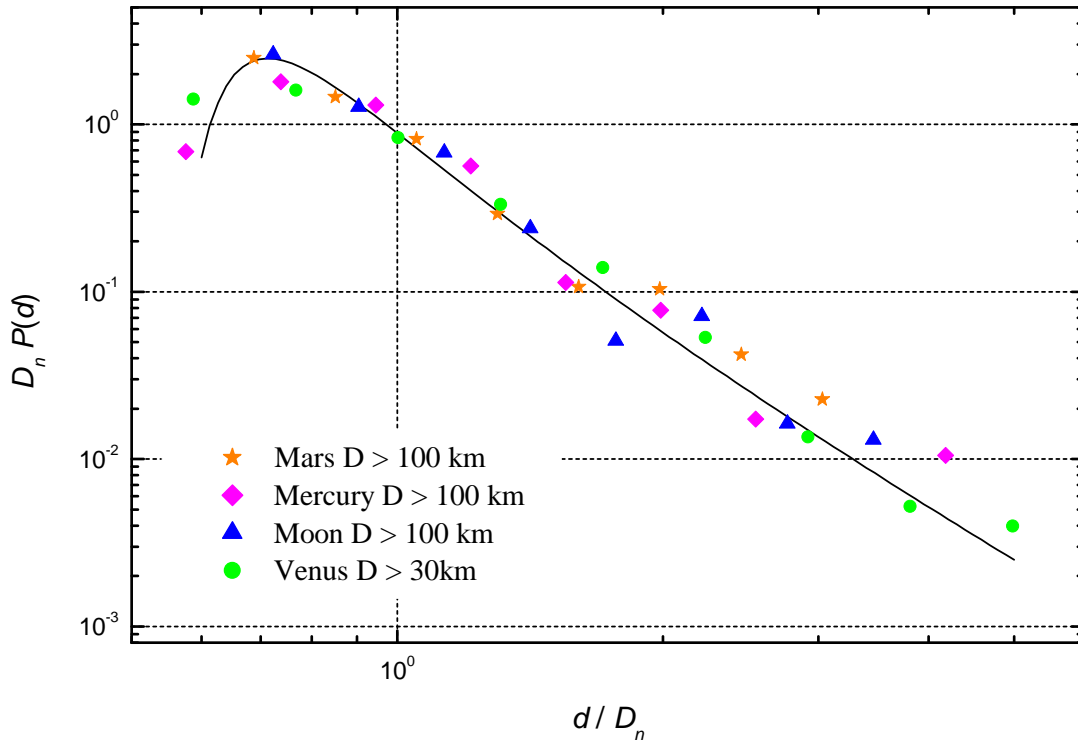


Figure 3.5: Rescaled distributions of crater diameters for Mars, Mercury, the Moon and Venus according to Eq. 3.1. The solid black curve is a fit to the rescaled distributions and is given by the GEV distribution, Eq. (3.4), with  $\theta = 0.51 \pm 0.08$ ,  $\mu = 0.78 \pm 0.01$ , and  $\sigma = 0.17 \pm 0.01$ .

The best fit for the scaling function  $f(x)$  here is the GEV distribution with  $\theta = 0.51 \pm 0.08$ ,  $\mu = 0.78 \pm 0.01$ , and  $\sigma = 0.17 \pm 0.01$ . The shape parameter  $\theta$  of the GEV distribution characterizes its tail behavior. Here,  $\theta > 0$  implies a heavy tail behavior for the distribution. We can observe from Figure 3.5 the power-law trend of

Planetary body	#craters	$D_n$ [km]	$D_{\min}$ [km]	$D_{\max}$ [km]
Earth	184	$15.7 \pm 3.5$	0.01	160
Venus	895	$21.7 \pm 1.3$	2	270
Mars	1034	$43.4 \pm 3.4$	0.1	467.3
Mercury	355	$113.2 \pm 8.1$	0.9	716.1
Moon	1565	$57.6 \pm 2.5$	0.06	536.4

Table 3.1: Summary of the data used for the planetary impact crater analysis.  $D_n$  is the mean diameter,  $\text{Min}_n$  and  $\text{Max}_n$  are the smallest and largest diameters respectively. The errors on the mean are given at 95% confidence intervals.

Distribution	$k$	$\ln L$	AIC
Generalized Pareto	2	-2453.32	4910.65
Log-normal	2	-1971.53	3947.07
Generalized Extreme Value	3	-1978.99	3963.99

Table 3.2: The maximum values of the log-likelihood function ( $\ln L$ ) and the corresponding values of the Akaike Information Criterion (AIC) for the model distribution functions considered to fit the rescaled distributions given in Figure 3.4

Distribution	$k$	$\ln L$	AIC
Generalized Pareto	2	-672.73	1349.47
Log-normal	2	-208.66	421.315
Generalized Extreme Value	3	-53.49	112.98

Table 3.3: The maximum values of the log-likelihood function ( $\ln L$ ) and the corresponding values of the Akaike Information Criterion (AIC) for the model distribution functions considered to fit the rescaled distributions given in Figure 3.5

this tail. We note that the GEV distribution has also been used to fit the distribution of landslide inventories [Malamud et al., 2004] and planetary calderas [Sanchez and Shcherbakov, 2012].

### 3.3 Conclusions

Impact cratering is a prominent phenomenon in our solar system. The formation and evolution of impact craters are dependent, amongst other processes, on the size of the impactors as well as the physical planetary conditions on the impacted body. Craters can display different morphological characteristics, ranging from simple bowl-shaped craters to heavily faulted complex crater or multi-ring basins. Multiple impacting periods, comprising the Late Heavy Bombardment and impacts occurring after, might also be responsible for the variability in size distribution of impact craters [Head et al., 2010, Strom et al., 2005, 2008].

In this study, we proposed a scaling analysis to uncover similarities in formation and evolution mechanisms of impact craters on Earth, Mars, Mercury, the Moon and Venus. Considering all crater sizes, we rescaled the probability density functions of diameters for all the bodies considered using the mean diameter of each distribution as a scaling factor. We found similarities in the tail of the distribution but a large deviation from the collapse of the data for small features. For the Earth, this deviation could be attributed to the difference in statistical behavior for simple and complex craters as well as the bias introduced by active tectonics and erosion which tends to erase craters of all sizes. On the Moon, the shape of the probability density function for small craters could be explained by that same difference between simple and complex craters. This result would confirm that the transition between simple and complex structures occurs around 10–15 km for the Moon and around 1–5 km for the Earth. Concerning lunar craters, the hypothesis of two separate bombardment periods might also explain the change in the probability density function between small and large craters. For Venus, this deviation could be due to the atmospheric filtering effect for small impactors. For Mars and Mercury, the rollover of the distribution could be explained by the two bombardment periods hypothesis.

After defining a size cutoff for our analysis, we found that the 5 distributions display a reasonable collapse into a single curve that can be approximated by a log-Normal distribution. A deviation from the collapse is still noticeable for small values

of the distributions and for the Earth's distribution in general. We conclude that the erosion and tectonic effects on Earth are greatly affecting the size distribution of craters, and influencing the shape of the collapse toward a log-normal distribution. When considering only large craters from Mars, Mercury, the Moon and Venus, we found a much better collapse of the distributions, implying that the processes acting for the formation and evolution of large impact craters on Mars, Mercury, the Moon and Venus are similar. The mean diameter for each of the datasets considered acts as a characteristic size for each of the distributions. This result confirms the hypothesis that the crater size distributions for Mars, Mercury and the Moon are similar if shifted by a scaling parameter (here, the mean diameter  $D_n$ ) [Strom et al., 2008] and expands it by including Venusian craters. These results have important implications in the investigation of the formation and evolution mechanisms of impact craters in the solar system.

## References

- H. Akaike. A new look at the statistical model identification. *IEEE Trans. Autom. Contr.*, 19(6):716–723, 1974.
- M. Baiesi, M. Paczuski, and A.L. Stella. Intensity threshold and the statistics of the temporal occurrence of solar flares. *Phys. Rev. Lett.*, 96(5):051103, 2006.
- M. H. Carr. *The surface of Mars*. Cambridge Univ. Press, Cambridge, 2006.
- M.H. Carr and G.D. Clow. Martian channels and valleys: Their characteristics, distribution, and age. *Icarus*, 48(1):91–117, 1981.
- C.R. Chapman and R.R. Haefner. A critique of methods for analysis of the diameter-frequency relation for craters with special application to the moon. *J. Geophys. Res.*, 72(2):549–557, 1967.
- Á. Corral. Local distributions and rate fluctuations in a unified scaling law for earthquakes. *Phys. Rev. E*, 68(3):035102, 2003. doi: 10.1103/PhysRevE.68.035102.
- Á. Corral, L. Telesca, and R. Lasaponara. Scaling and correlations in the dynamics of forest-fire occurrence. *Phys. Rev. E*, 77(1):016101, 2008.
- Á. Corral, A. Ossó, and J.E. Llebot. Scaling of tropical-cyclone dissipation. *Nat. Phys.*, 6(9):693–696, 2010.
- C.A. Cross. The size distribution of lunar craters. *Monthly Notices of the Royal Astronomical Society*, 134:245, 1966.
- Earth Impact Database, last consulted in December 2013. <http://www.passc.net/EarthImpactDatabase/>.
- R.A. Grieve. *Impact structures in Canada*. St. John’s, NL: Geological Association of Canada, 2006.
- W.K. Hartmann. Martian cratering, 4, mariner 9 initial analysis of cratering chronology. *J. Geophys. Res.*, 78(20):4096–4116, 1973.
- W.K. Hartmann. Planetary cratering 1. the question of multiple impactor populations: Lunar evidence. *Meteoritics*, 30(4):451–467, 1995.

- J.W. Head, C.I. Fassett, S.J. Kadish, D.E. Smith, M.T. Zuber, G.A. Neumann, and E. Mazarico. Global distribution of large lunar craters: Implications for resurfacing and impactor populations. *Science*, 329(5998):1504–1507, 2010.
- <http://nssdc.gsfc.nasa.gov/planetary/projects.html>. NASA planetary missions, last consulted in January 2014.
- <http://planetarynames.wr.usgs.gov/>. USGS astrogeological program, last consulted in December 2013.
- B.A. Ivanov, A.T. Basilevsky, V.P. Kryuchkov, and I.M. Chernaya. Impact craters of venus: Analysis of venera 15 and 16 data. *J. Geophys. Res.*, 91(B4):413–430, 1986.
- B.D. Malamud, D.L. Turcotte, F. Guzzetti, and P. Reichenbach. Landslide inventories and their statistical properties. *Earth Surf. Proc. Land.*, 29(6):687–711, 2004.
- H.J. Melosh. Impact cratering: A geologic process. *Research supported by NASA. New York, Oxford University Press (Oxford Monographs on Geology and Geophysics, No. 11), 1989, 253 p.*, 1, 1989.
- G. Neukum and B.A. Ivanov. Crater size distributions and impact probabilities on earth from lunar, terrestrial-planet, and asteroid cratering data. In *Hazards due to Comets and Asteroids*, volume 1, page 359. The University of Arizona Press, 1994.
- G. Neukum, E. Schneider, A. Mehl, D. Storzer, G.A. Wagner, H. Fechtig, and M.R. Bloch. Lunar craters and exposure ages derived from crater statistics and solar flare tracks. In *Lunar and Planetary Science Conference Proceedings*, volume 3, page 2793, 1972.
- G. Neukum, B. König, and J. Arkani-Hamed. A study of lunar impact crater size-distributions. *The Moon*, 12(2):201–229, 1975.
- G.R. Osinski and E. Pierazzo. Chapter one: Impact cratering: processes and products. In G.R. Osinski and E. Pierazzo, editors, *Impact cratering: processes and products*. John Wiley & Sons, 2012.
- R.J. Phillips, R.E. Arvidson, J.M. Boyce, D.B. Campbell, J.E. Guest, G.G. Schaber, and L.A. Soderblom. Impact craters on venus: Initial analysis from magellan. *Science*, 252(5003):288–297, 1991.

- R.J. Phillips, R.F. Raubertas, R.E. Arvidson, I.C. Sarkar, R.R. Herrick, N. Izenberg, and R.E. Grimm. Impact craters and venus resurfacing history. *J. Geophys. Res.*, 97(E10):15923–15948, 1992.
- L. Sanchez and R. Shcherbakov. Scaling properties of planetary calderas and terrestrial volcanic eruptions. *Nonlinear Proc. in Geoph.*, 19(6):585–593, 2012.
- P.H. Schultz. Impact crater growth in an atmosphere. *Int. J. of Impact Eng.*, 14(1): 659–670, 1993.
- R. Shcherbakov, G. Yakovlev, D. L. Turcotte, and J. B. Rundle. Model for the distribution of aftershock interoccurrence times. *Phys. Rev. Lett.*, 95:218501, 2005. doi: 10.1103/PhysRevLett.95.218501.
- D. Stöffler, G. Ryder, B.A. Ivanov, N.A. Artemieva, M.J. Cintala, and R.A.F. Grieve. Cratering history and lunar chronology. *Rev. Mineral. Geochem.*, 60(1):519–596, 2006.
- R.G. Strom and G. Neukum. The cratering record on mercury and the origin of impacting objects. *Mercury*, pages 336–373, 1988.
- R.G. Strom, R. Malhotra, T. Ito, F. Yoshida, and D.A. Kring. The origin of planetary impactors in the inner solar system. *Science*, 309(5742):1847–1850, 2005.
- R.G. Strom, C.R. Chapman, W.J. Merline, S.C. Solomon, and J.W. Head. Mercury cratering record viewed from messenger’s first flyby. *Science*, 321(5885):79–81, 2008.
- J. Young. A statistical investigation of diameter and distribution of lunar craters. *J. Brit. Astron. Assoc.*, 50(9):309–326, 1940.

# Chapter 4 Temporal Scaling of Volcanic Eruptions<sup>1</sup>

## 4.1 Introduction

Volcanic eruptions are outcomes of complex processes that operate in the upper mantle and crust when magma reaches the surface of the Earth. They constitute a major natural hazard on Earth especially in the areas with significant population density. Therefore, understanding the processes taking place in the magma chamber and surrounding crust that lead to an eruption is of fundamental importance. A typical approach to studying volcanoes involves examination of their structures, tectonic settings and associated eruptive activities. Statistical analysis is a powerful tool that can be used to identify patterns and correlations in the occurrence of volcanic eruptions. The first statistical analyses of eruption time series were performed on individual volcanoes in Hawaii and groups of volcanoes in Japan [Wickman, 1966, Klein, 1982]. Since then, stochastic models and various distributions have been proposed on selected volcanoes such as homogeneous and non-homogeneous Poisson models [De la Cruz-Reyna, 1991, Ho, 1991, Salvi et al., 2006], Weibull renewal model for volcanoes in New Zealand [Bebbington and Lai, 1996], or a mixture of exponential distributions [Mendoza-Rosas and De la Cruz-Reyna, 2009]. Rank-ordering power-law statistics was used to predict the repose time of extreme volcanic eruptions and the method was applied to the Taupo volcano [Pyle, 1998]. The frequency-magnitude statistics of historical recurrence rates of large explosive eruptions was analyzed using extreme value theory [Deligne et al., 2010]. The temporal structure of global sequences of explosive eruptions in Kamchatka was analyzed and self-similar clustering and episodicity were observed [Gusev et al., 2003]. Clustering was also observed on the onsets of volcanic eruptions and their statistical behavior was modeled using a trend renewal process [Bebbington, 2010].

---

1. Pulished in *J. Volcanol. Geotherm. Res.*, 247-248:115121, 2012. doi:10.1016/j.jvolgeores.2012.08.004



A promising approach to study volcanism is to look at the phenomenon as a whole in order to develop a general framework applicable to all the volcanoes, independent of the volcano's type and geographical location. This type of statistical analysis has been successfully applied to other natural hazards and several scaling laws, implying that the triggering mechanism operates the same way at broad spatial and temporal scales have been proposed in studies of seismicity [Corral, 2003], forest fires [Corral et al., 2008], solar flares [Baiesi et al., 2006], tropical cyclones [Corral et al., 2010] and in the occurrence of rock fracturing [Davidsen et al., 2007, Åström et al., 2006]. Similarly to the aforementioned processes, volcanism operates through nonlinear threshold dynamics. Despite this complexity, one can consider volcanic eruptions as a point process in space and time. In addition, the distribution of magnitudes and/or Volcanic Explosivity Index (VEI) of volcanic eruptions, displays scale-invariant characteristics [Newhall and Self, 1982, De la Cruz-Reyna, 1991, Simkin, 1993, Gusev et al., 2003]. The cumulative distribution of the annual amount of tephra produced by eruptions also exhibits power-law behavior [Turcotte, 1997]. A few statistical analyses have been performed on global data sets of volcanic eruptions. Gusev [2008] observed self-similar clustering in time and size for eruptions. It was also observed that large eruptions tend to occur during the most volcanically active periods. These characteristics of global volcanic activity lead to the conclusion that a global mechanism was responsible for the time/size clustering. Marzocchi and Zaccarelli [2006] observed two different regimes concerning interevent times: short times are clustered and can be explained by an open conduit system while long interevent times show random behavior, that can be characterized by a Poisson process and explained by a closed conduit system. These two regimes were also associated with different rhythms in magmatic intrusions [Dubois and Cheminee, 1991].

In this chapter, we analyzed the scaling properties of volcanic eruptions on Earth. For this purpose, we considered eruptive histories of the 26 most active volcanoes as well as eruptions of 163 less active volcanoes around the world. The volcanoes were also analyzed by grouping them into 9 geographical regions as well as into 4 volcano types: calderas, complex volcanoes, shield volcanoes, and stratovolcanoes. We computed the distributions of interevent times between successive eruptions for all the eruption data sets considered. The scaling analysis was performed to quantify their universal properties. This was accomplished by using the corresponding mean interevent time of each data set as a scaling factor. A collapse of all the distributions

into a single functional form for interevent times lead us to conclude that the processes responsible for volcanic eruptions on Earth were similar and quite independent of the type of volcanism and geographical location.

## 4.2 Volcanic Eruption Data

A time interval between two successive volcanic eruptions, or an interevent time, is an important characteristic of volcano dynamics [Marzocchi and Zaccarelli, 2006, Deligne et al., 2010]. When one studies the distribution of interevent times it is crucial to define what constitutes the onset of an eruption. Here, we consider the onset as the time of the arrival of volcanic products at the Earth's surface. This includes explosive ejection of fragmental material or effusion of previously liquid lava. To analyze the interevent time distributions of eruptions, we extracted eruptive histories of volcanoes on Earth from the Smithsonian Institution global eruption catalog [Siebert and Simkin, 2002-] and assembled them into separate data sets. For each individual volcano data set, we computed the time intervals  $\Delta t$  between successive eruptions as  $\Delta t_i = t_i - t_{i-1}$ , with  $t_i$  being the time onset of the  $i$ th eruption. For the analysis, we ignored the eruption duration but instead measured the interevent time between the onset of one eruption and the onset of the subsequent eruption.

The incompleteness of the catalogs is an important issue that had to be addressed in our analysis. Indeed, the number of reported volcanic eruptions has dramatically increased in the past 500 years [Simkin, 1993]. This is mainly due to the development of modern tools and methods for monitoring and detection of volcanic activities. Previous studies of individual and combined volcanic catalogs have addressed the problem of incompleteness with some success [Marzocchi and Zaccarelli, 2006, Bebbington, 2010, Deligne et al., 2010]. To ensure that the catalogs considered in our analysis were complete and that our estimates of the interevent times were not biased by incompleteness, we introduced a cutoff date for older eruptions for each of the considered eruption sequences. The cutoff date was determined specific to each volcano sequence considered. For this type of data, as stated before, the older the eruption date, the less reliable it was. We chose the cutoff date for each volcano by detecting when the data became less reliable based on the number of uncertain dates and changes in the mean rate of eruptions. This method might not fully account for uncertain or missing eruption dates, but at present, there is no truly reliable

technique to validate the completeness of the volcanic eruption catalogs to ensure sufficient data for the analysis. In comparison, when studying earthquake interevent times, one often introduces a lower magnitude cutoff in the catalogs to address their incompleteness. In our case, we were dealing with the eruptive history of individual volcanoes, and even small eruptions represent the outcome of complex processes occurring in the magma chamber and could not be ignored in our analysis. In addition, the Volcanic Explosivity Index (VEI) [Newhall and Self, 1982] used as an estimate of the eruption's magnitude only takes into account the explosive component of an eruption and ignores the volume of lava produced by effusive eruptions. However, to analyze the scaling of interevent times with respect to the lower magnitude cutoff we also considered different VEI cutoffs in our study.

For our analysis, we considered the individual eruption sequences of 26 prominent volcanoes around the world (Table 4.1). We selected these individual volcanoes because their eruptive histories were long enough to be considered in a statistical analysis and the events were relatively recent and therefore the dates were reasonably reliable. We also studied other volcanoes from the volcanically active regions around the world. Their eruption sequences were usually not very long so the construction of statistical distributions for interevent times was problematic. To increase statistics by assuming that volcanoes located in the same region and surrounded by similar tectonic settings produce statistically similar eruption sequences [Rodado et al., 2011], we subdivided the Earth into nine volcanically active regions: Alaska (3 volcanoes considered, 72 eruptions), Aleutians (14 volcanoes, 142 eruptions), Central America (22 volcanoes, 403 eruptions), Iceland (7 volcanoes, 100 eruptions), Indonesia (37 volcanoes, 768 eruptions), Japan (21 volcanoes, 502 eruptions), Kamchatka (11 volcanoes, 289 eruptions), New Zealand (4 volcanoes, 175 eruptions), and South America (36 volcanoes, 522 eruptions) (the detailed information for each volcano considered is given in appendix A). We also considered these volcanoes by classifying them into 4 groups according to their type: caldera, complex, shield, and stratovolcano (see Table 4.2). For each of the catalogs considered, when the day of the event was not specified, we assigned it as being the first day of the month. When both the day and the month were missing, we assigned the date to the first of July. This was done following the methodology suggested by Gusev [2008].

The individual volcanoes or groups of volcanoes produce interevent distributions over comparable length scales. In order to model broader time scales of the interevent

time distribution, we compiled an additional group consisting of 24 volcanoes located around the world and characterized by the presence of a caldera and long interevent times between eruptions (see details in the appendix). This was done assuming that the processes controlling the eruptions of this type of volcanoes were similar and therefore their interevent time distributions were comparable. For the major caldera data sets, we did not introduce a date cutoff since the eruptions characterizing these volcanoes were all of considerable size and present in the geological records. We therefore assumed that the eruptive histories were approximately complete.

### 4.3 Results and interpretation

Using the extracted sequences, we computed the probability density functions of interevent times for each of the 26 data sets for the individual volcanoes. Because multiple time scales were involved (days to hundreds of years), we used logarithmically increasing bin lengths to plot the probability densities. We defined  $x_n$  as the coordinate of the right end of the  $n$ th bin ( $n = 0, 1, 2, \dots$ ). The coordinate  $x_{n+1}$  of the  $(n + 1)$ th bin was calculated recursively,  $x_{n+1} = bx_n$ , where  $b$  was the bin factor. The length of the  $n$ th bin was given by  $\Delta x_n = x_0(b^n - b^{n-1})$ . In our analysis the number of bins was chosen for each distribution and the corresponding bin factors  $b$  were estimated. The normalized probability density function was calculated by dividing the number of occurrences within each bin by the corresponding bin length and the total number of data points considered. Figure 4.1 shows the corresponding distributions for the 26 individual volcanoes. They all display a power-law trend for large interevent times and rollover for small times.

To analyze scaling properties of the interevent time distributions, we used the mean interevent time,  $\tau_n$ , between eruptions computed for each data set as a scaling parameter, where  $n$  enumerates each volcano. We then rescaled the individual probability density functions,  $P(\Delta t)$ , according to

$$\tau_n P(\Delta t) = f\left(\frac{\Delta t}{\tau_n}\right), \quad (4.1)$$

where  $f(x)$  is a scaling function. This transformation results in dimensionless coordinate axes. Figure 4.2 shows the resulting plot of the rescaled distributions for the 26 individual volcanoes. We observe a good collapse of the data into one single

Volcano (region)	#eruptions	time span	$\tau_n$ [days]
Ambrym (Vanuatu)	46	1888 – 2008	$976 \pm 160$
Asama (Japan)	110	1595 – 2009	$1386 \pm 247$
Aso (Japan)	129	1434 – 2008	$1637 \pm 232$
Bezymianny (Kamchatka)	53	1955 – 2010	$387 \pm 54$
Colima (Mexico)	51	1519 – 1997	$3495 \pm 709$
Cotopaxi (Ecuador)	58	1532 – 1940	$2612 \pm 1108$
Etna (Italy)	155	1381 – 2010	$1492 \pm 217$
Grimsvotn (Iceland)	44	1610 – 2011	$3405 \pm 403$
Kilauea (Hawaii)	64	1790 – 1983	$1116 \pm 272$
Kirishima (Japan)	55	1524 – 2010	$3285 \pm 613$
Kliuchevskoi (Kamchatka)	99	1697 – 2009	$1163 \pm 156$
Krakatau (Indonesia)	41	1883 – 2010	$1164 \pm 401$
Llaima (Chile)	53	1640 – 2008	$2584 \pm 885$
Marapi (Indonesia)	59	1770 – 2004	$1474 \pm 280$
Mauna Loa (Hawaii)	38	1832 – 1984	$1498 \pm 267$
Merapi (Indonesia)	56	1768 – 2010	$1608 \pm 185$
Piton de la Fournaise (Reunion island)	160	1721 – 2010	$665 \pm 61$
Poas (Costa Rica)	44	1880 – 2009	$1099 \pm 163$
Raung (Indonesia)	55	1815 – 2008	$1302 \pm 217$
Ruapehu (New Zealand)	58	1861 – 2007	$938 \pm 206$
Semeru (Indonesia)	58	1818 – 1967	$954 \pm 202$
Slamet (Indonesia)	41	1772 – 2009	$2161 \pm 528$
Taupo (New Zealand)	25	9460 BC – 260 AD	$147923 \pm 47242$
Tenger (Indonesia)	58	1804 – 2010	$1322 \pm 174$
Tongariro (New Zealand)	68	1839 – 1977	$755 \pm 96$
Villarrica (Chile)	66	1730 – 2009	$1570 \pm 173$

Table 4.1: Summary of the eruption data used for the interevent time analysis of 26 prominent volcanoes.  $\tau_n$  is the mean interevent time between eruptions computed for each volcanic data set. The last column gives the time span of the eruption history considered for each volcano. The errors are given at 95% confidence intervals

Group	#eruptions	#volcanoes
Caldera	448	24
Complex volcano	333	13
Shield volcano	266	12
Strato volcano	2135	113

Table 4.2: Summary of the eruption data used for the interevent time analysis for the volcano types

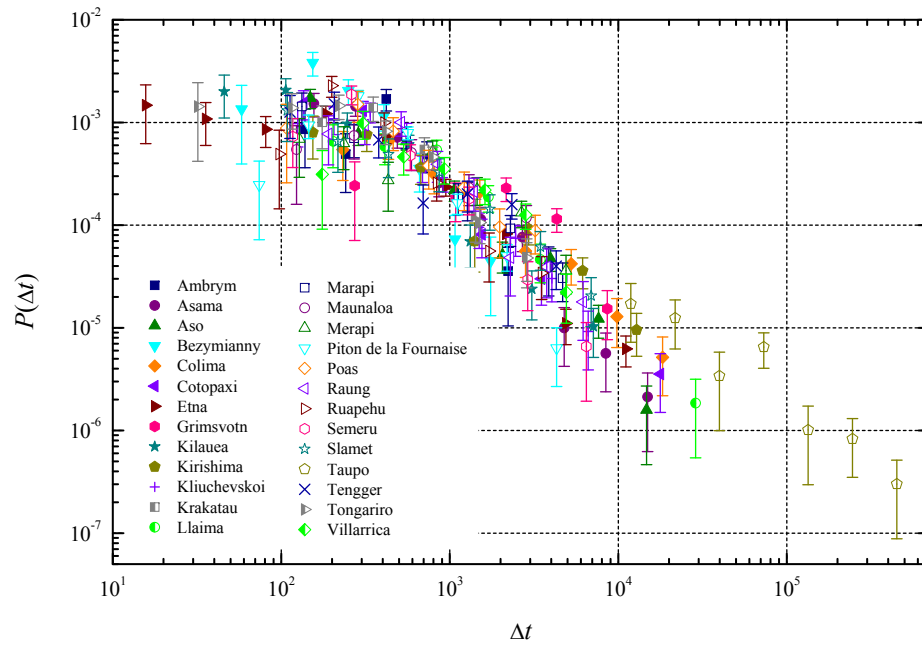


Figure 4.1: Probability density functions of interevent times for the 26 volcanoes on Earth with the largest eruptive history

functional form, similar to the observed scaling reported for the distributions of other natural hazards and rock fractures [Corral, 2003, Corral et al., 2008, Baiesi et al., 2006, Davidsen et al., 2007].

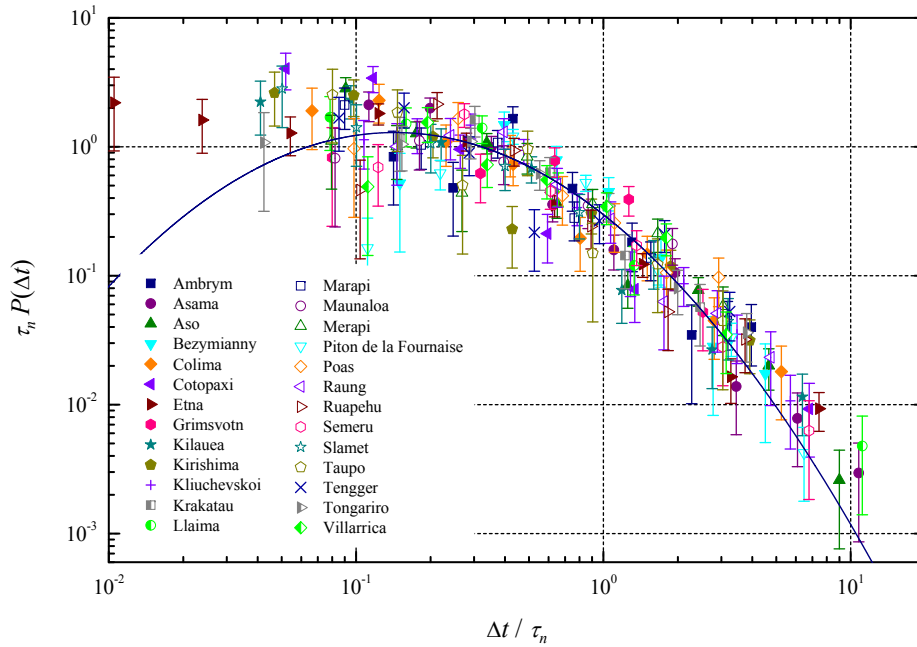


Figure 4.2: Rescaled interevent time distributions for the 26 individual active volcanoes according to Eq. (4.1) with the mean interevent time  $\tau_n$  computed for each volcano (Table 4.1). The solid curve is a fit to the rescaled distributions and is given by the log-normal distribution, Eq. (4.2), with  $\mu = -0.66 \pm 0.05$  and  $\sigma = 1.14 \pm 0.04$ . The errors on the parameters are given at the 95% confidence interval assuming a log-normal distribution. The error bars are not displayed for the sake of clarity

The data sets for grouped volcanoes belonging to specific regions or volcano type typically consist of several volcanoes. Each volcano has its own rate of eruption. For processes with the exponential trend in the distribution of interevent times it is appropriate to rescale first the interevent times of each individual volcano sequence with the corresponding sample mean value and then combine those data sets into a single one [Marzocchi and Zaccarelli, 2006]. This effectively transforms each volcano interevent sequence into one with a unit rate. For each individual volcano eruption sequence belonging to the 9 regional groups and the four volcano type groups, we computed the corresponding interevent times and the sample mean  $\tau_n$ . We then divided each interevent time  $\Delta t_i$ , by this sample mean, in order to normalize each

interevent sequence to have the same unit mean rate. After that we combined these normalized interevent times from all volcanoes belonging to a specific region or group and computed their interevent time distribution functions. This was done to ensure that the distributions were computed from the data having the same rate of occurrence [Marzocchi and Zaccarelli, 2006]. The result of this rescaling is shown in Figure 4.3 and the result for the volcano type subdivision is shown in Figure 4.4. This approach is essentially the same as given by Eq. (4.1).

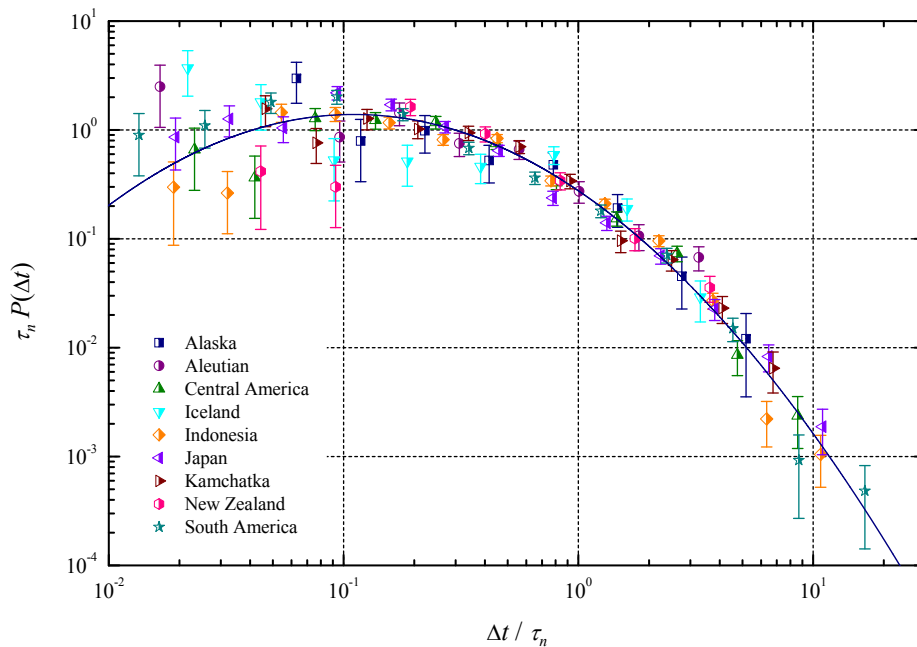


Figure 4.3: The combined rescaled interevent time distributions of groups of volcanoes belonging to 9 different regions. Each individual volcano sequence was first rescaled with the mean interevent time and only after that the distributions were constructed. Data collapse was observed similar to the one shown in Figure 4.2. The solid curve is a fit to the rescaled distributions and is given by the log-normal distribution with  $\mu = -0.70 \pm 0.05$  and  $\sigma = 1.23 \pm 0.03$ . The errors on the parameters are given at the 95% confidence interval assuming a log-normal distribution

We also performed the analysis of interevent times between successive eruptions by introducing the threshold magnitude above which eruptions were considered. This was done to confirm that the proposed scaling was valid for different lower magnitude cutoffs. We used the VEI values as a magnitude because it was the only eruption size scale listed for all volcanoes considered in the catalog. This analysis is useful in estab-



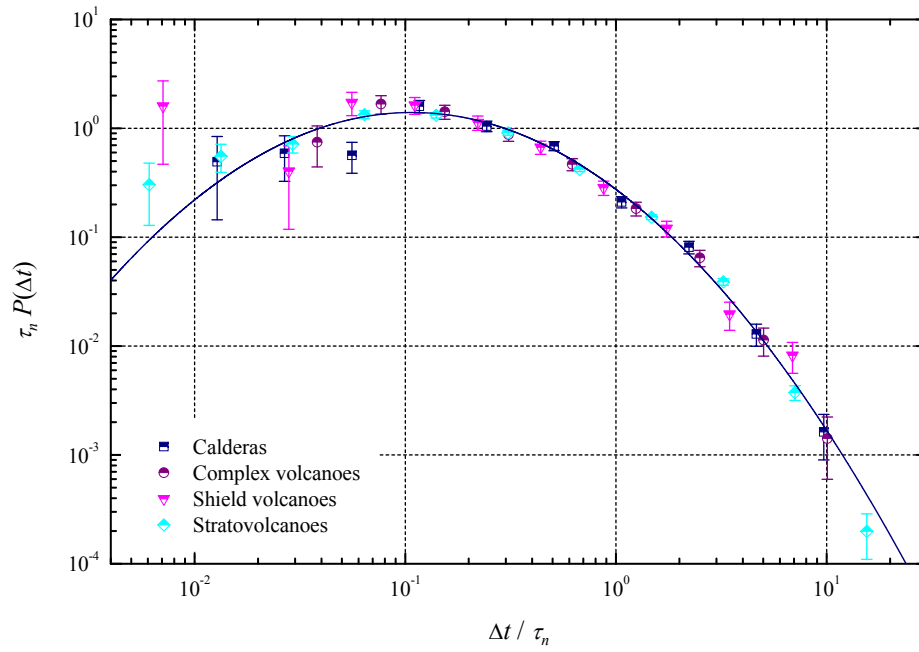


Figure 4.4: The combined rescaled interevent time distributions of volcanoes grouped by type. Each individual volcano sequence was first rescaled with the mean interevent time and only after that the distributions were constructed. Data collapse was observed similar to the one shown in Figure 4.2. The solid curve is a fit to the rescaled distributions and is given by the log-normal distribution with  $\mu = -0.70 \pm 0.04$  and  $\sigma = 1.24 \pm 0.03$ . The errors on the parameters are given at the 95% confidence interval assuming a log-normal distribution

lishing the invariance with respect to the magnitude threshold. This is illustrated in Figure 4.5 for the geographically grouped distributions, where the magnitude cutoffs were 1.0, 2.0, and 3.0, respectively. Comparing these plots with Figure 4.3 confirms the invariance of the rescaled functional form with respect to the magnitude cutoff. The only deviation is observed for VEI  $\geq 3.0$  and can be attributed to the low statistics and resulting spread in the data points. We performed the same analysis for the 26 individual volcano sequences with the similar result that the proposed scaling holds for higher magnitude thresholds (Figure 4.6).

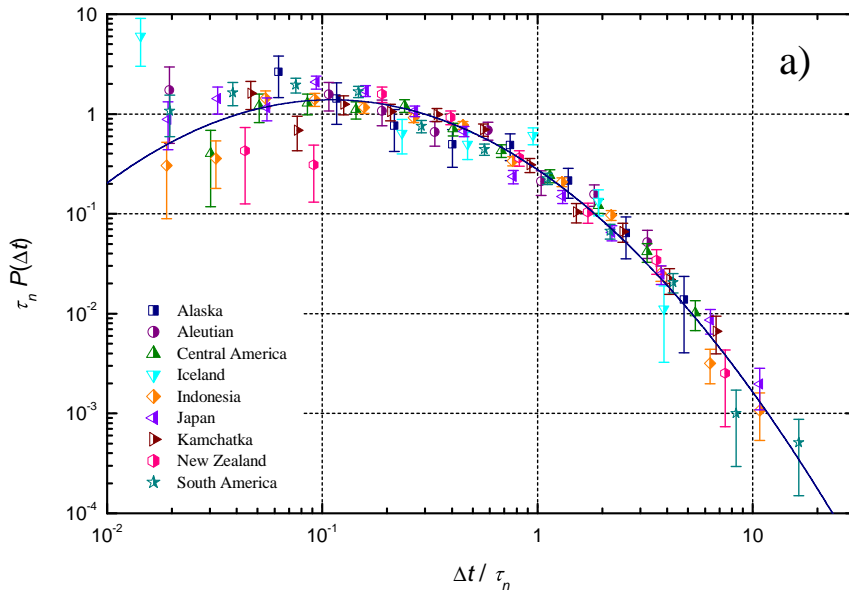


Figure 4.5: The combined rescaled interevent time distributions of groups of volcanoes belonging to different regions. Each individual volcano sequence was first rescaled with the mean interevent time and only after that the distributions were constructed. The lower magnitude cutoff of eruptions was used: a)  $\text{VEI} \geq 1.0$ ; b)  $\text{VEI} \geq 2.0$ ; c)  $\text{VEI} \geq 3.0$ . The solid curve is a fit to the rescaled distributions and is given by the log-normal distribution with a)  $\mu = -0.70 \pm 0.05$  and  $\sigma = 1.23 \pm 0.04$ ; b)  $\mu = -0.67 \pm 0.06$  and  $\sigma = 1.22 \pm 0.04$ ; c)  $\mu = -0.59 \pm 0.15$  and  $\sigma = 1.27 \pm 0.11$ . The errors on the parameters are given at the 95% confidence interval assuming a log-normal distribution. The error bars are not displayed for the sake of clarity

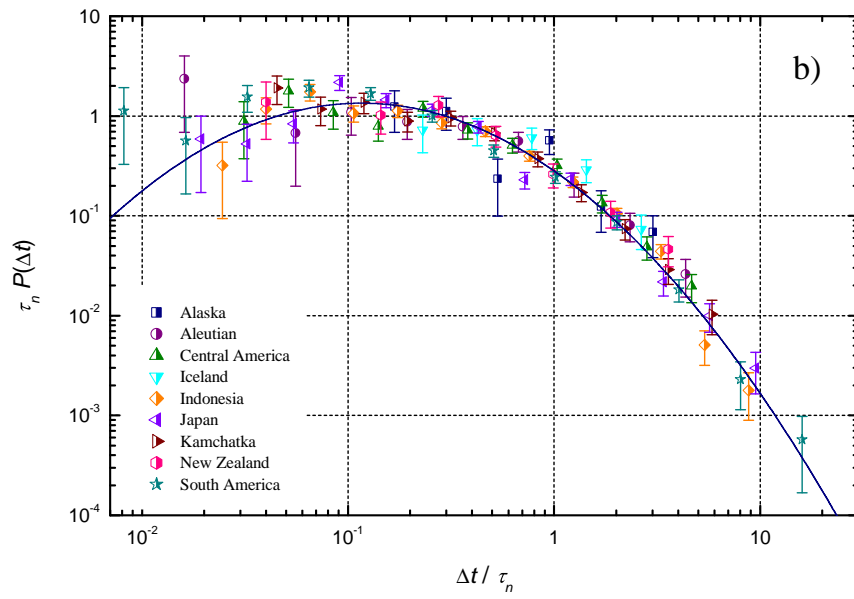


Figure 4.5: Continued.

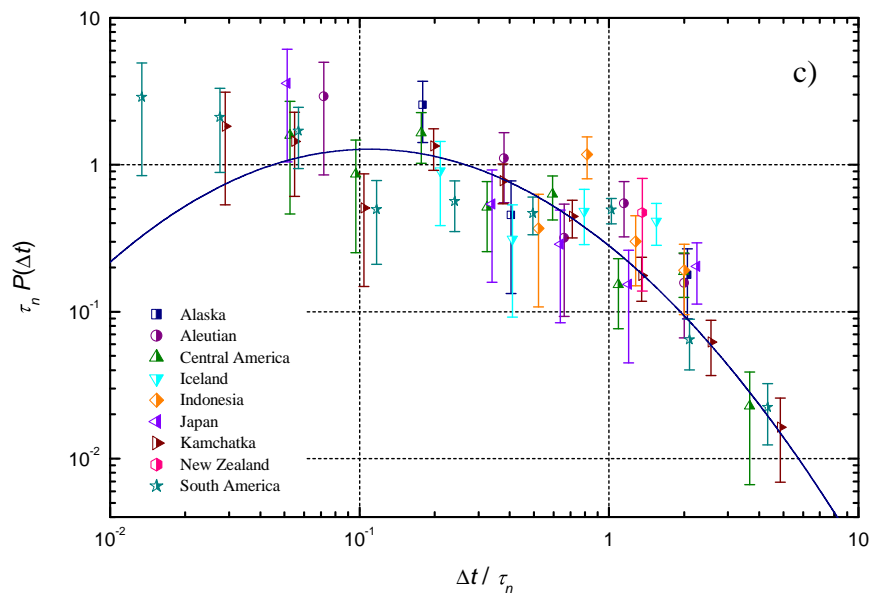


Figure 4.5: Continued.

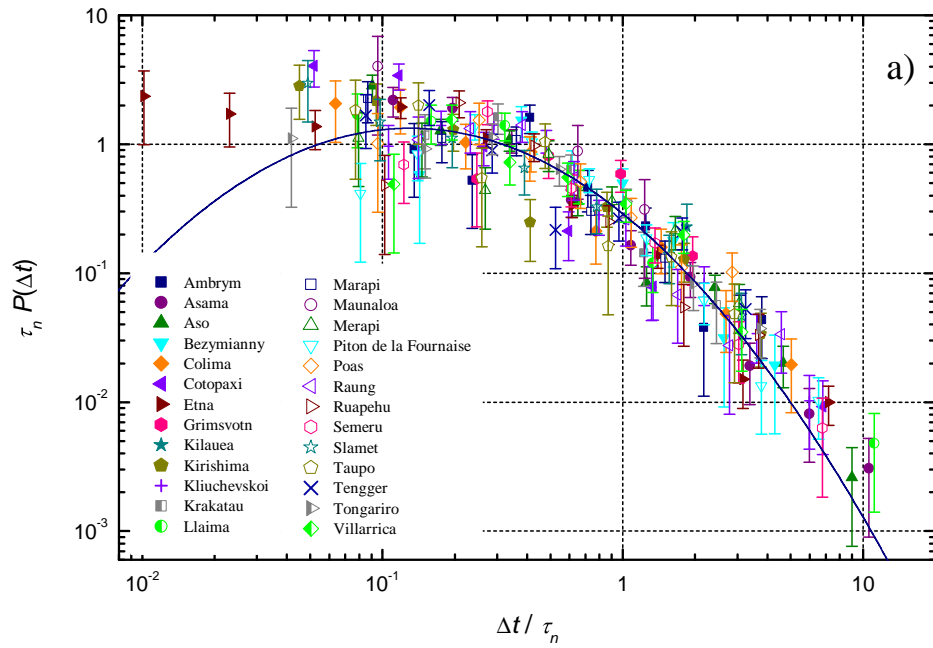


Figure 4.6: Rescaled interevent time distributions for the 26 individual volcanoes according to Eq. (1) with the mean interevent time  $\tau_n$  for each volcano. Lower magnitude cutoffs of eruptions were used: a)  $\text{VEI} \geq 1.0$ ; b)  $\text{VEI} \geq 2.0$ . The solid curve is a fit to the rescaled distributions by the log-normal distribution with a)  $\mu = -0.68 \pm 0.08$  and  $\sigma = 1.20 \pm 0.06$ ; b)  $\mu = -0.68 \pm 0.07$  and  $\sigma = 1.18 \pm 0.06$ .

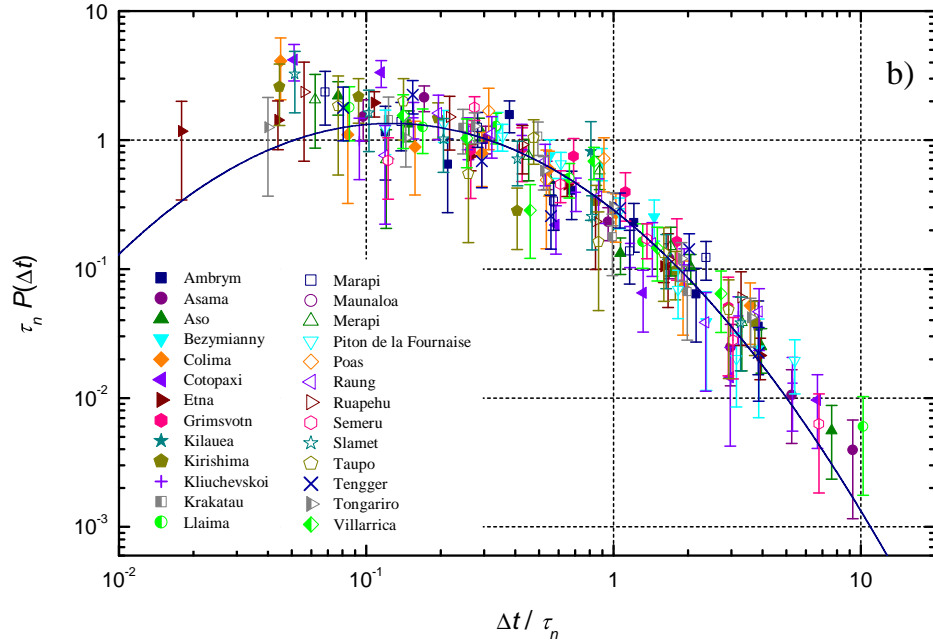


Figure 4.2: Continued.

The above analysis indicates that the mean sample interevent time  $\tau_n$  plays the role of a characteristic time scale for each data set. To model the scaling function  $f(x)$ , we tested several distributions: the generalized Pareto, the log-normal, and the generalized extreme value (GEV) which are used to model heavy tailed distributions, and the gamma and the exponential distributions which are both part of the exponential family and a common choice when fitting interevent time distributions. The estimation of the parameters for these distributions was performed using the maximum likelihood method. In order to select the best among several tested models, we used the Akaike information criterion (AIC) which measures the relative goodness of fit taking into account the number of parameters for each model [Akaike, 1974]. If  $L$  is the maximum value of the likelihood function for a model described by  $k$  different parameters, then  $AIC = -2 \ln L + 2k$ . Smaller values of the AIC indicate a better fit of a model. The results of this test are given in Table 4.3.

The obtained AIC values (Table 4.3) suggested that the log-normal distribution

Distribution	$k$	a) $\ln L$	AIC	b) $\ln L$	AIC	c) $\ln L$	AIC
Log-normal	2	-1527.8	3059.6	-2306.5	4617.0	-2775.2	5554.3
GEV	3	-1544.5	3095.0	-2378.6	4763.2	-2853.6	5713.2
Exponential	1	-1718.0	3438.0	-2497.0	4996.0	-2987.0	5976.0
Gamma	2	-1710.4	3424.8	-2471.8	4947.5	-2955.4	5914.7
Generalized Pareto	2	-1607.2	3218.3	-2366.4	4736.7	-2832.3	5668.5

Table 4.3: The maximum values of the log-likelihood function ( $\ln L$ ) and the corresponding values of the Akaike Information Criterion (AIC) for the model distribution functions considered to fit a) the rescaled distributions given in Fig. (4.2), b) the rescaled distributions given in Fig. (4.3) and c) the rescaled distributions given in Fig. (4.4).  $k$  is the number of parameters for the considered distribution

was the best fit to model the functional form of the rescaled data:

$$f(x) = \frac{1}{x \sigma \sqrt{2\pi}} \exp \left[ -\frac{(\ln(x) - \mu)^2}{2\sigma^2} \right], \quad (4.2)$$

with  $\mu = -0.66 \pm 0.05$  and  $\sigma = 1.14 \pm 0.04$  for the individual distributions (Figure 4.2),  $\mu = -0.70 \pm 0.05$  and  $\sigma = 1.23 \pm 0.03$  for the regional groups of volcanoes (Figure 4.3), and  $\mu = -0.70 \pm 0.04$  and  $\sigma = 1.24 \pm 0.03$  for the volcano type groups (Figure 4.4). These parameter values are equivalent within the error limits, implying a common functional form for all the distributions considered. For short interevent times, we observe a deviation from the proposed scaling behavior. This can be attributed to a different scaling form for short interevent times as observed for earthquakes [Davidsen and Goltz, 2004] or it can be due to low statistics in the event count. To check the latter we also plot the uncertainties in the event counts corresponding to one standard deviation which are based on the binomial distribution. The estimation of the parameters of the log-normal distribution for the proposed scaling model was performed using the maximum likelihood method and the errors are reported at 95% confidence levels. The maximum likelihood method has been chosen as it does not depend on the type of the binning of distribution functions and provides a robust estimate of model parameters. In this method the individual interevent times are used to find an optimal set of parameters based on a specific probability model.

The fit using the exponential distribution exhibits the largest AIC value, indicating that the volcanic eruptions cannot be explained by a Poisson process where

events are independent of each other. Instead, the smallest AIC value for the log-normal fit indicates that the occurrence of volcanic eruptions can be modeled by a random multiplicative process. This distribution has already been reported to describe the conditional probability density function of the times to the next eruption given a magnitude of the current eruption for open conduit systems [Marzocchi and Zaccarelli, 2006]. The eruption sequences we considered, except for the caldera type, were characterized by small mean interevent times and were consistent with an open conduit system. In that regard, our analysis is in agreement with the previous results obtained by Marzocchi and Zaccarelli [2006]. The calderas considered were, on the other hand, described by long mean interevent times, which would be described as a closed conduit system. The result from our scaling analysis states that this type of volcanic system is not characterized by a Poissonian behavior as stated by Marzocchi and Zaccarelli [2006].

## 4.4 Conclusions

The interevent time statistics is an important signature of any underlying stochastic process. Particularly, volcanic eruptions can be considered as a stochastic process in time generated by the complex interaction of the rising magma with surrounding solid rock layers. This process generates events (eruptions) which are characterized in most cases by non-trivial temporal correlations.

Using the proposed scaling analysis, we demonstrated that the distributions of interevent times between eruptions can be described by a universal functional form when rescaled with the corresponding mean interevent times. The observed scaling law indicates that the distributions are controlled by the mean interevent time  $\tau_n$  of each data set. This implies a consistent behavior quite independent of the type of volcanism and geographical setting of volcanoes. In addition, the log-normal distribution plays an important role in describing the temporal distribution of eruptions.

The obtained log-normal scaling can signify that the interevent times between eruptions are the result of a multiplicative process. This also signifies that eruption times are correlated with elements of clustering. Clustering and self-similarity were reported earlier by Gusev et al. [2003]; Gusev [2008]; Marzocchi and Zaccarelli [2006]. The proposed scaling and the log-normal model were derived for relatively short time

---

spans of each volcano sequences. This was done to ensure that the existing records are relatively complete and the average rates of individual volcanic eruptions stayed approximately constant. We also considered sequences of large caldera eruptions to analyze the interevent time distribution for longer time spans. The same analysis was also performed on the eruption sequences with the different lower magnitude (VEI) cutoffs. For all these data sets the obtained rescaled distributions followed a universal functional form described by the log-normal distribution. The obtained universality in the distribution of interevent times is a manifestation of self-similar nature of volcanic processes in time. It also indicates that the temporal structure of volcanic sequences deviates from the simple Poisson statistics. Therefore, the obtained results are important in constraining the physics of eruption processes as well as in any volcanic hazard assessment and mitigation techniques.



## References

- H. Akaike. A new look at the statistical model identification. *IEEE Trans. Autom. Contr.*, 19(6):716–723, 1974.
- J. Åström, PCF Di Stefano, F. Pröbst, L. Stodolsky, J. Timonen, C. Bucci, S. Cooper, C. Cozzini, F. Feilitzsch, H. Kraus, et al. Fracture processes observed with a cryogenic detector. *Phys. Lett. A*, 356(4):262–266, 2006.
- M. Baiesi, M. Paczuski, and A.L. Stella. Intensity threshold and the statistics of the temporal occurrence of solar flares. *Phys. Rev. Lett.*, 96(5):051103, 2006.
- M. S. Bebbington. Trends and clustering in the onsets of volcanic eruptions. *J. Geophys. Res.*, 115(B1):B01203, 2010.
- M. S. Bebbington and C. D. Lai. On nonhomogeneous models for volcanic eruptions. *Math. Geol.*, 28(5):585–600, 1996.
- Á. Corral. Local distributions and rate fluctuations in a unified scaling law for earthquakes. *Phys. Rev. E*, 68(3):035102, 2003. doi: 10.1103/PhysRevE.68.035102.
- Á. Corral, L. Telesca, and R. Lasaponara. Scaling and correlations in the dynamics of forest-fire occurrence. *Phys. Rev. E*, 77(1):016101, 2008.
- Á. Corral, A. Ossó, and J.E. Llebot. Scaling of tropical-cyclone dissipation. *Nat. Phys.*, 6(9):693–696, 2010.
- J. Davidsen and C. Goltz. Are seismic waiting time distributions universal? *Geophys. Res. Lett.*, 31(21):L21612, 2004. doi: 10.1029/2004GL020892.
- J. Davidsen, S. Stanchits, and G. Dresen. Scaling and universality in rock fracture. *Phys. Rev. Lett.*, 98(12):125502, 2007. doi: 10.1103/PhysRevLett.98.125502.
- S. De la Cruz-Reyna. Poisson-distributed patterns of explosive eruptive activity. *Bull. Volcanol.*, 54(1):57–67, 1991. doi: 10.1007/BF00278206.
- N. I. Deligne, S. G. Coles, and R. S. J Sparks. Recurrence rates of large explosive volcanic eruptions. *J. Geophys. Res.*, 115(B6):B06203, 2010.

- J. Dubois and J.L. Cheminee. Fractal analysis of eruptive activity of some basaltic volcanoes. *J. Volcanol. Geotherm. Res.*, 45(3-4):197–208, 1991.
- A. A. Gusev. Temporal structure of the global sequence of volcanic eruptions: Order clustering and intermittent discharge rate. *Phys. Earth Planet. Inter.*, 166(3-4): 203–218, 2008. doi: 10.1016/j.pepi.2008.01.004.
- A. A. Gusev, V.V. Ponomareva, O. A. Braitseva, I. V. Melekestsev, and L. D. Sulerzhitsky. Great explosive eruptions on Kamchatka during the last 10,000 years: Self-similar irregularity of the output of volcanic products. *J. Geophys. Res.*, 108 (B2):2126, 2003. doi: 10.1029/2001JB000312.
- C.H. Ho. Non homogeneous Poisson model for volcanic eruptions. *Math. Geol.*, 23 (2):167–173, 1991.
- F. W. Klein. Patterns of historical eruptions at Hawaiian volcanos. *J. Volcanol. Geotherm. Res.*, 12(1-2):1–35, 1982.
- W. Marzocchi and L. Zaccarelli. A quantitative model for the time-size distribution of eruptions. *J. Geophys. Res.*, 111(B4):B04204, 2006.
- A. T. Mendoza-Rosas and S. De la Cruz-Reyna. A mixture of exponentials distribution for a simple and precise assessment of the volcanic hazard. *Nat. Hazards Earth Syst. Sci.*, 9(2):425–431, 2009.
- C. G. Newhall and S. Self. The volcanic explosivity index (VEI) – An estimate of explosive magnitude for historical volcanism. *J. Geophys. Res.*, 87(C2):1231–1238, 1982.
- D. M. Pyle. Forecasting sizes and repose times of future extreme volcanic events. *Geology*, 26(4):367–370, 1998.
- A. Rodado, M. Bebbington, A. Noble, S. Cronin, and G. Jolly. On selection of analog volcanoes. *Math. Geosci.*, 43(5):1–15, 2011.
- F. Salvi, R. Scandone, and C. Palma. Statistical analysis of the historical activity of Mount Etna, aimed at the evaluation of volcanic hazard. *J. Volcanol. Geotherm. Res.*, 154(3-4):159–168, 2006.

- 
- L. Siebert and T. Simkin. *Volcanoes of the World: An Illustrated Catalog of Holocene Volcanoes and their Eruptions*. Smithsonian Institution, Global Volcanism Program Digital Information Series, GVP-3, 2002-. <http://www.volcano.si.edu/world/>.
- T. Simkin. Terrestrial volcanism in space and time. *Annu. Rev. Earth Planet. Sci.*, 21:427–452, 1993.
- D. L. Turcotte. *Fractals and Chaos in Geology and Geophysics*. Cambridge Univ. Press, Cambridge, 2nd edition, 1997.
- F. E. Wickman. Repose period patterns of volcanoes. I. Volcanic eruptions regarded as random phenomena. *Ark. Kem. Mineral. Geol.*, 4(4):291, 1966.

# Chapter 5 A Cellular Automata to Model Magma-Crust Interactions and Volcanic Eruptions

## 5.1 Introduction

Volcanic eruptions are the expression of complex interactions between magma and the host rock. They can display a variety of behaviors, ranging from gentle effusive activity to highly explosive events. Volcanic processes have been extensively studied through field work and numerical analysis providing us with some quantitative understanding of the main physical mechanisms involved. However, our current knowledge remains insufficient to explain and forecast the temporal behavior of eruptions. The deterministic character of the modeling fails at reproducing the temporal patterns observed. Therefore, understanding the nonlinear interactions that lead to eruptions alongside with being able to reproduce the observed temporal patterns are crucial steps in the field of volcanology and hazard assessment.

Statistical analysis of the spatial, temporal and size distribution of volcanic eruptions has allowed to uncover some of the behavior of these characteristics. The size distribution of volcanic eruptions has been shown to display scale-invariant behavior [Newhall and Self, 1982, De la Cruz-Reyna, 1991, Simkin, 1993, Gusev et al., 2003], implying that there exist no characteristic eruption size for a given region. The spatial distribution of basaltic flows seems to exhibit self-similarity [Pelletier, 1999] and the distribution of magma fractions at depth was found to display self-similar clustering [Shaw and Chouet, 1991]. The size and temporal distribution of acoustic emissions from volcanic rocks are also characterized by power-law distributions, implying a single underlying mechanism [Diodati et al., 1991, 2000]. The temporal patterns describing volcanic events are complex and are the results of non-trivial correlations. Studying the temporal organization of global volcanic activity, Gusev [2008] observed self-similar clustering of eruptions. These characteristics of worldwide activity lead to the conclusion that a common mechanism was responsible for

the time/size clustering. The scaling properties of the temporal behavior of eruptions displayed by multiple volcanic regions and by the most currently active volcanoes on Earth also hints towards a universal mechanism for the triggering of events [Sanchez and Shcherbakov, 2012]. Other natural hazards such as earthquakes, landslides, forest fires or tropical cyclones have also been shown to display power law distributions in size [Kagan, 2002, Malamud et al., 2004, 2005, Corral et al., 2010]. This kind of statistical behavior implies the presence of complex behavior, where a broad range of events are triggered by small driving processes such as tectonic forcing, and the relationship between input and output is highly non-linear [Deluca and Corral, 2013]. Such statistical observations are hard to quantify using classical mechanical laws and an alternative approach is therefore needed [Lahaie and Grasso, 1998].

The non-linear interactions of several entities in a complex system lead to a global behavior that cannot simply be described by the sum of each entity's local behavior. This kind of systems are highly sensitive to initial conditions and the emerging temporal patterns are not predictable or deterministic [Schadschneider et al., 2009]. The analysis and modeling of cellular automata (we will call them CA from now) is one of the approaches used to study complex systems. CAs are an idealization of a physical system where the physical characteristics of a physical system are represented by only a set of values. The dynamics of physical systems are often described using nonlinear partial differential equations. Due to non-linearities, the solutions of these equations are strongly sensitive to the initial conditions. The same type of complications can occur in discrete dynamical systems such as CAs [Chopard and Droz, 1998]. A CA is represented by a lattice (can be one, two-dimensional or more) filled with cells. The state of each cell at a given time step is updated according to local rules that depend on the state of the neighboring cells. Following the predefined rules, the CA can produce a variety of behaviors including complex ones. CAs therefore represent a good alternative to explore the dynamics of continuous systems and to simulate natural processes. These kind of models have been successful in the past at reproducing the complex behavior of some natural hazards such as earthquakes [Ogata, 1992, Olami et al., 1992], forest fires [Bak et al., 1990] and processes such as percolation [Sahimi, 1993].

The use of CAs in the field of volcanology is a new approach and has been mainly applied to model the flow of erupted lava in order to improve the determination of hazardous zones on specific volcanoes [Vicari et al., 2007, Crisci et al., 2003, Del Negro

et al., 2008]. Lahaie and Grasso [1998] developed a CA composed of fluid and rock cells interacting with each other in order to reproduce the size and temporal behavior of the eruptive activity at the Piton de la Fournaise volcano. They were able to show that the behavior of the volcano could be explained by a combination of multiple magma storages rather than a main magma chamber. Pelletier [1999] combined a model of fluid migration in a disordered porous media developed by Buldyrev et al. [1992] with eruption dynamics. His goal was to describe magmatic upwelling through the continental crust. When analyzing the synthetic history of volcanism produced by this model, it was found that the spatial and temporal pair-correlation functions were consistent with the functions obtained from real data.

Piegari et al. [2008] designed a CA that models magma ascent through the crust. In a two-dimensional lattice, the initial stress level of each site is assigned randomly while a slow constant loading is applied to each site following the rule of the model developed by Olami et al. [1992]. Fractures are initiated and magma is allowed to rise in an upward direction when in contact with a crack. An eruption occurs when a batch of magma reaches the surface (top of the lattice) and the volume  $V$  of the eruption is defined by the number of magma filled sites connected to the surface. It was found that the size distribution of eruptions exhibits a power-law behavior consistent with the behavior observed in nature by using the Volcanic Explosivity Index (VEI) scale for eruptions [Newhall and Self, 1982, Simkin, 1993]. Concerning the interevent time distribution  $P(t)$ , the model results exhibit an exponential behavior for large eruptions, implying that the major events are independent and occur at a constant rate, while small events are better fitted by a stretched exponential distribution. Expanding this model Piegari et al. [2011] incorporated the effect of the water content of the magma and investigated the effect of water exsolution on the explosivity degree of eruptions. In another formulation of the model, Piegari et al. [2013] introduced a rock density layered structure in order to approximate the density structure of mount Vesuvius. The density differences between the magma and the host rock determined whether or not the magma was allowed to rise, or had to stop and start cooling and solidifying. The interevent time distributions produced by the model is in agreement with the data from Vesuvius.

In this chapter, we formulate a CA model that investigates the magma-crust interactions in order to further our understanding of the several volcanic temporal regimes in open and closed conduit systems. We focus on using a minimal number

of parameters in order to investigate universality in eruption processes. We compare the results of the CA with temporal data obtained from worldwide catalogs [Siebert and Simkin, 2002-].

## 5.2 The Model

Our goal is to reproduce the statistical properties of volcanic eruptions using a simple physically motivated model. We are interested in the size and temporal behavior of events in a large range of tectonic settings. To achieve this goal, we formulate a model that describes the magma-crust interactions in volcanic settings. We base our model on the consensus that overpressure in the reservoir leads to the rise of magma through a network of cracks to the surface, and the hypothesis that magma ascent is mainly controlled by buoyancy differences [Ryan, 1987].

As previously stated, CAs represent a powerful tool to model complex behaviors. One class of CAs has been specifically developed and used to simulate fluid flow behavior. Based on the discretization of partial differential equations, the Lattice Gas Cellular Automata (LGCA) had been used as a tool to simulate fluid flow. The first model, formulated by Hardy et al. [1973] and now referred to as the HPP model, describes particle interactions on a 2-dimensional square lattice which consist in a series of collision and propagation stages where particle number and momentum are conserved. Using the same evolution rules on a hexagonal lattice, Frisch et al. [1986] showed that this type of model is successful at solving the Navier-Stokes equations of fluid flow as the change of geometry from the HPP model introduced isotropy in the system. For this study, we will expand the HPP model in order to represent the interactions between magma and the solid crust in a volcanic setting.

We consider a rectangular lattice composed of nodes that can contain a maximum of 4 particles at a time, one particle on each branch of the node (see Figure 5.1). The state of each site  $(i, j)$  of the lattice at time  $t$  is characterized by its strength  $s(i, j, t)$  and by the presence or not of magma at each branch of the node  $m_d(i, j, t)$  where  $d = (n, e, s, w)$  is the branch position on the node:

$$0 \leq s_{crust}(i, j, t) \leq 1, \tag{5.1}$$

$$s_{chamber}(i, j, t) = 0, \quad (5.2)$$

$$m_d(i, j, t) = \begin{cases} 1 \\ 0 \end{cases}, \quad (5.3)$$

The system is divided into two distinct areas, the magma chamber and the crust (see Figure 5.1 e)). The strength of the sites in the crust  $s_{crust}(i, j)$  can range from 0 for a completely "open" site to 1 for a completely "closed" site (see Eq. (5.1)). The strength of the sites in the magma chamber is set at a constant value of 0, so all sites in this area are "open" (see Eq. (5.2)). A closed site, characterized by  $s(i, j) < 1$ , will prevent the propagation of magma particles while an open site, where  $s(i, j) = 0$ , will allow an undisturbed movement of the particles. At each time increment  $\Delta t$ , the system is updated in 3 steps. First, we input particles in order to simulate a magma feeding rate. Each empty site at the bottom of the chamber has a probability  $P_f$  to be filled by a particle with an upward motion. In the second step, collisions between particles are updated. The only configuration of particles affected by this stage is the case where only two particles are present and in an opposite position on a horizontal or a vertical plane (see configurations c) and d) of Figure 5.1). Once all the collisions have been updated, the third step consists in the propagation of the particles. In the simple case where  $s(i, j, t) = 0$ , the particles are free to move to the next site (see Figure 5.2). This process occurs at all times in the magma chamber. In the crust, when  $s_{crust}(i, j, t) \neq 0$ , the particles are not allowed to propagate and will bounce back and be guided in the opposite direction. A particle headed upwards in the crust encountering a locked site will end up heading downwards for example. In order to create a pathway to the surface, the particles will progressively damage the sites in the crust. Each particle is indeed assigned a constant "damage capacity"  $0 < d < 1$ , while the crustal sites are assigned a constant "healing capacity" value  $0 < h < 1$ .

$$s_{crust}(i, j, t + 1) = s_{crust}(i, j, t) - d \quad (5.4)$$

$$s_{crust}(i, j, t + 1) = s_{crust}(i, j, t) + h \quad (5.5)$$

Every time a site is hit by a particle, its strength will be affected according to Eq. (5.4). When not hit by any particles, crustal sites will "heal" according to



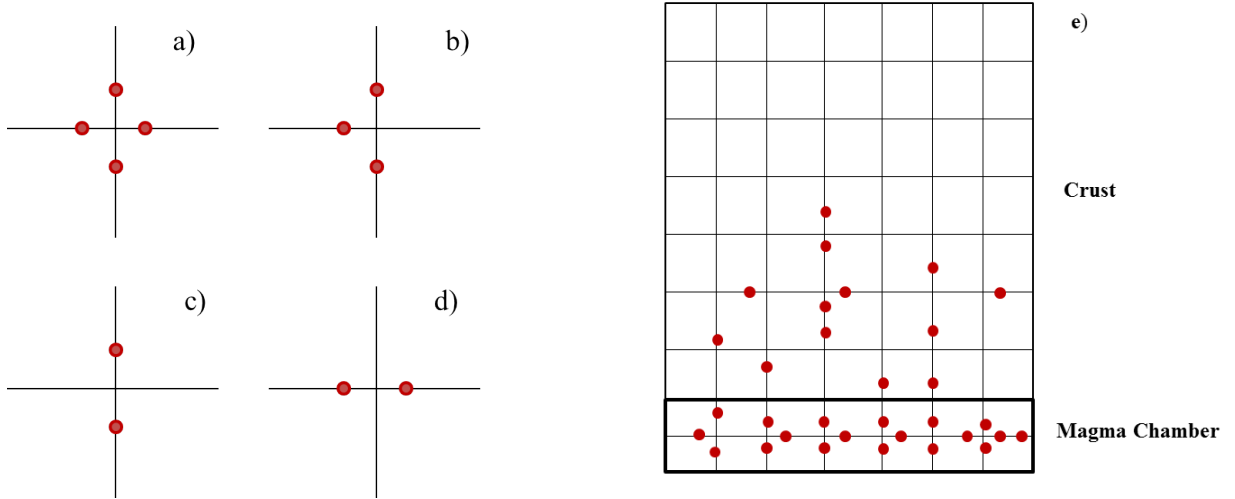


Figure 5.1: Different possible configurations for particle positions in the HPP model for the cases of 4, 3 and 2 particles on a node (a,b,c,d). Schematic view of the 2D lattice with the distinction between the magma chamber and the crust (e)

Eq. (5.5). This characteristic of the model is one of the main difference with the CAs formulated by Piegari et al. [2008, 2011, 2013]. In our case, we consider that density differences cause the ascent of magma through the crust and that this ascent is the primary force that generates fractures within the crust. Slow constant tectonic loading is ignored in our case.

When a particle reaches the top of the crust and  $s_{crust}(i, top, t) = 0$ , an eruption occurs. In order to evaluate the size of the eruption (or the number of particles involved), we compute the number of open sites connected to the eruption site and containing magma particles. To do so, we use the rules defined in the forest fire model [Bak et al., 1990]. In our model, we introduce a connectivity factor  $C$  which controls whether or not the open site is considered as part of the eruption cluster.  $C$  is the probability of the open site to be considered part of the eruption. We then define the eruption size as the number of magma particles present in the defined cluster. These particles will exit the system at time  $t$ .

With these rules, we want to represent a wide range of volcanic behaviors by only changing the values of main two parameters:  $d$  and  $h$ . In this model, these two

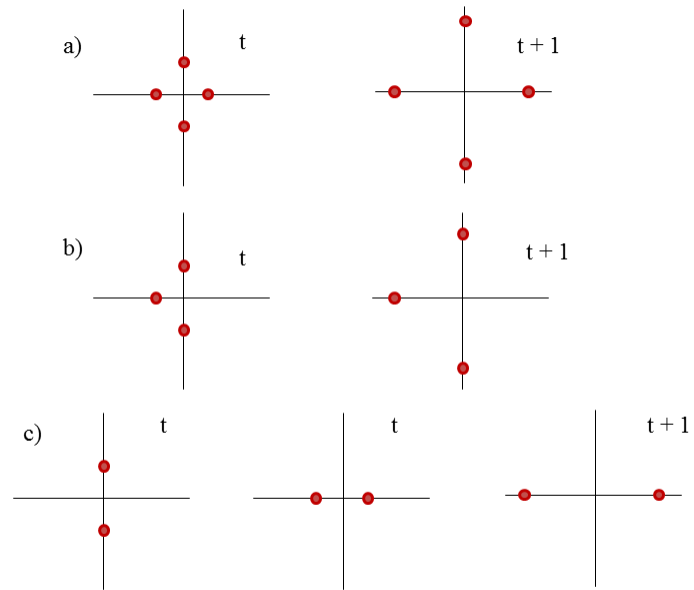


Figure 5.2: Collision and propagation rules for the different configuration of particles on the lattice

parameters are not the only ones responsible for the complex interactions occurring in the crust, but rather the ratio  $d/h$  can be considered as a proxy to characterize the global state of the crust and magma body. These two parameters comprise the different variables defining the strength of the crust alongside with the pressure changes in the magma body. We want to investigate open and closed conduit systems using the same model and therefore demonstrate the universality of the processes responsible for all types of volcanic eruptions.

### 5.3 Results

For numerical simulations of the model, we studied the behavior of two different configurations. The first one (we will call it model 1) is defined on a 2-dimensional square lattice of size  $300 \times 110$ . The crustal dimensions are  $300 \times 100$  and the magma reservoir at the bottom of the system has a size of  $300 \times 10$ . The particles are propagating in the  $[N, S, E, W]$  directions as shown in Figure 5.3. Model 2 is also defined on a 2-dimensional square lattice but has a size of  $256 \times 256$ . The crust fills 80% of the system and the magma chamber fills the remaining 20%. The particles in this case are propagating in the  $[NE, NW, SE, SW]$  directions (see Figure 5.3).



Figure 5.3: Propagation directions for model 1 (left) and model 2 (right).

For both configurations, at time  $t = 0$ , the whole crust is "locked" and empty and the magma chamber contains a random number of particles (each position on a node has a probability of 80% to be filled with a particle at  $t = 0$ ). We consider reflective boundary conditions so the particles bounce back on the sides and bottom of the system, and the sites at the boundaries can only contain a maximum of 3 particles. After the system has reached a steady state (the number of particles in the system is oscillating around a constant value), we collect the size of each eruption in order to compute statistics on the frequency-size distribution of events as well as the

time of occurrence of events to obtain statistics on the temporal behavior of eruptions in the two systems.

### 5.3.1 Model 1 ( $300 \times 110$ )

We studied a range of values for  $d$  and  $h$  ( $0.04 < d < 0.95$  and  $0.03 < h < 0.90$ ) in order to simulate different volcanic settings. We investigated several connectivity values ( $C = 0.4; 0.5; 0.6$ ) but we will focus our analysis on the results of  $C = 0.5$ . For  $C = 0.4$ , we obtain a very small amount of eruptions and our statistics are therefore low. For  $C = 0.6$ , the number of particles involved in an eruption is much greater, creating almost constant eruptions and leading to low statistics as well.

#### 5.3.1.1 Frequency size distribution of eruptions

An eruption event consists in the undisrupted succession of magma loss from the system. When particles have reached the top of the system and the strength of the top of the crust  $s_{crust}(i, top, t) = 0$ , particles start exiting the system according to the eruption process previously described. If eruptions occur within consecutive time steps, they are counted as a single eruption and its size consists in the sum of exiting particles at each time step. An eruption event can last for one or many more time steps. We collected eruption data for different values of  $d$  and  $h$  and computed the probability density distributions  $P(V)$  (normalized histogram, or PDF) for all of them.

We observe a consistent power-law behavior for the frequency-size distributions of events with the appearance of a peak for large eruptions. The peak being located at a size of  $3 \times 10^4$  and the size of the system being  $3 \times 100 = 30,000$ , we conclude it corresponds to the maximum size of an event (see Figure 5.4). To show that this peak is indeed related to the size of the system, we investigated the effect of a change in the system thickness on  $P(V)$  (see Figure 5.6). We observe a shift of the peak to larger values when the thickness of the system increases.

We fit the distribution by a truncated power-law model using a maximum likelihood estimation, following the fitting method by Deluca and Corral [2013] (see

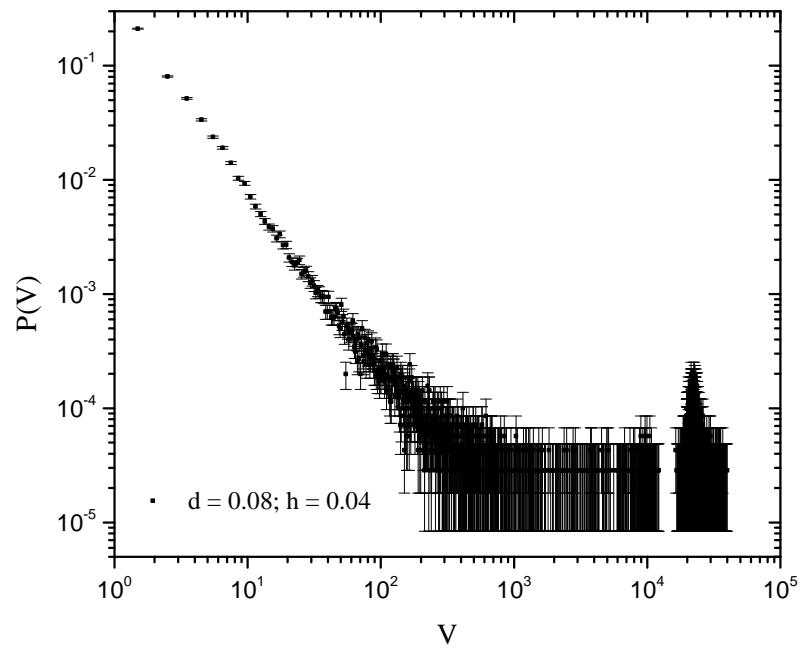


Figure 5.4: Example of the frequency-size distribution of eruptions for  $d = 0.08$  and  $h = 0.04$ . We note the peak at  $3 \times 10^4$

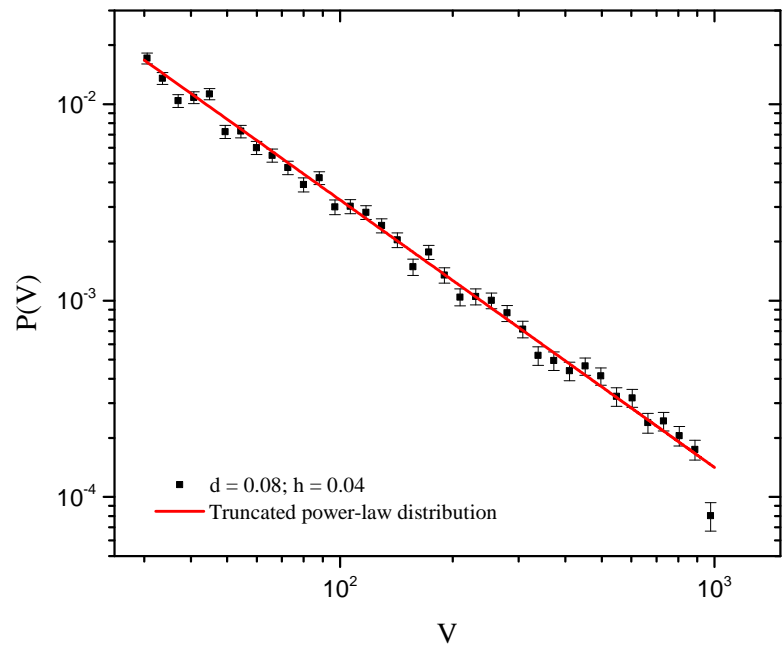


Figure 5.5: Truncated power-law fit of the frequency-size distribution for the size range  $V \in [30, 1000]$  with  $\alpha = 1.36 \pm 0.03$ .

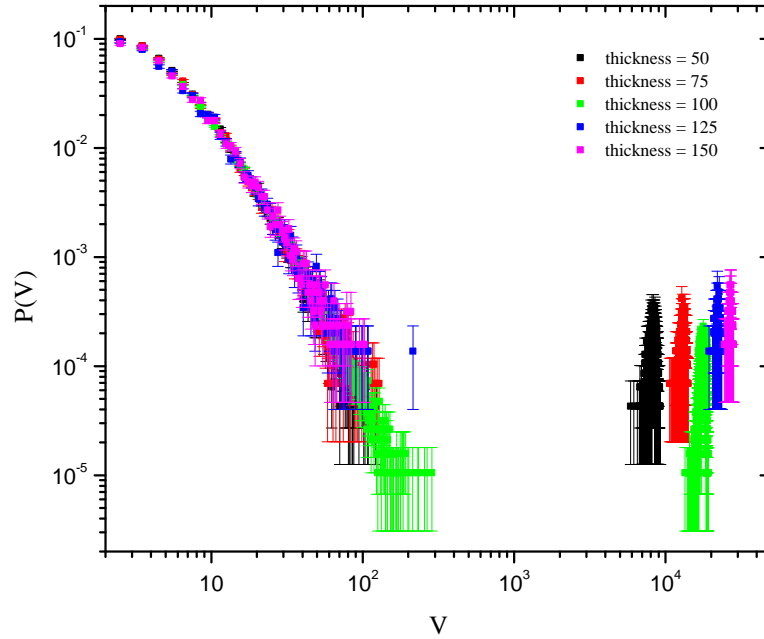


Figure 5.6: Frequency-size distributions of eruptions for  $d = 0.5$  and  $h = 0.2$  and varying thickness of the system.

Figure 5.5). The probability density of the power-law distribution is defined over the range  $a \leq x \leq b$  and is given by:

$$P(x) = \frac{\alpha - 1}{a^{1-\alpha} - b^{1-\alpha}} \left(\frac{1}{x}\right)^\alpha \quad (5.6)$$

where  $\alpha$  is the power-law exponent. When  $b \rightarrow \infty$ ,  $\alpha \geq 1$  and  $a > 0$ , Eq. (5.6) describes the left-truncated power-law distribution. When  $b$  takes a finite value, Eq. (5.6) provides a doubly truncated power-law distribution [Deluca and Corral, 2013]. Here, we use a doubly truncated power-law model to fit our data since the finite size effect of the system prevents  $b$  to tend to infinity.

After fitting the frequency-size distributions, we observe that the power-law exponent  $\alpha$  varies with the values of  $d$  and  $h$  and ranges from 1.3 to 4.5. We observe a consistent increase in the value of  $\alpha$  when  $h$  increases for small values of  $d$  (see Figure 5.7). For larger values of  $d$  ( $0.2 < d < 0.9$ ),  $\alpha$  seems to stay constant when  $h$  increases for a given  $d$  (within the errors limits, see Figure 5.8). In that case, when  $d$  increases,  $\alpha$  seems to increase as well. Figure 5.9 shows the size distributions for large values of  $d$  and a constant  $h$ . This result implies that the effect of a change in  $h$

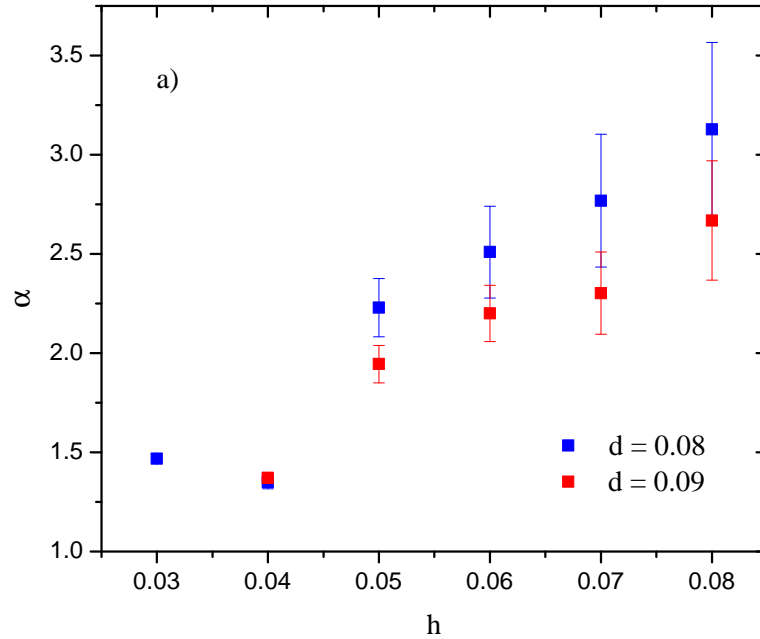


Figure 5.7: Variation of the power-law exponent  $\alpha$  with  $h$  for small values of  $d$ .

affects the potential eruptions sizes more efficiently for smaller than for larger values of  $d$ .

Model 1 is successful at reproducing the power-law behavior of volcanic eruption sizes observed in nature [Newhall and Self, 1982, Simkin, 1993, Diodati et al., 2000]. The exponent change according to the model parameters may reproduce a change in the power-law exponent of the size distribution of events from one volcano to another. The frequency-size distribution of events at the Piton de la Fournaise volcano was shown to display a power-law behavior with an exponent around  $\alpha = 1.2$  [Lahaie and Grasso, 1998], which is consistent with values found in our model for small values of  $d$  and  $h$  (within the error limits). We also observe the appearance of a characteristic behavior of eruptions, with small events following a power-law distribution while events of the size of the system have a relative high probability of occurrence.

### 5.3.1.2 Temporal behavior

We define the interevent time as the time from the onset of one eruption to the other and ignore the duration of an event [Klein, 1982, Sanchez and Shcherbakov, 2012]. We collected the interevent times of eruptions for varying values of  $d$  and  $h$  and computed their probability density functions  $P(\tau)$ .

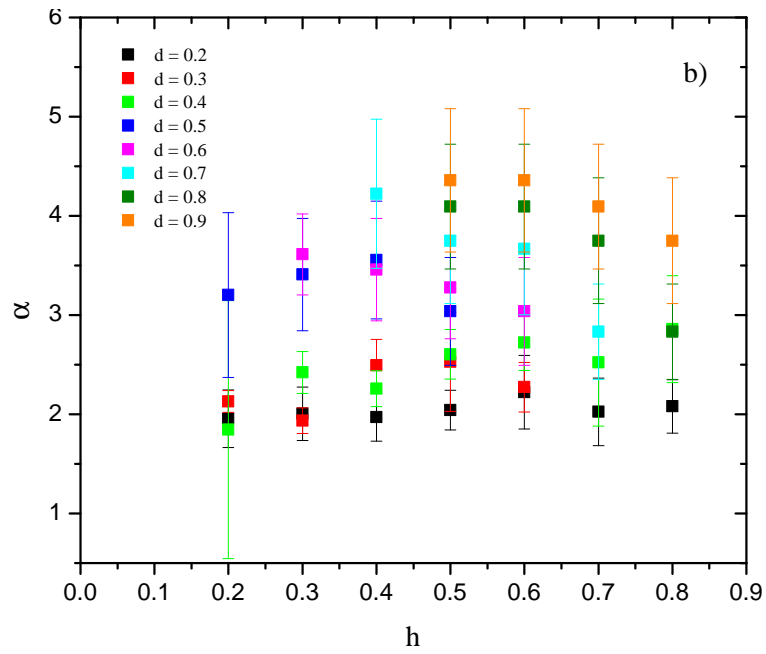


Figure 5.8: Variation of the power-law exponent  $\alpha$  with  $h$  for large values of  $d$  (b).

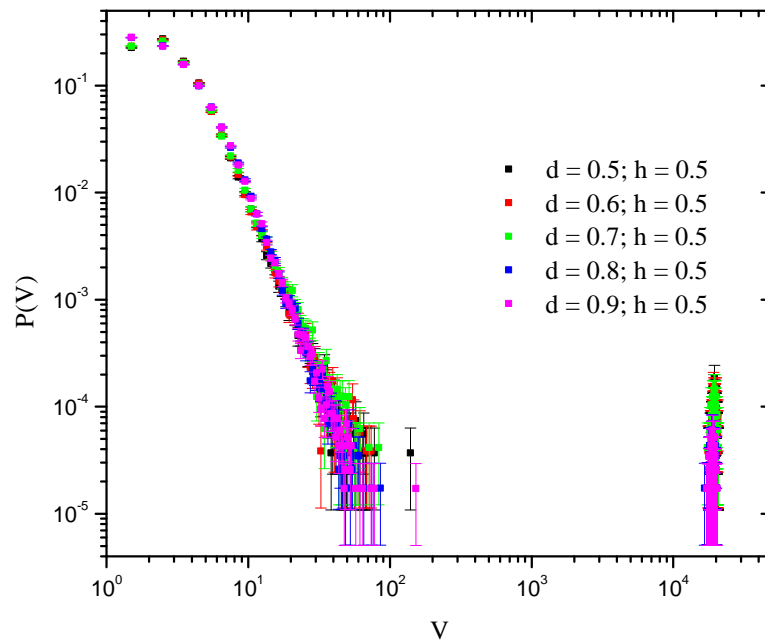


Figure 5.9: Frequency size distributions of eruptions for  $h = 0.5$  and large values of  $d$ .



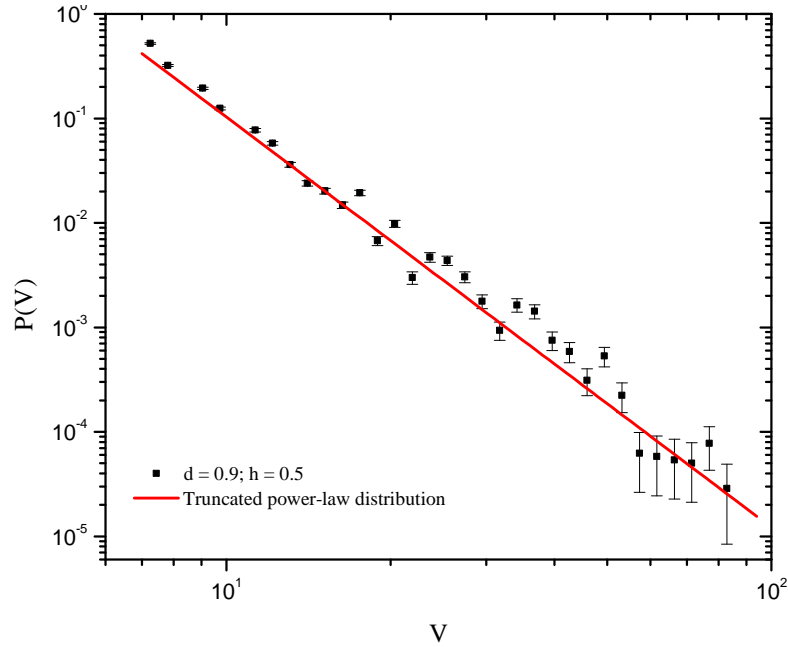


Figure 5.10: Truncated power-law fit of the frequency-size distribution for  $d = 0.9$  and  $h = 0.5$  for the size range  $V \in [7, 100]$  with  $\alpha = 4.36 \pm 0.72$ .

Unlike the distribution of eruption sizes, we observe several temporal regimes according to the values of  $d$  and  $h$ . In order to describe these different regimes, we tested several models. First, the truncated exponential distribution (Eq. (5.7)) [Hannon and Dahiya, 1999]

$$P(x) = \frac{\lambda e^{-\lambda x}}{e^{-a\lambda} - e^{-b\lambda}} \quad (5.7)$$

where  $\lambda$  is the event rate and the distribution is defined for  $a < x \leq b$ . The second distribution tested was the truncated log-normal distribution (Eq. (5.8)) [Cohen, 1988]:

$$P(x) = \frac{1}{\sigma\sqrt{2\pi}(x-a)} \exp\left\{-\frac{1}{2\sigma^2} [\ln(x-a) - \mu]^2\right\} \quad (5.8)$$

where  $\sigma$  is the shape parameter,  $\mu$  is the scale parameter and  $a < x < \infty$ . The last model tested was the truncated power-law distribution (Eq. 5.6).

We fitted our temporal data using the maximum likelihood method for each of the considered distributions. In order to find the best fitting model, we first tested the

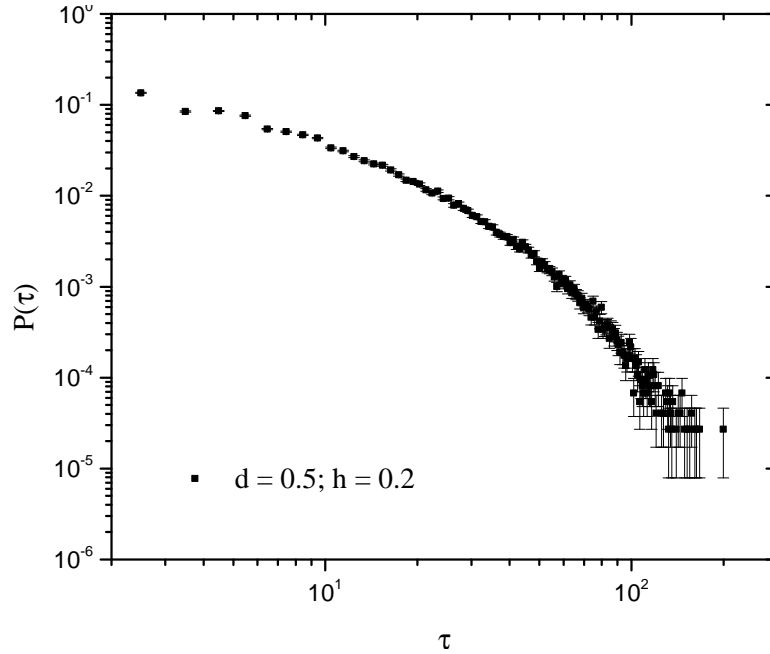


Figure 5.11: Example of the log-normal regime for the distribution of eruptions interevent times for  $d = 0.5$  and  $h = 0.2$ .

null hypothesis that the data is drawn from each distribution using the Kolmogorov-Smirnov test (KS test) [Massey and Frank, 1951]. In our case, we considered that if  $p \geq 0.01$  ( $p$  is the statistical p-value from the KS test), we could not reject the null hypothesis. If more than one model passed the KS test, we used the Akaike Information Criterion (AIC) which measures the relative goodness of fit taking into account the number of parameters for each model [Akaike, 1974]. If  $L$  is the maximum value of the likelihood function for a model described by  $k$  different parameters, then  $AIC = -2 \ln L + 2k$ . Smaller values of the AIC indicate a better fit of a model.

We observed three regimes with varying  $d$  and  $h$  that can be described by the following distributions:

- truncated log-normal (see Figures 5.11 and 5.12),
- truncated exponential (see Figure 5.13 and 5.14),
- truncated power-law (see Figure 5.15 and 5.16).

We explored the parameter space of the model with different values of  $d$  and  $h$  in order to uncover some consistent behavior from those three regimes. The phase

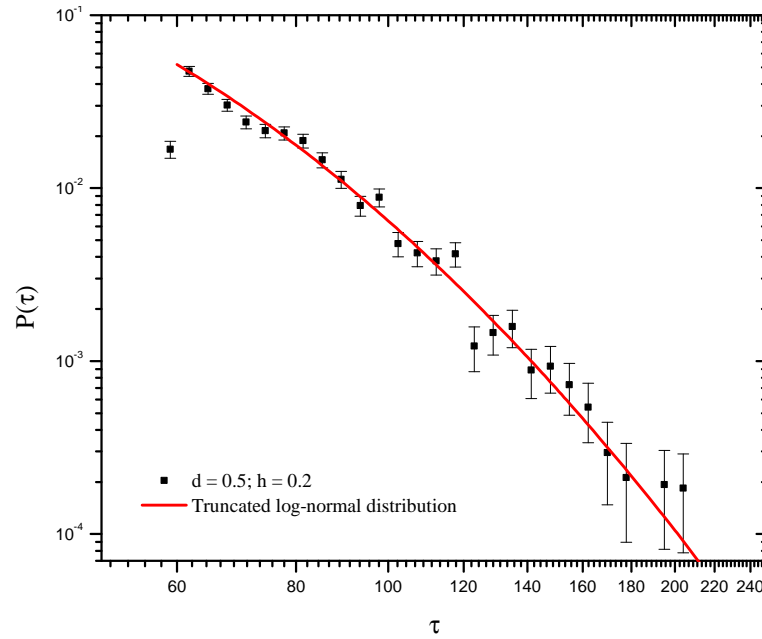


Figure 5.12: Truncated log-normal fit of the distribution for the time range  $\tau \in [60, 300]$  with  $\mu = 3.48 \pm 0.61$  and  $\sigma = 0.54 \pm 0.14$

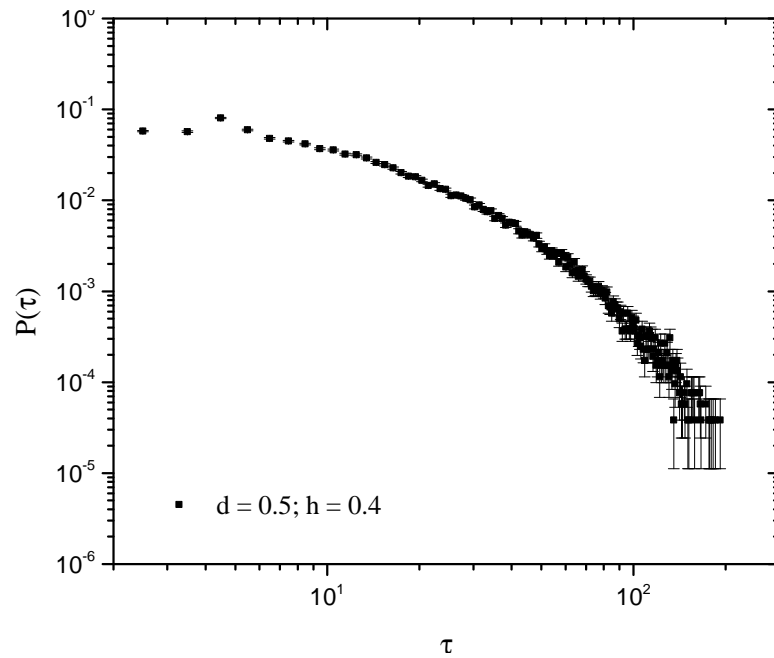


Figure 5.13: Example of the exponential regime for the distribution of eruptions interevent times for  $d = 0.5$  and  $h = 0.4$ .

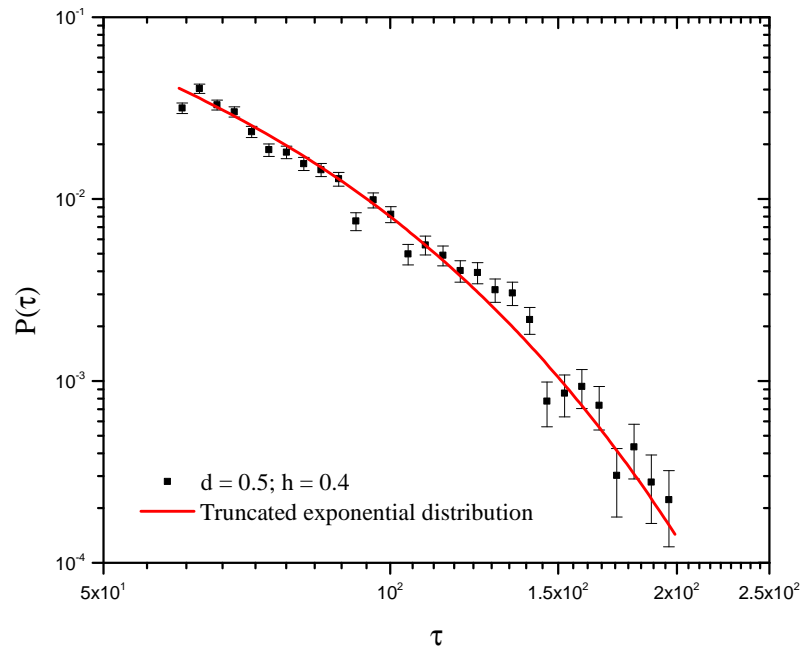


Figure 5.14: Truncated exponential fit of the distribution for the time range  $\tau \in [50, 200]$  with  $\lambda = 26.27 \pm 2.11$ .

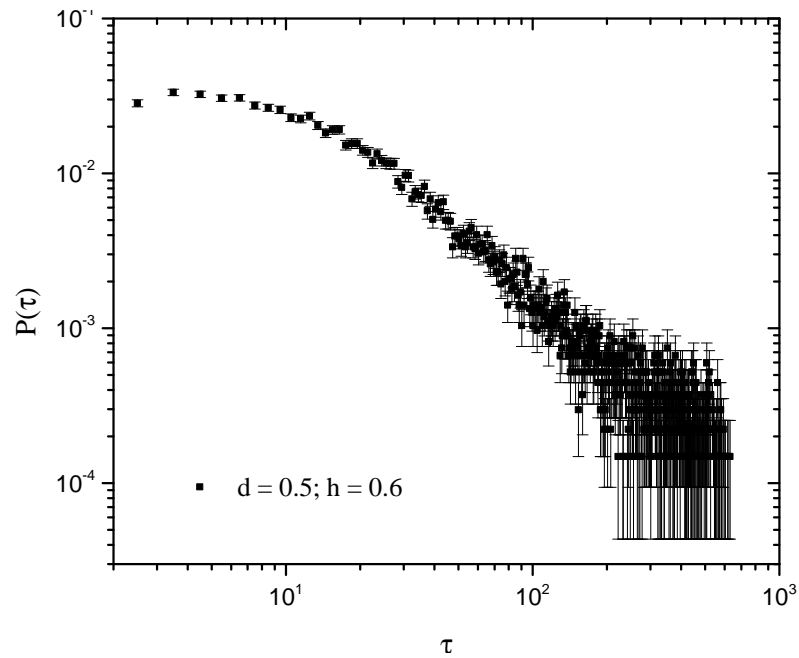


Figure 5.15: Example of the power-law regime for the distribution of eruptions interevent times for  $d = 0.5$  and  $h = 0.6$ .

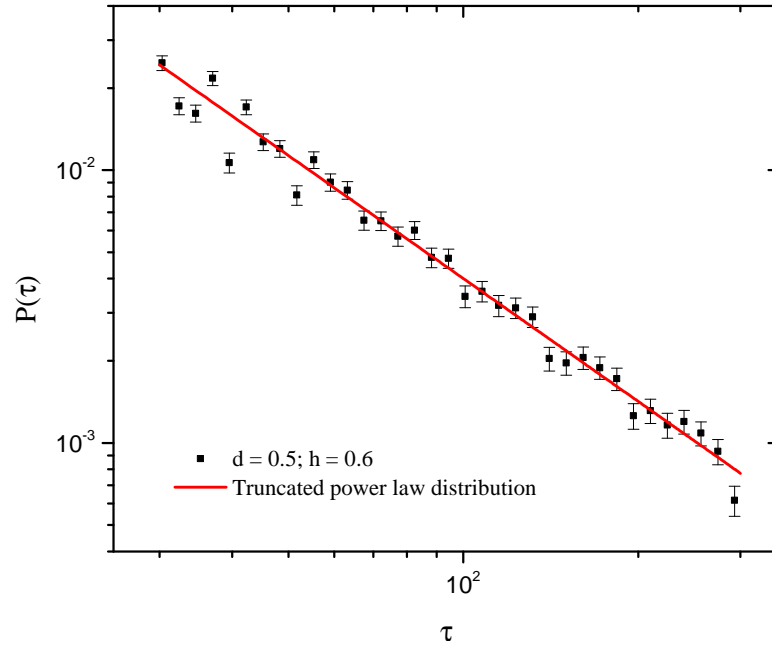


Figure 5.16: Truncated power-law fit of the distribution for the time range  $\tau \in [30, 300]$  with  $\alpha = 1.51 \pm 0.05$  (b)

diagram for the model is presented in Figure 5.17. We observed a consistent power-law behavior for small values of  $d/h$ . A power-law distribution of the interevent times implies that there is no characteristic time describing eruptions, and points towards the criticality of the temporal behavior of the model. This kind of behavior applied to volcanism would signify that volcanic systems are extremely sensitive to small perturbations, and this power-law distribution of interevent times of volcanic eruption has previously been observed for the Piton de la Fournaise volcano [Grasso and Bachelery, 1995]. As  $d/h$  increases, the temporal distribution of eruptions becomes better characterized by the log-normal distribution and the exponential distribution. An exponential distribution of interevent times implies that eruptions behave as a Poisson process where all the events are independent and occur at a constant rate in time. This kind of temporal behavior has previously been observed in volcanic activity [Wickman, 1966, Reymont, 1969, Klein, 1982, De la Cruz-Reyna, 1991]. The log-normal distribution implies that the interevent times between eruptions can be the result of a multiplicative process. This also signifies that eruption times are correlated with elements of clustering. Clustering has been reported by Gusev et al. [2003]; Gusev [2008] and Marzocchi and Zaccarelli [2006], and the log-normal distribution

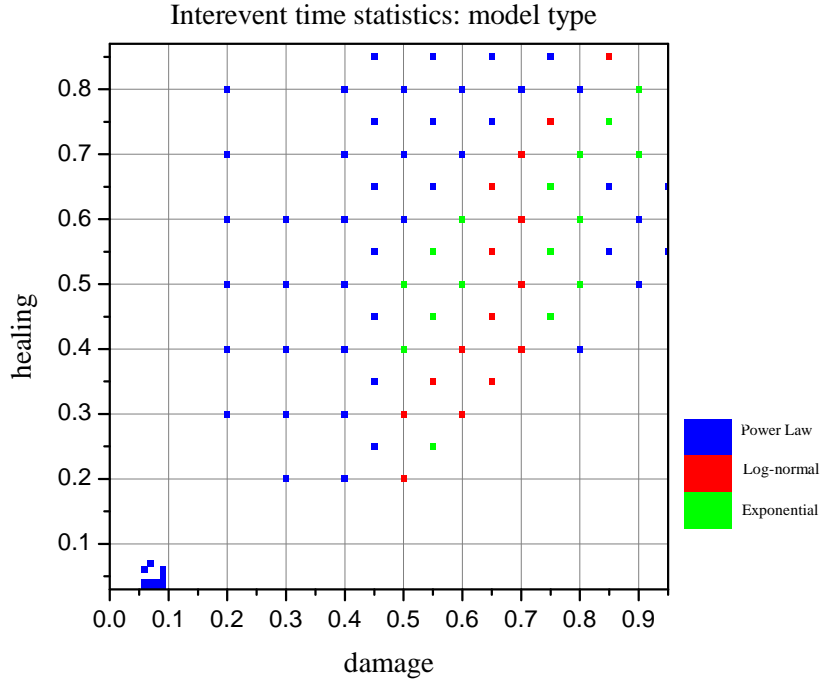


Figure 5.17: Phase diagram representing the best model to describe the interevent data for varying values of  $d$  and  $h$ .

was used to describe the temporal behavior of the currently most active volcanoes [Sanchez and Shcherbakov, 2012].

### 5.3.2 Model 2 ( $256 \times 256$ )

For model 2, we studied a range of values for  $d$  and  $h$  ( $0.06 < d < 0.50$  and  $0.04 < h < 0.50$ ) in order to simulate different volcanic settings. We investigated several connectivity values ( $C = 0.50; C = 0.55; C = 0.60; C = 0.65$ ). For the same reasons than for model 1, we will focus our analysis on the results for  $C = 0.60$  but will also present the phase diagrams for the other values of  $C$ . We investigated the size, interevent times and duration of eruptions.

#### 5.3.2.1 Frequency-size distribution of eruptions

In model 2, we observed several distinct behaviors for the distribution of eruption sizes. We tested the truncated exponential, Eq. (5.7), the truncated log-normal, Eq. (5.8) and the truncated power-law distributions, Eq. (5.6) in order to describe

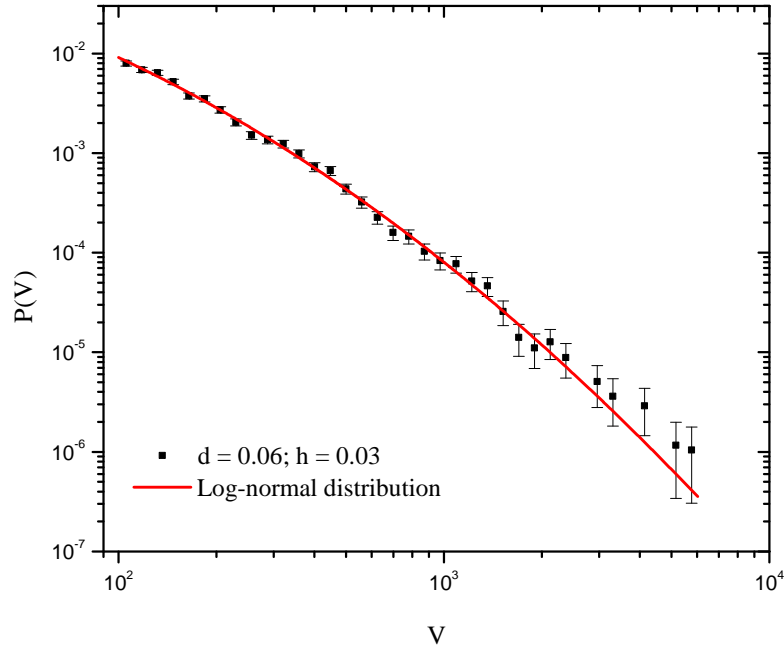


Figure 5.18: Truncated log-normal fit of the distribution for the size range  $V \in [100, 10000]$  with  $\mu = 3.52 \pm 0.58$  and  $\sigma = 1.46 \pm 0.17$  (model 2)

the frequency-size distribution of events. Figures 5.18 and 5.19 show examples of the fitted frequency-size distributions.

The phase diagram for the models best describing the frequency-size distribution of eruptions is presented in Figure 5.20. Some of the frequency-size distributions could not be fitted by the models for a significant range of sizes and are labeled as "other" in Figure 5.20. Figure 5.21, 5.22 and 5.23 display the variations in parameter values for the truncated log-normal and the power-law distributions. We note that the log-normal behavior seems to be more represented for small values of  $d$  and  $h$  while the power-law distribution provides a better fit for the distributions with larger sizes of  $d$  and  $h$ .

We observed an increase in the values of  $\mu$  and a decrease in the values of  $\sigma$  when  $d/h$  decreases. The power-law exponent takes large values when  $d/h$  is large and small while the intermediate values of  $d/h$  are represented by a small  $\alpha$ . In Figures 5.24 and 5.25, we show the phase diagrams for the best fitting frequency-size distribution models for  $C = 0.55$  and  $C = 0.65$ . For  $C = 0.50$ , none of the distributions can be fitted to the data for a long enough range. This is due to the low amount of eruptions produced from this connectivity value. For  $C = 0.55$  and

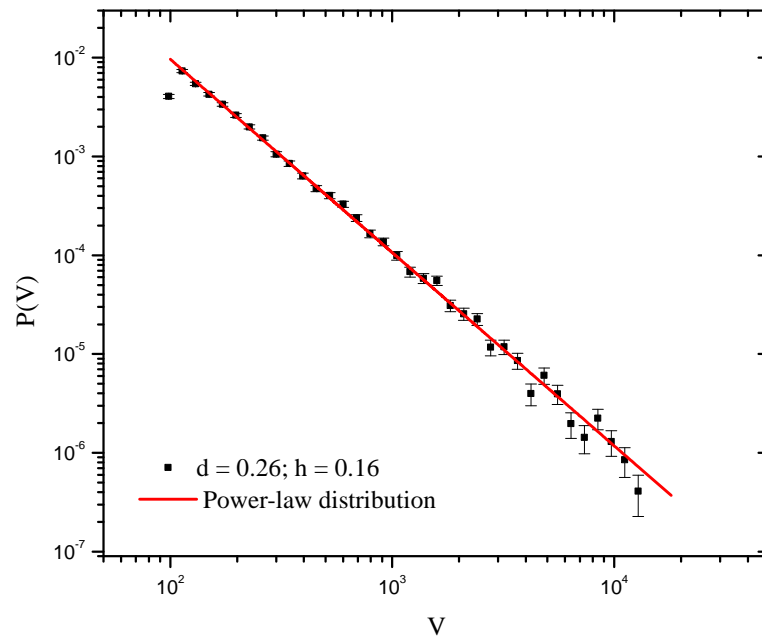


Figure 5.19: Truncated power-law fit of the distribution for the size range  $V \in [100, 10000]$  with  $\alpha = 1.96 \pm 0.03$  (model 2)

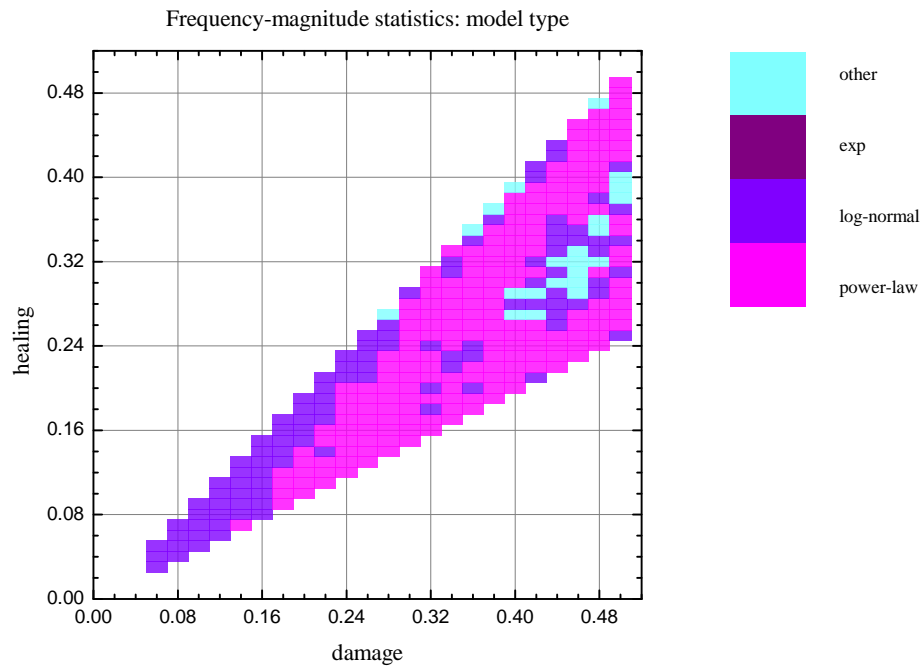


Figure 5.20: Phase diagram representing the best model to describe the frequency-size distributions from model 2 for varying values of  $d$  and  $h$ . The label "other" corresponds to cases where the 3 distributions considered were not a good fit



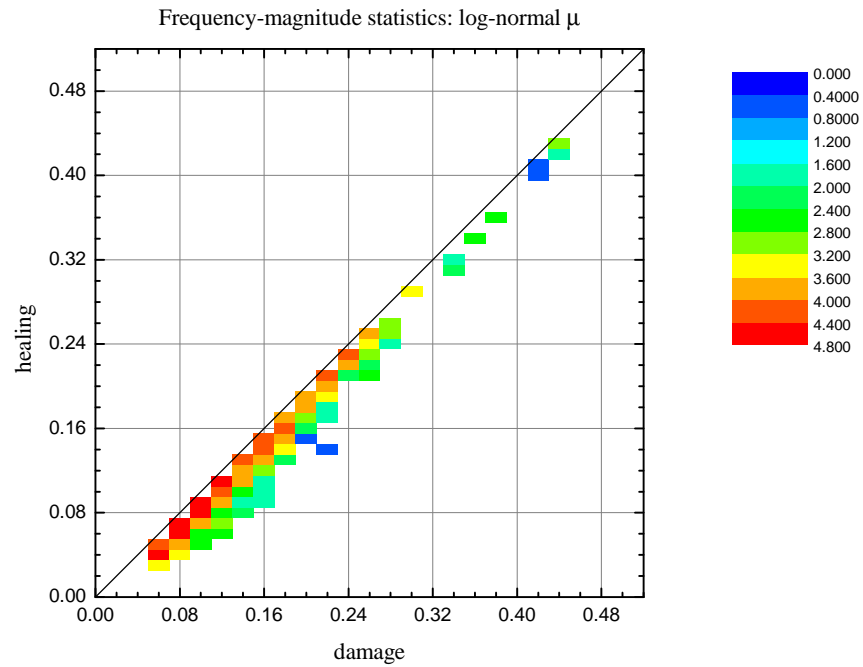


Figure 5.21: Phase diagram representing variations in the  $\mu$  parameter for the truncated log-normal fit of the size distribution of events for  $C = 0.6$

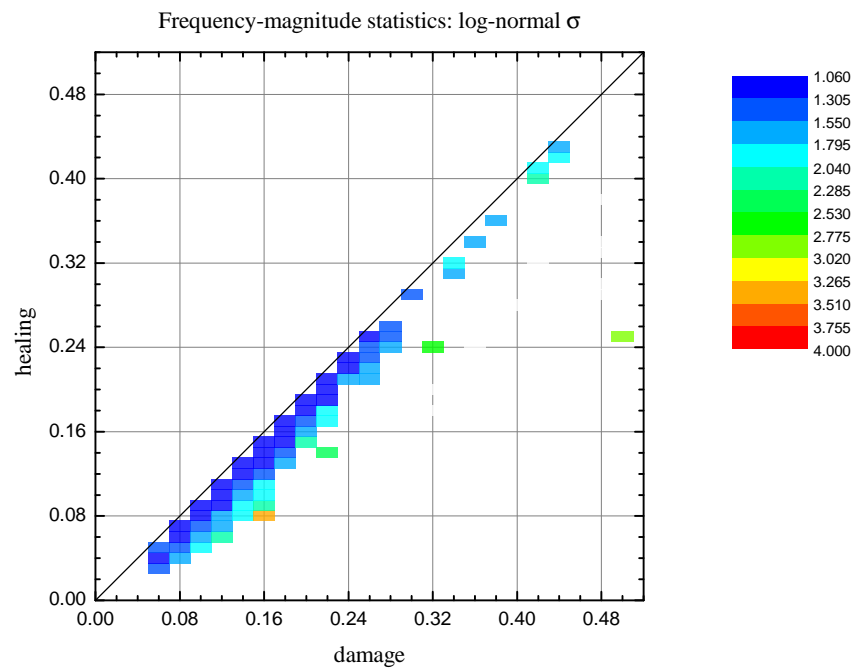


Figure 5.22: Phase diagram representing variations in the  $\sigma$  parameter for the truncated log-normal fit of the size distribution of events for  $C = 0.6$

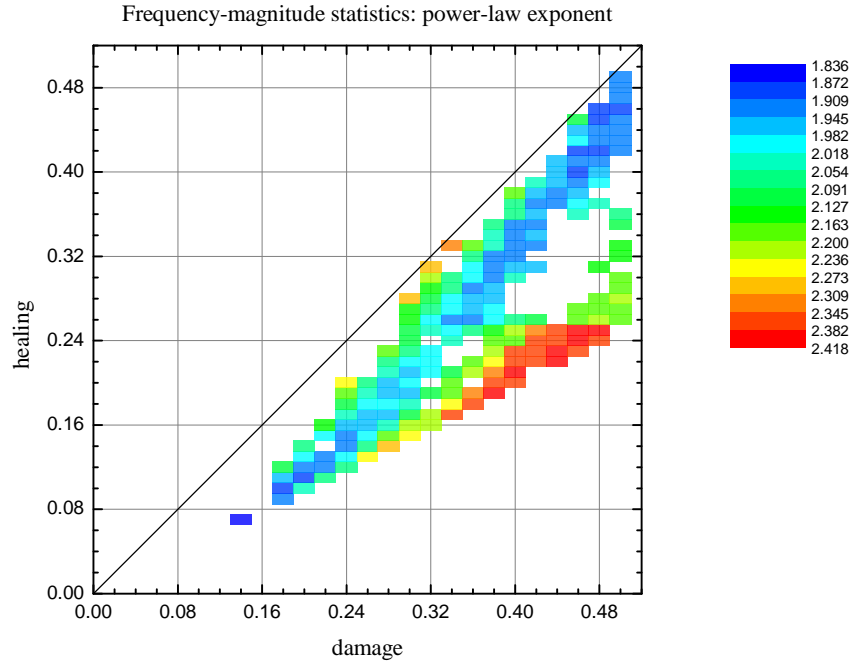


Figure 5.23: Phase diagram representing variations in the  $\alpha$  parameter for the truncated power-law fit of the size distribution of events for  $C = 0.6$ .

$C = 0.65$ , we observe slightly different behaviors. The log-normal distribution is a better fit when  $d/h$  is large and this trend is reversed for  $C = 0.65$ : the power-law is a better fit for large values of  $d/h$ .

### 5.3.2.2 Temporal behavior, interevent times

In model 2, we observed the same 3 behaviors as for model 1, described by the truncated exponential, the truncated log-normal and the truncated power-law distributions. Examples of those distributions of interevent times are displayed in Figures 5.26, 5.27 and 5.28.

The changes in temporal behavior according to the  $d/h$  ratio are shown in the phase diagram in Figure 5.29. The power-law distribution is a better fit for low values of  $d/h$  while the exponential and the log-normal distributions become better fits when  $d/h$  increases.

The variations in the parameter values for each fit seem to be consistent and we observed an increase of  $\mu$  and a decrease of  $\sigma$  with increasing  $d/h$  (Figure 5.30 and 5.31). The exponential rate parameter  $\lambda$  (Figure 5.32) and the power-law exponent  $\alpha$  increase for increasing  $d/h$  (Figure 5.33). Figures 5.34, 5.35 and 5.36 present the

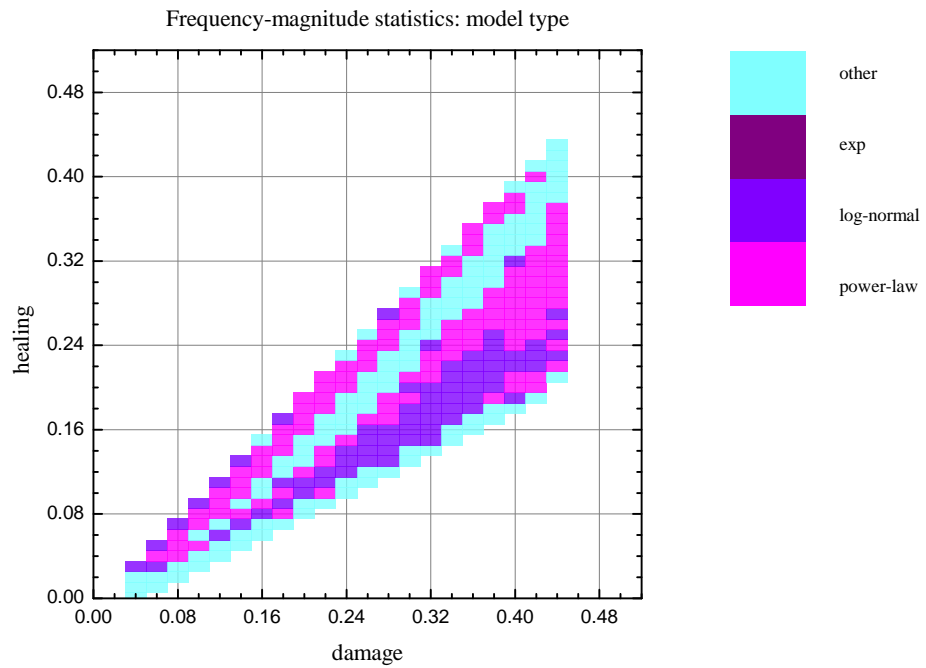


Figure 5.24: Phase diagram representing the best model to describe the frequency-size distributions from model 2 for varying values of  $d$  and  $h$  for  $C = 0.55$

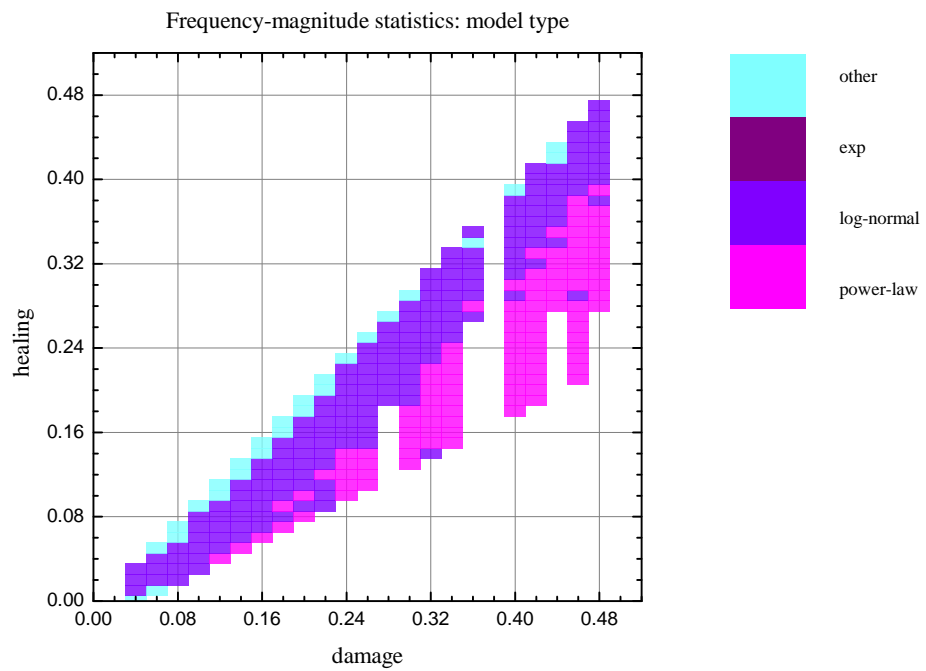


Figure 5.25: Phase diagram representing the best model to describe the frequency-size distributions from model 2 for varying values of  $d$  and  $h$  for  $C = 0.65$

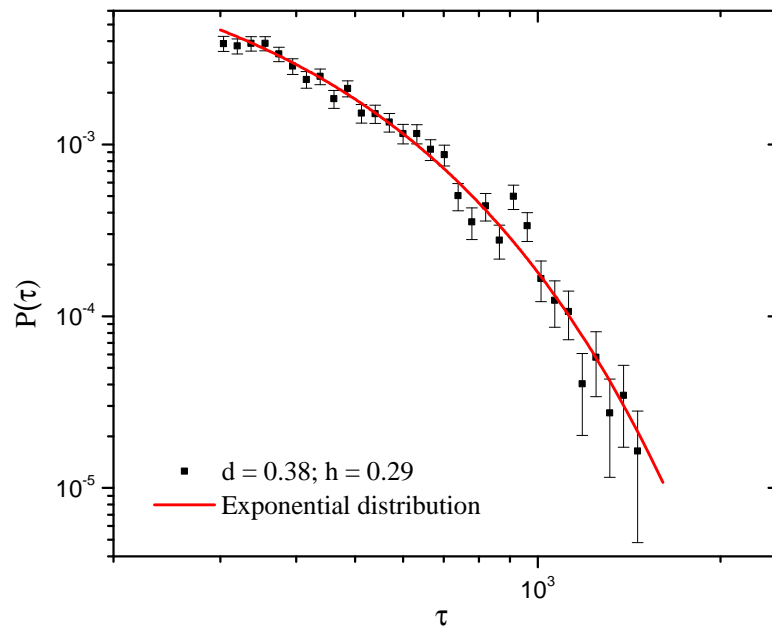


Figure 5.26: Truncated exponential fit of the distribution for the time range  $\tau \in [300, 10000]$  with  $\lambda = 215.4 \pm 11$

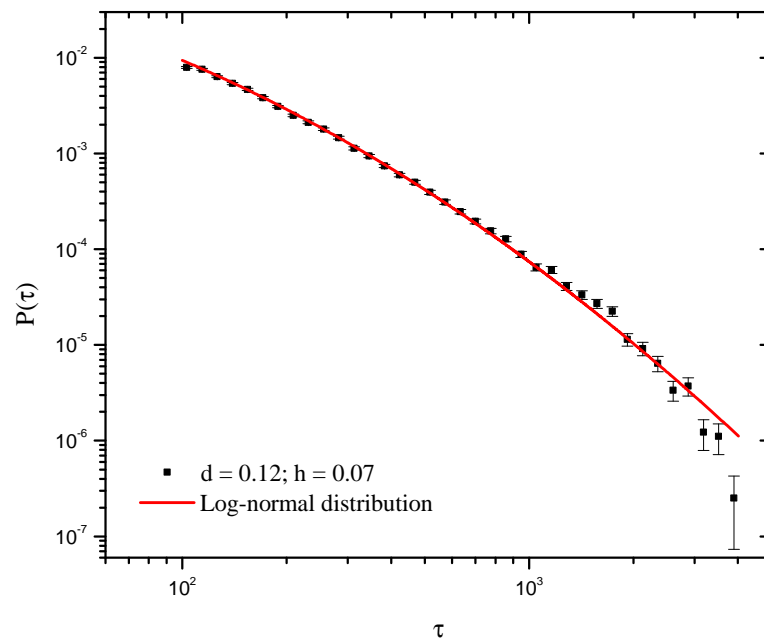


Figure 5.27: Truncated log-normal fit of the distribution for the time range  $\tau \in [100, 10000]$  with  $\mu = 3.53 \pm 0.22$  and  $\sigma = 1.42 \pm 0.07$

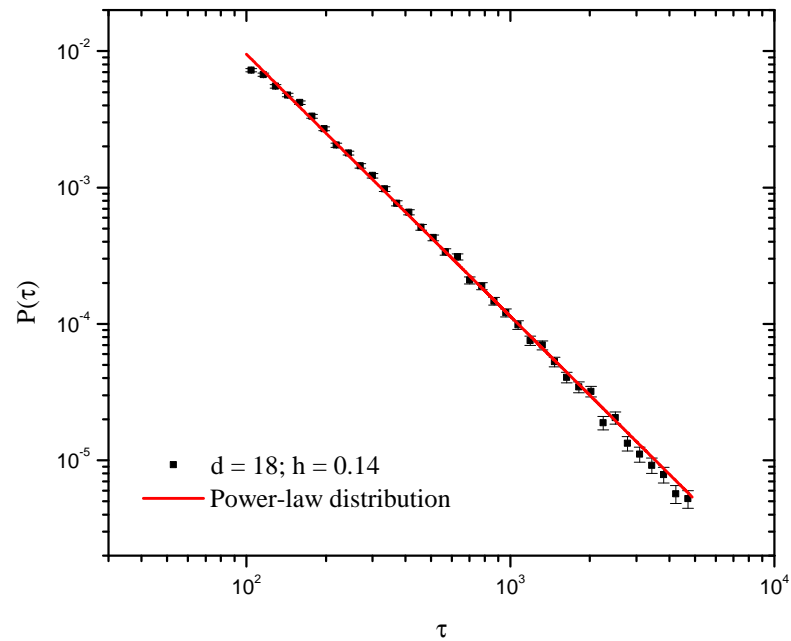


Figure 5.28: Truncated power-law fit of the distribution for the time range  $\tau \in [100, 10000]$  with  $\alpha = 1.92 \pm 0.02$

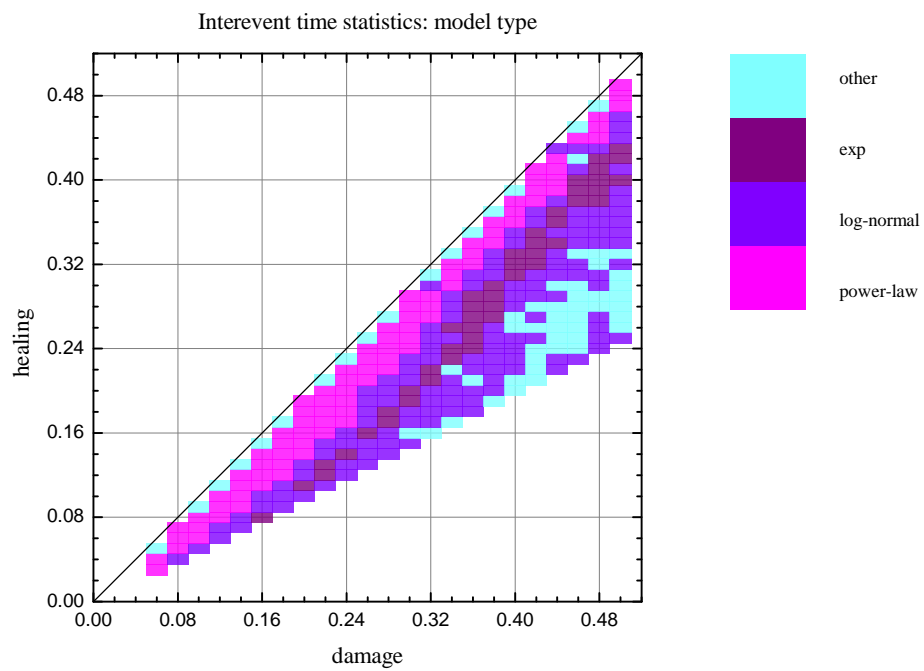


Figure 5.29: Phase diagram representing the best model to describe the interevent distributions from model 2 for varying values of  $d$  and  $h$  for  $C = 0.60$

interevent time behavior for  $C = 0.50$ ;  $C = 0.55$  and  $C = 0.65$  respectively. For those 3 connectivity values, we observed that a lot of the distributions cannot be fitted for a long enough time range. Indeed, values of  $C$  that are too small or too large will either prevent eruptions from happening or trigger constant eruptions, making the interevent times statistics very low.

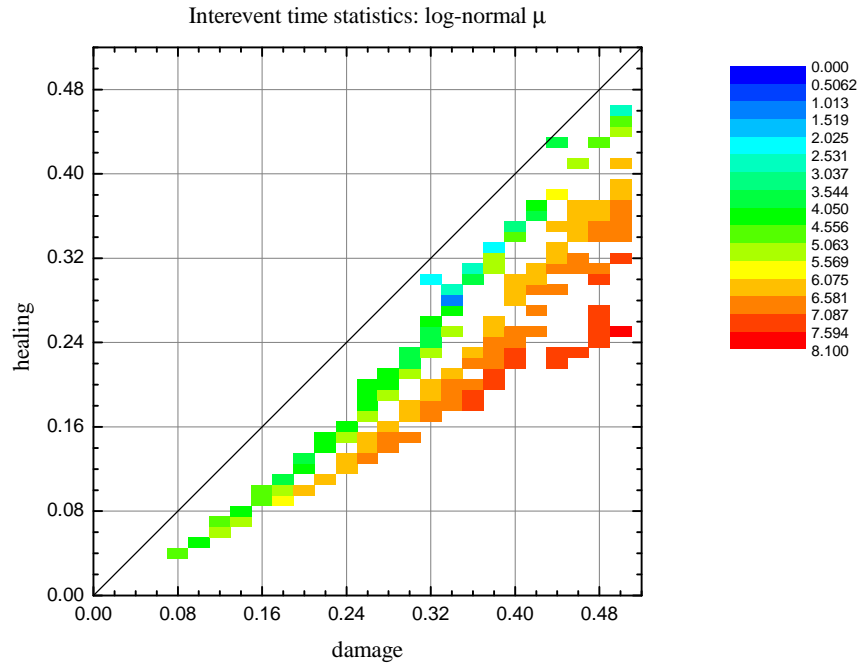


Figure 5.30: Phase diagram representing variations in the  $\mu$  parameter for the truncated log-normal fit of the size distribution of events for  $C = 0.6$ .

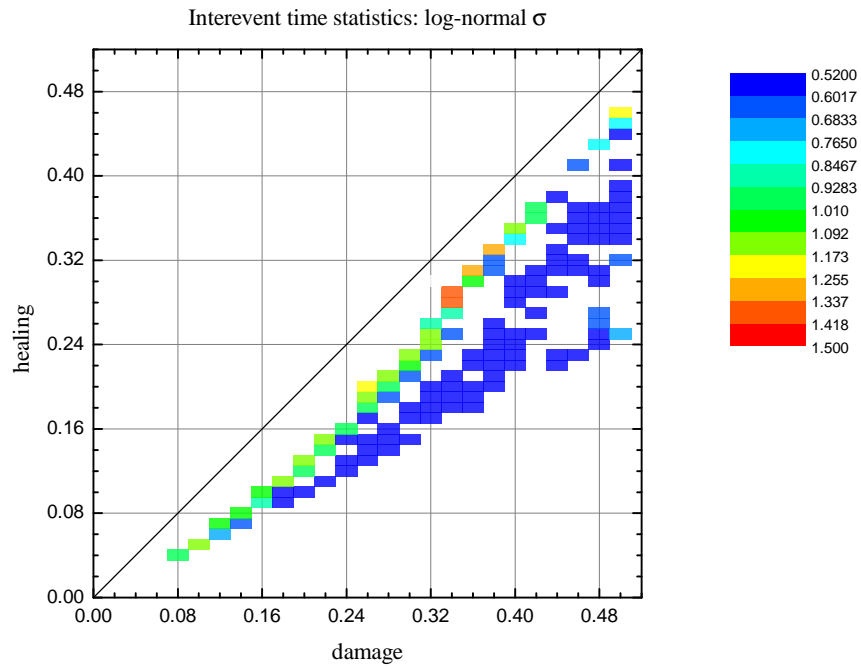


Figure 5.31: Phase diagram representing variations in the  $\sigma$  parameter for the truncated log-normal fit of the size distribution of events for  $C = 0.6$ .

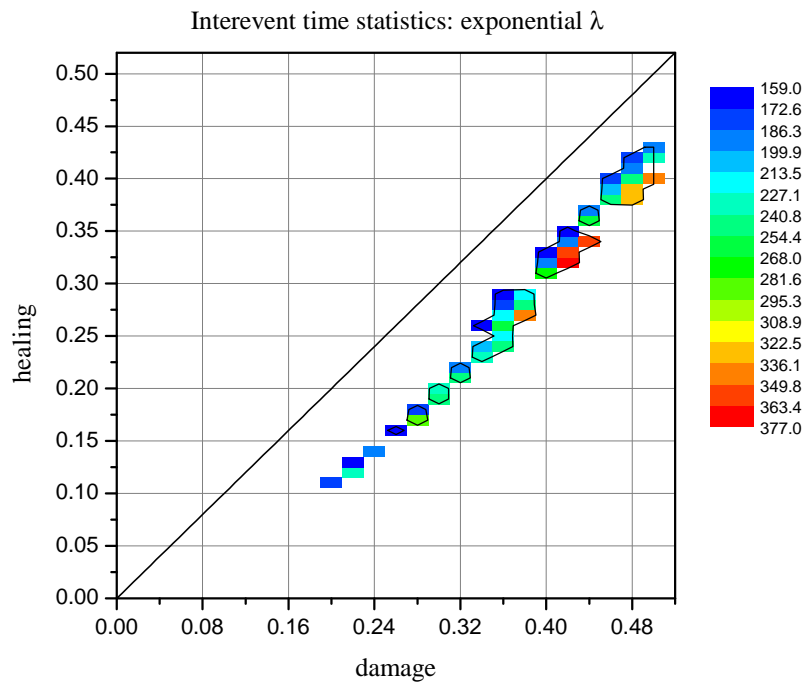


Figure 5.32: Phase diagram representing variations in the  $\lambda$  parameter for the truncated exponential fit of the size distribution of events for  $C = 0.6$ .

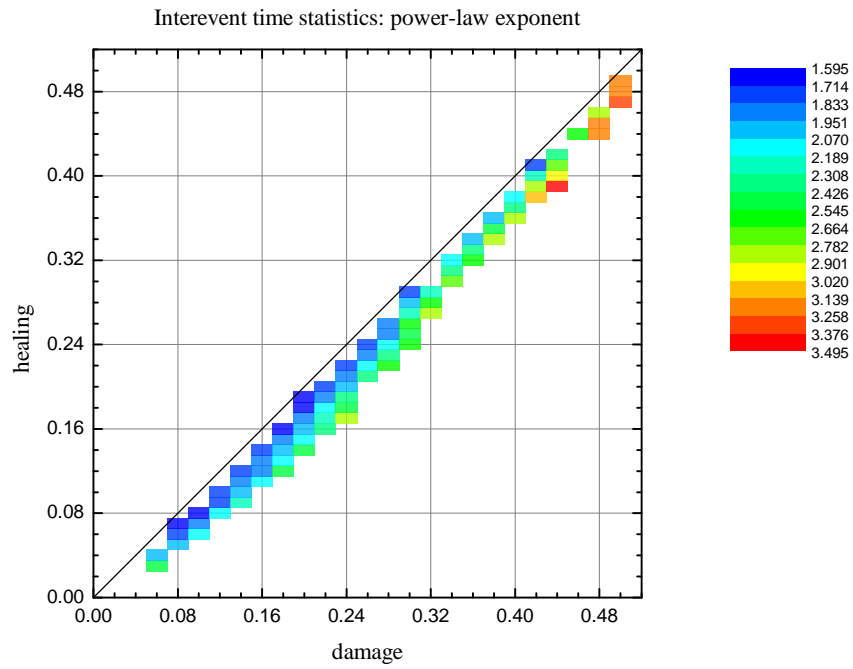


Figure 5.33: Phase diagram representing variations in the  $\alpha$  parameter for the truncated power-law fit of the size distribution of events for  $C = 0.6$ .

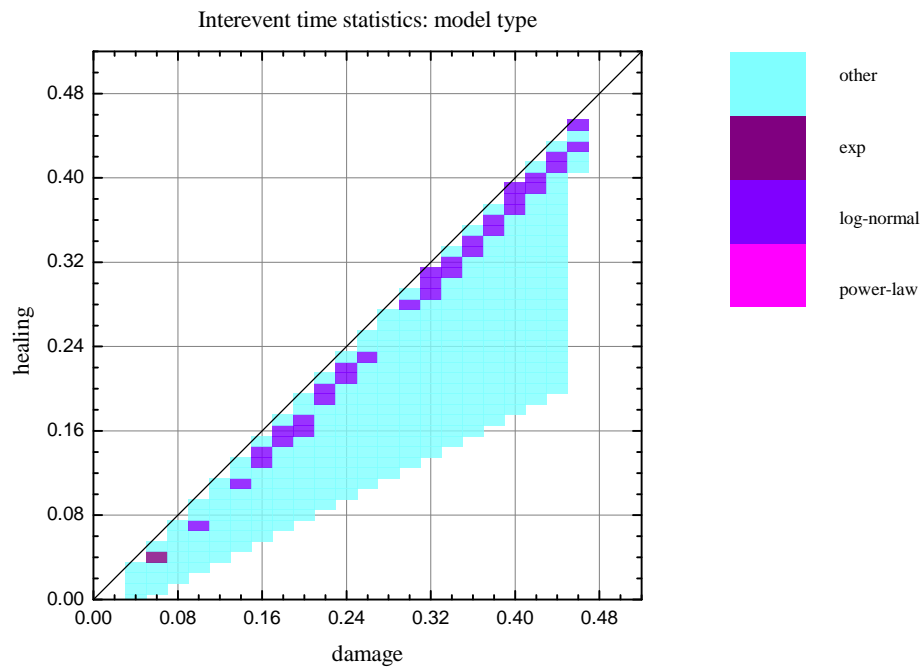


Figure 5.34: Phase diagram representing the best model to describe the interevent distributions from model 2 for varying values of  $d$  and  $h$  for  $C = 0.50$



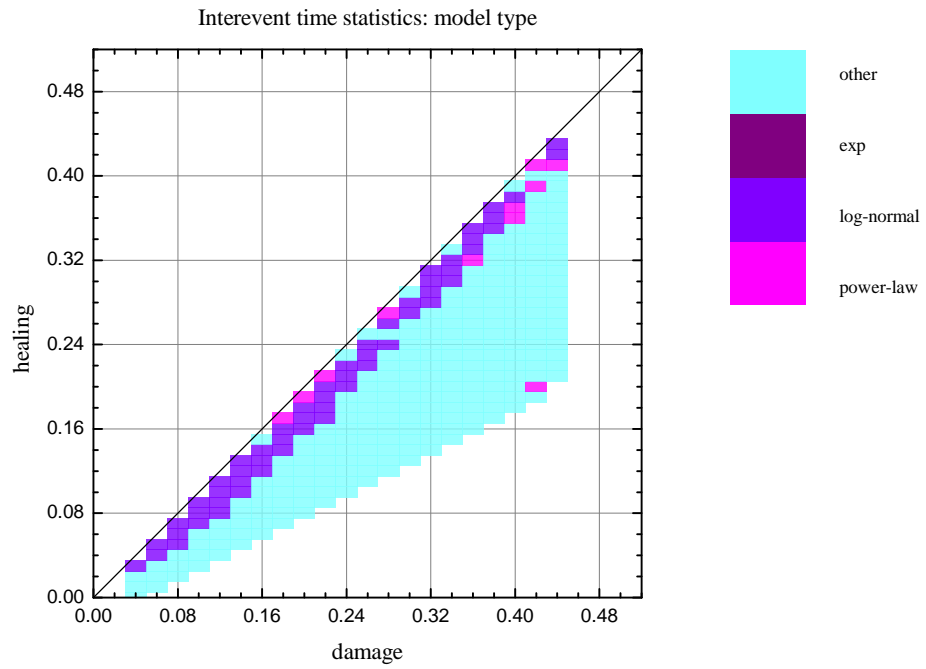


Figure 5.35: Phase diagram representing the best model to describe the interevent distributions from model 2 for varying values of  $d$  and  $h$  for  $C = 0.55$

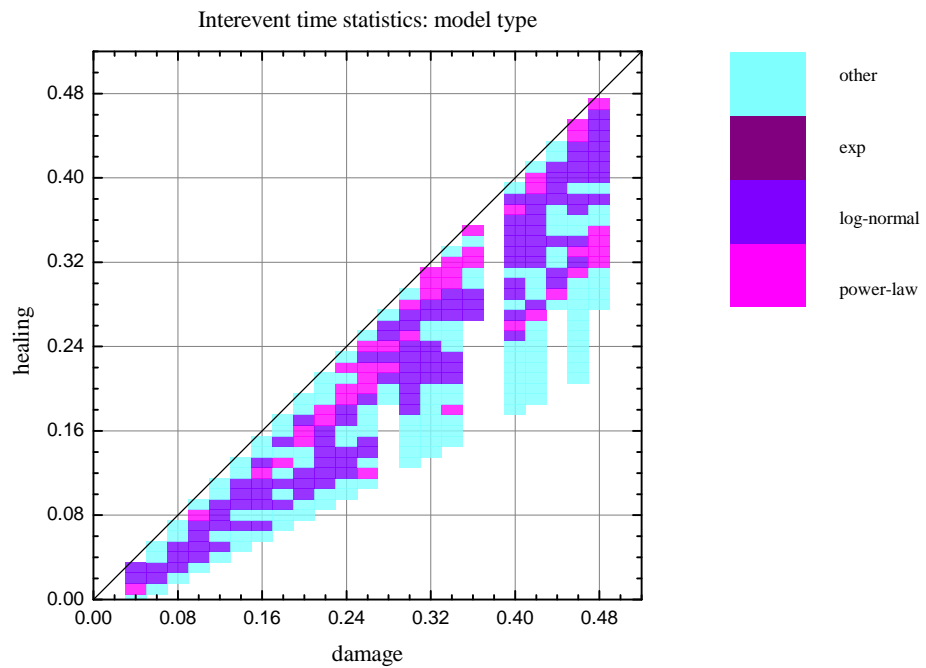


Figure 5.36: Phase diagram representing the best model to describe the interevent distributions from model 2 for varying values of  $d$  and  $h$  for  $C = 0.65$

### 5.3.3 Temporal behavior, eruption duration

For model 2, we also investigated the distribution of eruption durations  $P(t)$ . Similarly to interevent times, we observed 3 temporal regimes described by the truncated exponential, truncated log-normal and truncated power-law distributions (see Figures 5.37, 5.38 and 5.39). The phase diagram representing the best model for the distribution of eruption durations is presented in Figure 5.40. We observe a power-law behavior for low  $d/h$  ratios while larger  $d/h$  values lead to log-normally distributed eruption durations. The exponential behavior is only observed for a small amount of  $d/h$  ratios.

The parameter values for the log-normal and power-law fits are displayed in Figures 5.41, 5.42 and 5.43. Both parameters  $\mu$  and  $\sigma$  of the log-normal distribution increase for increasing values of  $d/h$  while the power-law exponent  $\alpha$  displays no pattern according to the value of the  $d/h$  ratio.

The best fitting models for the eruption duration distributions for  $C = 0.50$ ;  $C = 0.55$  and  $C = 0.65$  are presented in Figures 5.44, 5.45 and 5.46. For connectivity values of  $C = 0.50$  and  $C = 0.55$ , only a small amount of distributions are fitted by the models over a long enough time range. For  $C = 0.65$ , we observe that the power-law behavior of eruption duration seems to become less prevalent while the exponential distribution becomes a better fit for intermediate values of  $d/h$ .

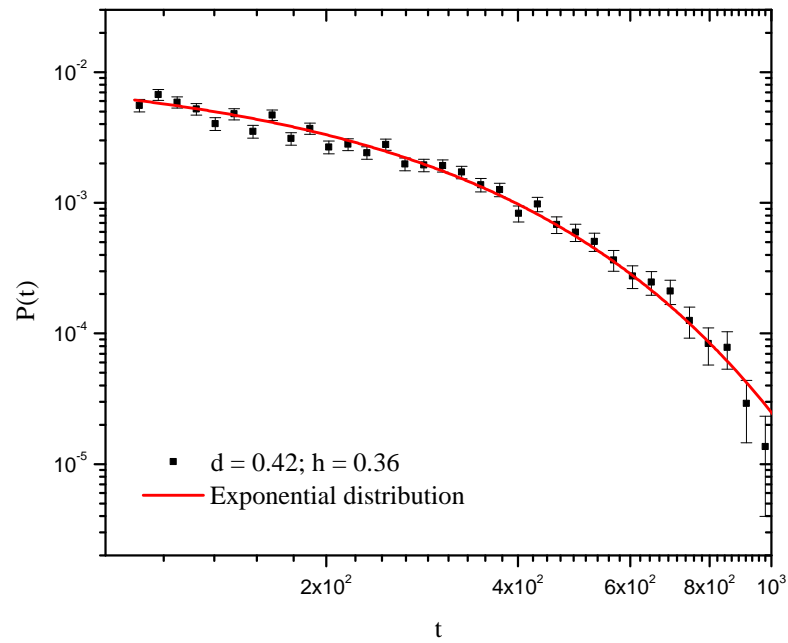


Figure 5.37: Truncated exponential fit of the distribution for the time range  $t \in [100, 10000]$  with  $\lambda = 163.5 \pm 6.9$

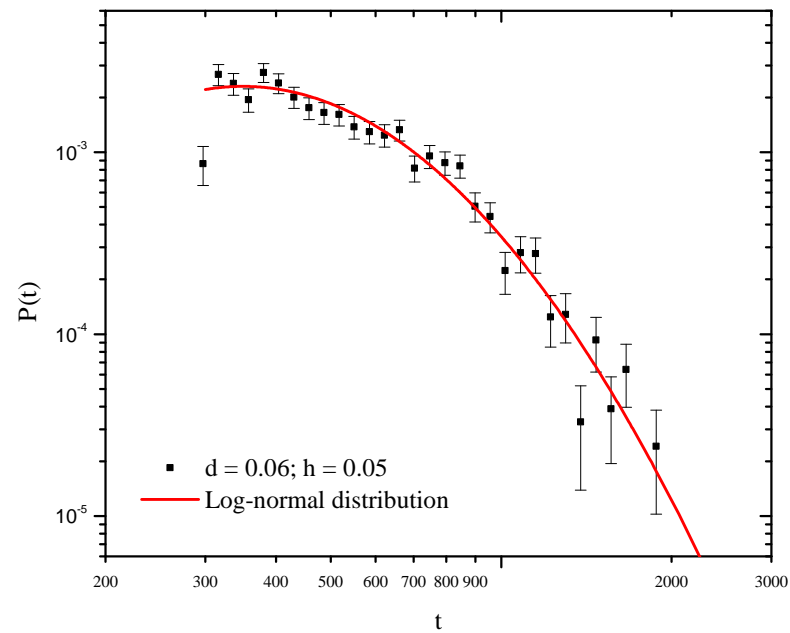


Figure 5.38: Truncated log-normal fit of the distribution for the time range  $t \in [100, 10000]$  with  $\mu = 5.7 \pm 0.18$  and  $\sigma = 0.81 \pm 0.13$

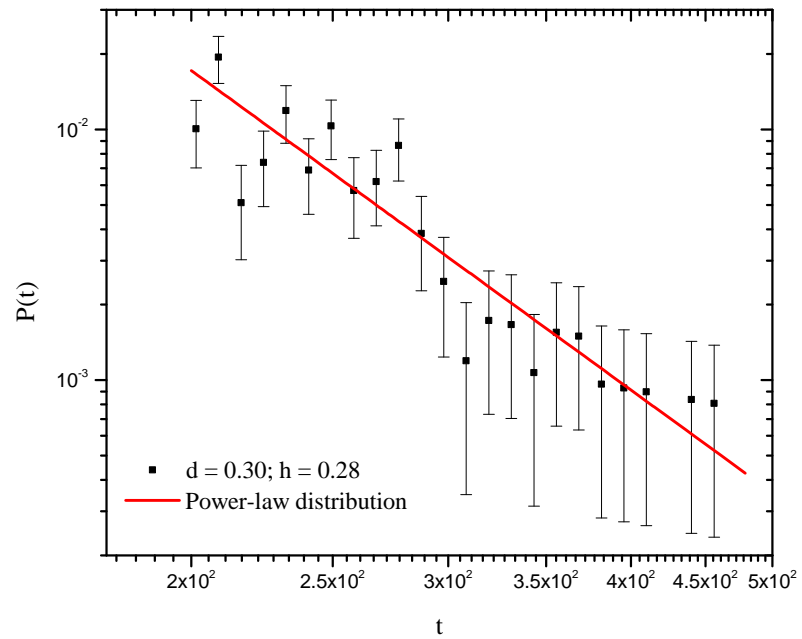


Figure 5.39: Truncated power-law fit of the distribution for the time range  $t \in [200, 10000]$  with  $\alpha = 4.23 \pm 0.75$

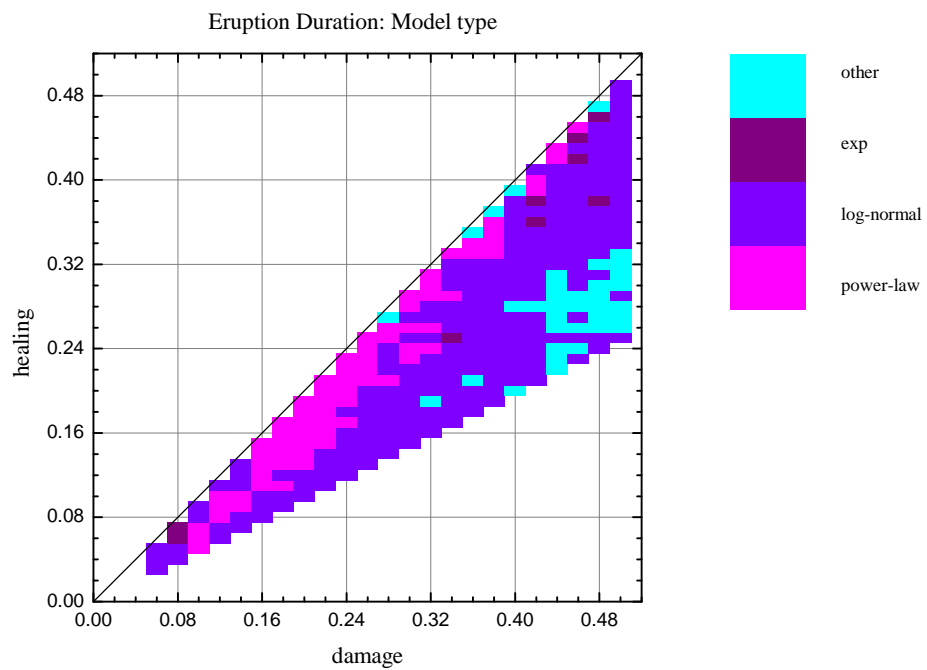


Figure 5.40: Phase diagram representing the best model to describe the duration distributions from model 2 for varying values of  $d$  and  $h$  for  $C = 0.60$

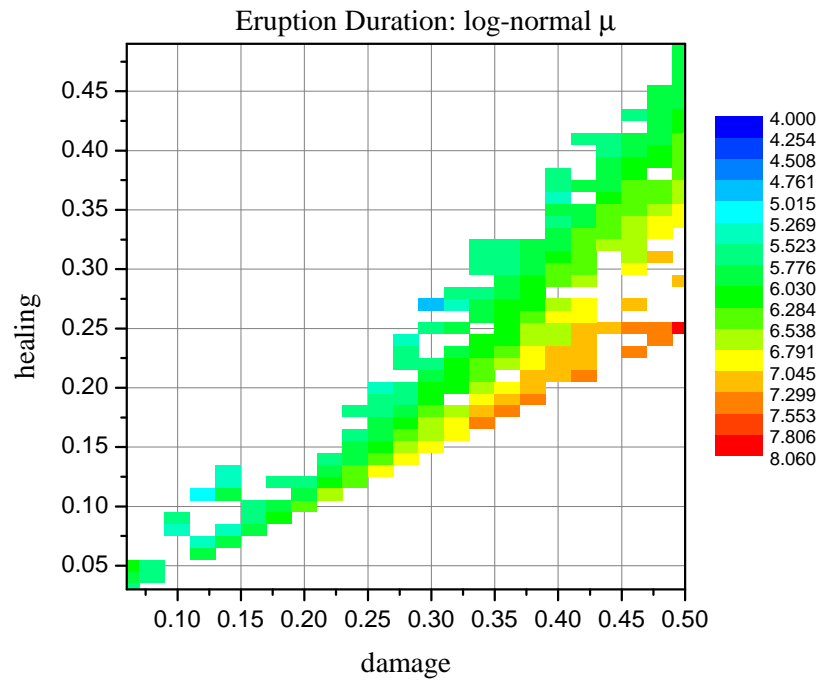


Figure 5.41: Phase diagram representing variations in the  $\mu$  parameter for the truncated log-normal fit of the distribution of durations for  $C = 0.60$ .

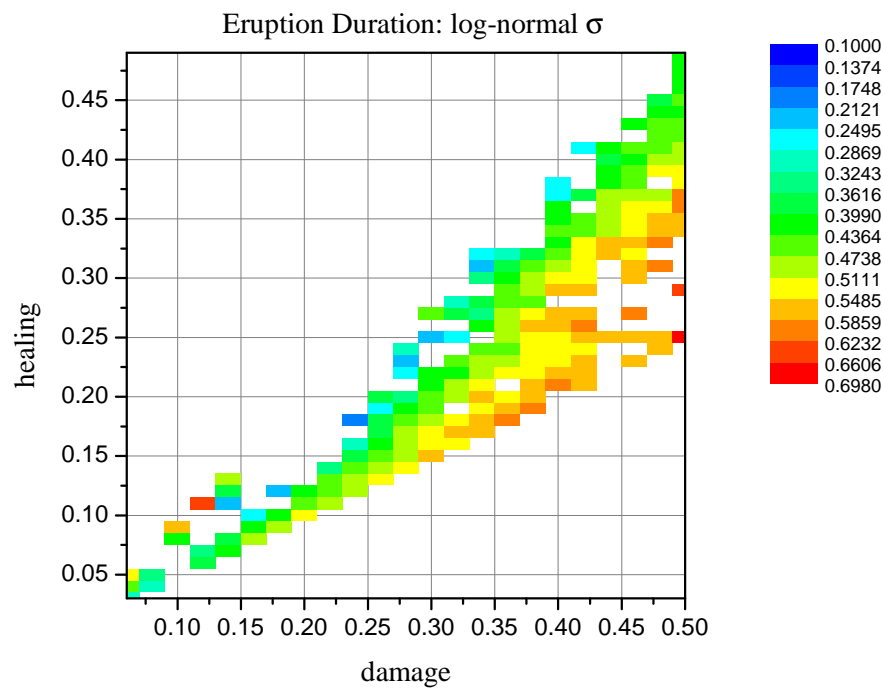


Figure 5.42: Phase diagram representing variations in the  $\sigma$  parameter for the truncated log-normal fit of the distribution of durations for  $C = 0.60$ .

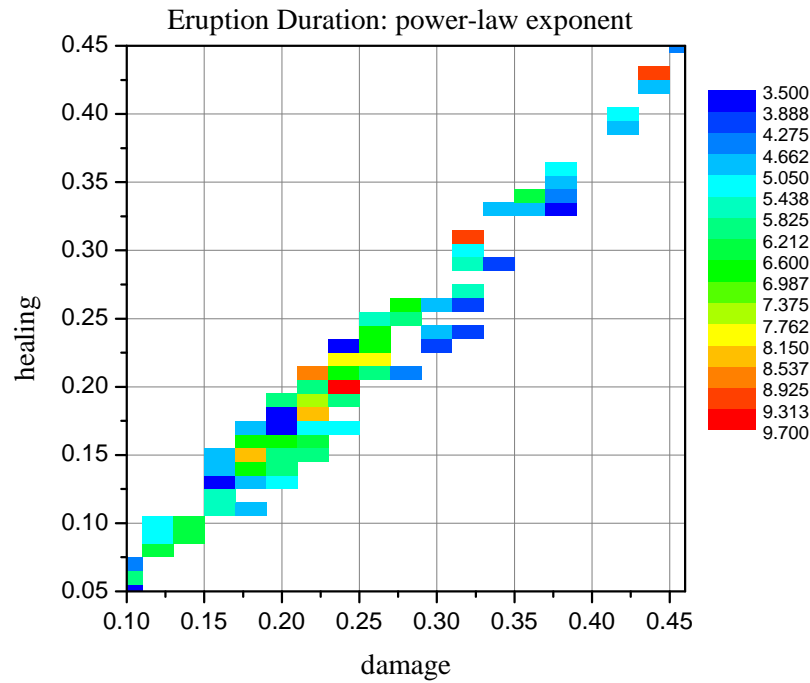


Figure 5.43: Phase diagram representing variations in the  $\alpha$  parameter for the truncated power-law fit of the distribution of durations for  $C = 0.60$ .

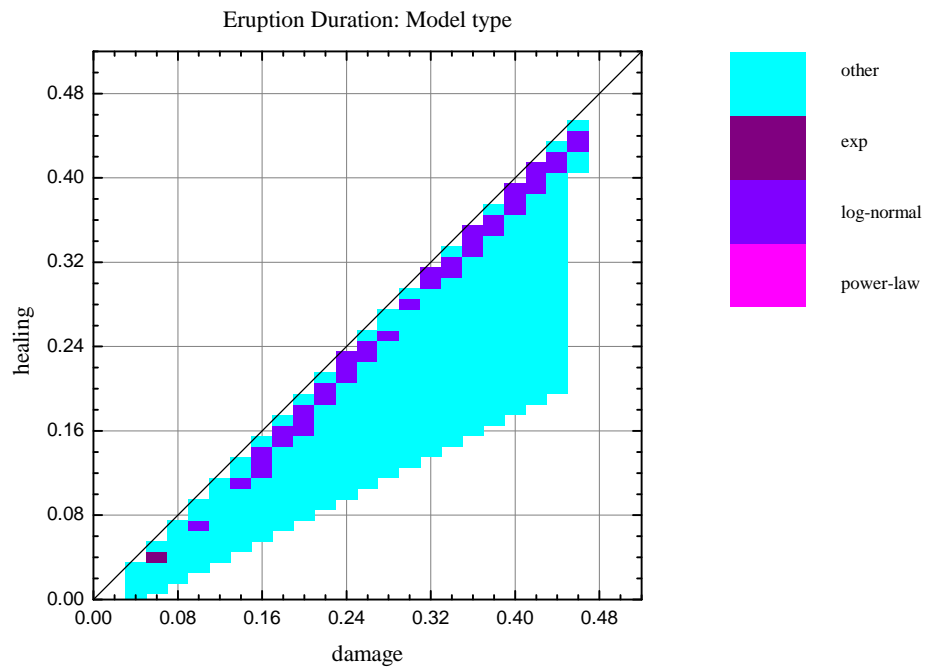


Figure 5.44: Phase diagram representing the best model to describe the duration distributions from model 2 for varying values of  $d$  and  $h$  for  $C = 0.50$

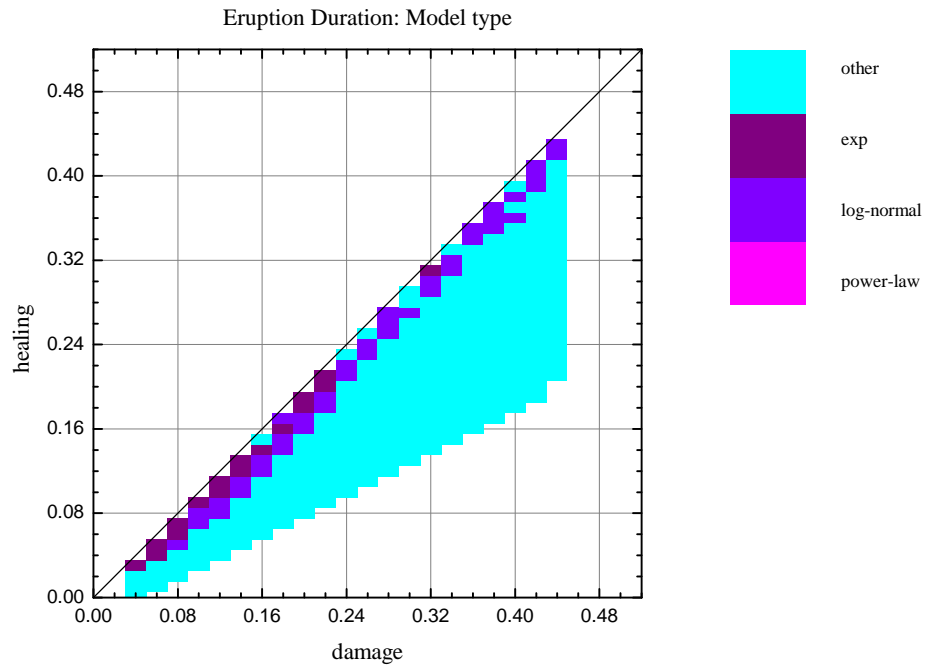


Figure 5.45: Phase diagram representing the best model to describe the duration distributions from model 2 for varying values of  $d$  and  $h$  for  $C = 0.55$

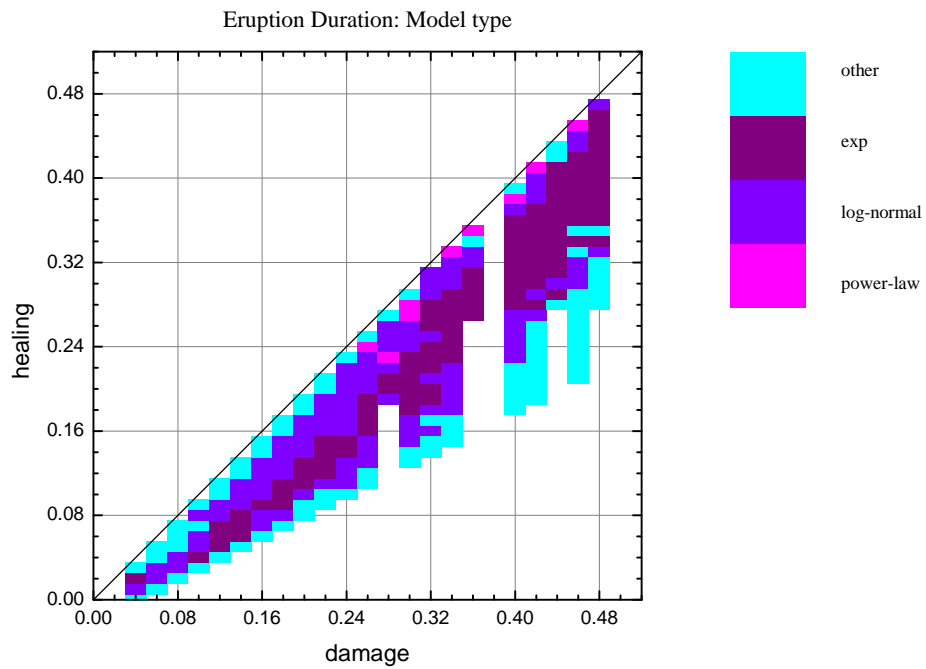


Figure 5.46: Phase diagram representing the best model to describe the duration distributions from model 2 for varying values of  $d$  and  $h$  for  $C = 0.65$

## 5.4 Conclusions

In this chapter, a cellular automaton is introduced in order to investigate the interactions between the magma and the solid crust and reproduce the statistical behavior of eruptions. Through numerical simulations of two versions of the model, we collected the size and occurrence time of volcanic events and studied their probability density functions.

For model 1, the frequency-size distributions of events displayed a consistent behavior for the range of values of  $d$  and  $h$  investigated and the truncated power-law distribution was defined as the best model to describe it. The power-law exponent  $\alpha$  of the distribution was found to vary with different values of  $d$  and  $h$ . We observed a peak in the size distribution of events attributed to the finite-size of the system. This kind of power-law behavior is consistent with the observed size distribution of volcanic events on a global scale [Newhall and Self, 1982, Simkin, 1993] but also on individual volcanoes [Lahaie and Grasso, 1998]. The variation in the value of  $\alpha$  can be attributed to different tectonic settings as well as different magma and crustal properties.

For model 2, we observe an additional behavior characterized by the log-normal distribution. This additional regime manifests for small values of  $d$  and  $h$  for  $C = 0.60$ . This kind of distribution is a heavy tailed distribution and points toward a power-law distribution of large eruptions and a roll-over for small sizes.

The temporal behavior of models 1 and 2 was characterized by three distinct regimes according to the  $d/h$  ratio. For small values of  $d/h$ , the interevent time distribution was best modeled by a truncated power-law distribution. This type of behavior indicates criticality in the system and the absence of a characteristic time scale for the interevent time and has been observed on the Piton de la Fournaise volcano [Grasso and Bachelery, 1995]. For larger values of  $d/h$ , the distribution can be described by either an exponential or a log-normal distribution. The exponential distribution implies the existence of a Poisson process and could be hypothesized as reproducing the behavior of closed conduit systems. In this case, the path to the surface is closed and the magma particles need to damage the crust completely in order to rise to the surface. After an eruption, since the value of  $h$  is high, the path taken by the magma gets "sealed" and the fracturation process has to start again. The eruptions in that case are independent from each other and the rate of



events is constant. In the case of a log-normally distributed series of eruptions, the events are the result of a multiplicative process and are correlated and clustered. Here, we conclude that we are observing an open conduit system behavior. After an eruption, the path to the surface heals but does not do so fast enough and becomes therefore a "preferential" path to the surface for the magma particles. Eruptions times will influence the probability of occurrence of the next event. These two types of statistical temporal behavior have been observed on empirical data [Wickman, 1966, Klein, 1982, De la Cruz-Reyna, 1991, Gusev, 2008, Marzocchi and Zaccarelli, 2006, Sanchez and Shcherbakov, 2012]. The duration of events from model 2 display the same 3 behaviors: truncated exponential, truncated power-law and truncated log-normal.

Our model has proven to be efficient at reproducing the statistical behavior of volcanic eruptions. We were able to obtain the multiple temporal behavior observed in nature and the size distribution of events in the model was consistent with the data. Our results emphasize the critical and unpredictable nature of volcanic eruptions and the need to use statistical approaches to understand the processes involved in the triggering of volcanic eruptions.

## References

- H. Akaike. A new look at the statistical model identification. *IEEE Trans. Autom. Contr.*, 19(6):716–723, 1974.
- P. Bak, K. Chen, and C. Tang. A forest fire model and some thoughts on turbulence. *Phys. Lett. A*, 147:297–300, 1990.
- S.V. Buldyrev, A.L. Barabási, F. Caserta, S. Havlin, H.E. Stanley, and T. Vicsek. Anomalous interface roughening in porous media: Experiment and model. *Phys. Rev. A*, 45(12):8313–8316, 1992.
- B. Chopard and M. Droz. *Cellular Automata Modeling of Physical Systems*, volume 122. Springer, 1998.
- A.C. Cohen. Censored, truncated, and grouped estimation. In E.L. Crow and K. Shimizu, editors, *Lognormal Distributions, Theory and Applications EL Crow & K. Shimizu, eds. Marcel Dekker, New York*, pages 139–172. 1988.
- Á. Corral, A. Ossó, and J.E. Llebot. Scaling of tropical-cyclone dissipation. *Nat. Phys.*, 6(9):693–696, 2010.
- G.M. Crisci, S. Di Gregorio, R. Rongo, M. Scarpelli, W. Spataro, and S. Calvari. Revisiting the 1669 Etnean eruptive crisis using a cellular automata model and implications for volcanic hazard in the Catania area. *J. Volcanol. Geotherm. Res.*, 123(1-2):211–230, 2003. ISSN 0377-0273.
- S. De la Cruz-Reyna. Poisson-distributed patterns of explosive eruptive activity. *Bull. Volcanol.*, 54(1):57–67, 1991. doi: 10.1007/BF00278206.
- C. Del Negro, L. Fortuna, A. Herault, and A. Vicari. Simulations of the 2004 lava flow at Etna volcano using the magflow cellular automata model. *Bull. Volcanol.*, 70(7):805–812, 2008. ISSN 0258-8900.
- A. Deluca and A. Corral. Fitting and goodness-of-fit test of non-truncated and truncated power-law distributions. *Acta Geophys.*, 61(6):1351–1394, 2013.
- P. Diodati, F. Marchesoni, and S. Piazza. Acoustic emission from volcanic rocks: An example of self-organized criticality. *Phys. Rev. Lett.*, 67(17):2239–2243, 1991.

- P. Diodati, P. Bak, and F. Marchesoni. Acoustic emission at the Stromboli volcano: scaling laws and seismic activity. *Earth Planet. Sci. Lett.*, 182(3):253–258, 2000.
- U Frisch, Y. Hasslacher, and B. Pomeau. Lattice-gas automata for the navier-stokes equation. *Phys. Rev. Lett*, 56(14):1505, 1986.
- J.R. Grasso and P. Bachelery. Hierarchical organization as a diagnostic approach to volcano mechanics: Validation on Piton de la Fournaise. *Geophys. Res. Lett.*, 22(21):2897–2900, 1995.
- A. A. Gusev. Temporal structure of the global sequence of volcanic eruptions: Order clustering and intermittent discharge rate. *Phys. Earth Planet. Inter.*, 166(3-4): 203–218, 2008. doi: 10.1016/j.pepi.2008.01.004.
- A. A. Gusev, V.V. Ponomareva, O. A. Braitseva, I. V. Melekestsev, and L. D. Sulerzhitsky. Great explosive eruptions on Kamchatka during the last 10,000 years: Self-similar irregularity of the output of volcanic products. *J. Geophys. Res.*, 108(B2):2126, 2003. doi: 10.1029/2001JB000312.
- P.M. Hannon and R.C. Dahiya. Estimation of parameters for the truncated exponential distribution. *Commun. Stat. A-Theor.*, 28(11):2591–2612, 1999.
- J. Hardy, Y. Pomeau, and O. De Pazzis. Time evolution of a two-dimensional model system. i. invariant states and time correlation functions. *J. Math. Phys.*, 14:1746, 1973.
- Y. Y. Kagan. Seismic moment distribution revisited: I. Statistical results. *Geophys. J. Int.*, 148(3):520–541, 2002.
- F. W. Klein. Patterns of historical eruptions at Hawaiian volcanos. *J. Volcanol. Geotherm. Res.*, 12(1-2):1–35, 1982.
- F. Lahaie and J.R. Grasso. A fluid-rock interaction cellular automaton of volcano mechanics: Application to the Piton de la Fournaise. *J. Geophys. Res.*, 103(B5): 9637–9649, 1998. ISSN 0148-0227.
- B. D. Malamud, G. Morein, and D. L. Turcotte. Log-periodic behavior in a forest-fire model. *Nonlinear Proc. Geophys.*, 12(5):575–585, 2005.

- B.D. Malamud, D.L. Turcotte, F. Guzzetti, and P. Reichenbach. Landslide inventories and their statistical properties. *Earth Surf. Proc. Land.*, 29(6):687–711, 2004.
- W. Marzocchi and L. Zaccarelli. A quantitative model for the time-size distribution of eruptions. *J. Geophys. Res.*, 111(B4):B04204, 2006.
- J. Massey and J. Frank. The kolmogorov-smirnov test for goodness of fit. *J. Am. Stat. Assoc.*, 46(253):68–78, 1951.
- C. G. Newhall and S. Self. The volcanic explosivity index (VEI) – An estimate of explosive magnitude for historical volcanism. *J. Geophys. Res.*, 87(C2):1231–1238, 1982.
- Y. Ogata. Detection of precursory relative quiescence before great earthquakes through a statistical-model. *J. Geophys. Res.*, 97(B13):19845–19871, 1992.
- Z. Olami, H.J.S. Feder, and K. Christensen. Self-organized criticality in a continuous, nonconservative cellular automaton modeling earthquakes. *Phys. Rev. Lett.*, 68(8):1244, 1992.
- J. D. Pelletier. Statistical self-similarity of magmatism and volcanism. *J. Geophys. Res.*, 104(B7):15425–15438, 1999.
- E. Piegari, V. Cataudella, R. Di Maio, L. Milano, M. Nicodemi, and R. Scandone. A model of volcanic magma transport by fracturing stress mechanisms. *Geophys. Res. Lett.*, 35(6):L06308, 2008.
- E. Piegari, R. Di Maio, R. Scandone, and L. Milano. A cellular automaton model for magma ascent: Degassing and styles of volcanic eruptions. *J. Volcanol. Geotherm. Res.*, 202(1):22–28, 2011.
- E. Piegari, R. Di Maio, and R. Scandone. Analysis of the activity pattern of volcanoes through self-organized crack networks: The effect of density barriersan application to Vesuvius activity in the period 1631–1944. *Earth Planet. Sci. Lett.*, 2013.
- R.A. Reymont. Statistical analysis of some volcanologic data regarded as series of point events. *Pure Appl. Geophys.*, 74(1):57–77, 1969.
- M.P. Ryan. Neutral buoyancy and the mechanical evolution of magmatic systems. *Geochem. Soc. Spec. Publ.*, pages 259–288, 1987.

- 
- M. Sahimi. Flow phenomena in rocks: from continuum models to fractals, percolation, cellular automata, and simulated annealing. *Rev. Mod. Phys.*, 65(4):1393, 1993.
- L. Sanchez and R. Shcherbakov. Temporal scaling of volcanic eruptions. *J. Volcanol. Geotherm. Res.*, 247-248:115–121, 2012. doi: 10.1016/j.jvolgeores.2012.08.004.
- A. Schadschneider, W. Klingsch, H. Klüpfel, T. Kretz, C. Rogsch, and A. Seyfried. Encyclopedia of Complexity and System Science. *Springer*, 2009.
- H.R. Shaw and B. Chouet. Fractal hierarchies of magma transport in Hawaii and critical self-organization of tremor. *J. Geophys. Res.*, 96(B6):10191–10, 1991.
- L. Siebert and T. Simkin. *Volcanoes of the World: An Illustrated Catalog of Holocene Volcanoes and their Eruptions*. Smithsonian Institution, Global Volcanism Program Digital Information Series, GVP-3, 2002-. <http://www.volcano.si.edu/world/>.
- T. Simkin. Terrestrial volcanism in space and time. *Annu. Rev. Earth Planet. Sci.*, 21:427–452, 1993.
- A. Vicari, H. Alexis, C. Del Negro, M. Coltelli, M. Marsella, and C. Proietti. Modeling of the 2001 lava flow at Etna volcano by a Cellular Automata approach. *Environ. Model. Softw.*, 22(10):1465–1471, 2007. ISSN 1364-8152.
- F. E. Wickman. Repose period patterns of volcanoes. I. Volcanic eruptions regarded as random phenomena. *Ark. Kem. Mineral. Geol.*, 4(4):291, 1966.

## Chapter 6 Discussion and Concluding Remarks

Throughout this thesis I have been addressing the following goals:

- Understanding the formation and evolution of calderas and impact craters in the solar system using a comparative planetology approach,
- Investigating the global temporal behavior of volcanic eruptions on Earth,
- Understanding the nonlinear interactions taking place in the solid crust which lead to an eruption.

To fulfill these goals, I combined several approaches. The first method involved statistical analysis on empirical data. More specifically, I employed scaling analyses on multiple datasets. First, I performed the analysis on planetary calderas and impact craters to investigate landform formation and evolution processes in the solar system. Zooming in to the Earth, I then used the same type of scaling analysis on the temporal behavior of volcanic eruptions. The results from these statistical studies lead me to conclude that taking a global approach when studying volcanic processes is a novel and efficient approach in volcanology. Considering volcanoes as a complex system, I developed a computer model with the goal of reproducing the behavior of all volcanoes, independent of their location and magma properties, using only a limited set of parameters. This study allowed me to reproduce temporal and size distributions of volcanic events in a variety of settings. In this chapter, I summarize all the results from the studies and draw conclusions on their implications for the field of volcanology.

## 6.1 Landform formation in the solar system

In Chapter 2, I focused on investigating volcano formation in the solar system using a comparative planetology approach. To do so, I chose to study the distribution of sizes properties of calderas on Earth, Mars, Venus and Io. The diameter and area of this planetary feature are related to the size of the underlying magma chamber and can be used as a proxy for estimating the potential of volcanic eruptions [Lipman, 2000]. The distribution of magma chamber sizes for planetary bodies is directly related to the crustal thickness and the properties of magma material such as density, concentration of volatiles, etc. [Mouginis-Mark and Rowland, 2001]. For these reasons, the study of planetary calderas is of major importance to understand volcano formation in the solar system as well as to uncover subsurface characteristics of the planetary bodies investigated. Using the mean caldera diameter and area of each planetary body as scaling factors, I performed a scaling analysis on their respective probability distribution functions. I observed a collapse of all the distributions into a single one, the Generalized Extreme Value (GEV) distribution. Looking closer to the Earth, I also performed a similar scaling analysis on the distributions of caldera sizes according to their crustal settings. There again, I observed a collapse of all the distributions into the GEV distribution with similar parameters to the planetary bodies investigated. These results lead me to conclude that the use of comparative planetology is a powerful tool to understand formation and evolution mechanisms of planetary landforms. The processes responsible for caldera formation are similar on the four planetary bodies considered and independent of the crustal settings on Earth. Using the properties of the GEV distribution for each planetary body considered could lead to a better estimation of the probability of caldera maximum size, and therefore also the estimation of the maximum sizes of magma chambers on a given body.

In Chapter 3, I utilized the comparative planetology approach to investigate impact craters. I investigated their size distributions on Earth, Mars, Mercury, Venus and the Moon. I was able to uncover specific statistical features for those planetary bodies. First, I found a difference in behavior for small and large craters on the Earth and Moon. I hypothesized that these could be the statistical manifestation of the morphological difference between simple and complex craters. With respect to the Moon, this difference could also be explained by two distinct bombardment periods with different impactor size ranges. On Mars, Mercury, Venus and the Moon, I

observed a collapse of the distributions of crater sizes in large craters. The formation and evolution mechanisms are therefore similar for large craters for the planetary bodies considered. On Venus, the deviation for small craters can be attributed to atmospheric effects.

Through statistical scaling analysis I demonstrated that the processes governing caldera formation on Earth, Mars, Venus and Io are similar and that large impact craters on Mars, Mercury, the Moon and Venus follow the same formation and evolution mechanisms. Using a similar statistical technique on two different landforms, I highlighted the importance of comparative planetology in the study of geomorphological features. Building on these results, further analysis could entail the study of magma chamber depth on Venus, Mars and Io as well as the investigation of the evolution of small impact craters on Mars, Mercury, Venus and the Moon.

## **6.2 Temporal behavior of volcanic eruptions on Earth**

In Chapter 4, I focused on temporal aspects of volcanism on Earth by performing comprehensive statistical analysis of time intervals between consecutive eruptions. Assuming that volcanism operates through non-linear threshold dynamics, I took a global approach to study the temporal behavior of volcanic eruptions. I collected eruption histories for 26 of the most active volcanoes throughout the world as well as for 163 less active volcanoes that I grouped into regional datasets. I performed a scaling analysis on the distributions of interevent times of all the datasets considered, using the mean interevent time as a scaling factor. I observed a collapse of all the distributions into a single one, characterized by a log-normal distribution. I performed this analysis with several magnitude cutoffs to ensure the validity of results for the broadest range of eruption sizes. The results from this analysis lead me to conclude that volcanic eruptions on Earth can be the result of a multiplicative process and that eruption times are correlated with elements of clustering. The obtained universality of the distribution of interevent times is a manifestation of self-similar nature of volcanic processes in time. It also indicates that the temporal structure of volcanic sequences deviates from simple Poisson statistics. These results imply that the processes involving magma transfer from the mantle to the crust, that are responsible for



the triggering of volcanic eruptions, operate on a global scale. These results stress the importance of using statistical approaches when studying eruptions instead of classic deterministic methods. They also have implications in the design of future volcano hazard assessment programs.

### 6.3 Modeling of volcanic eruptions

Following up the results from Chapter 4 which imply that volcanic systems could be regarded as a critical system, I designed a computer model to simulate the interactions between the magma and the solid crust on a global scale. To do so, I used a cellular automata approach which has been proved successful at reproducing the dynamics of various natural hazards [Ogata, 1992, Olami et al., 1992, Bak et al., 1990]. Using simple dynamics with a small number of parameters, the model was able to reproduce the power-law size distribution of volcanic events implying the self-similarity of eruptions [Newhall and Self, 1982, Simkin, 1993, Lahaie and Grasso, 1998]. Looking at the temporal behavior of volcanic eruptions, the model displayed three different regimes: power-law, log-normal and exponential. The first one hints towards the criticality of the system and correlates with observations from the Piton de la Fournaise volcano [Grasso and Bachelery, 1995]. The exponential distribution of the model interevent times could describe the behavior of closed conduit volcanic systems, implying a Poisson process for eruptions [De la Cruz-Reyna, 1991]. The log-normal distribution describes events resultant from a multiplicative process and displays clustering of the events. This could represent the behavior of open conduit systems and has been shown to describe the temporal behavior of some active volcanoes [Sanchez and Shcherbakov, 2012].

### 6.4 Future work

The results from this thesis emphasize the importance of statistical methods and computer modeling in order to study complex natural systems. Where the use of deterministic approaches often fail at defining reliable prediction models, statistical analysis of data combined with modeling can lead to a better understanding of the processes in play. Future work would entail a broader analysis of the temporal distributions of volcanic events throughout the world in order to uncover more clearly the

different existing temporal regimes. Distinguishing the location of the eruption (i.e. flank or summit) as well as the event duration during the statistical analysis might help uncover some separate behaviors.

The investigation of the size distribution of volcanic eruptions is a major step in defining better hazard models. Studies of the frequency size-distribution of volcanic eruptions have been mostly focusing on large, explosive eruptions [Simkin, 1993, Mason et al., 2004, Bonadonna and Costa, 2013]. These studies were primarily done using the Volcanic Explosivity Index scale [Newhall and Self, 1982], which only accounts for the amount of tephra and column height produced by an eruption. When studying eruptions on a global scale, it is important to consider every type and size of eruption in order to determine whether or not eruptions truly display scale invariance characteristics. Investigating the frequency size distribution of all types of eruptions is a non-trivial problem since there is no precise magnitude scale for volcanic eruptions describing effusive and explosive eruptions on the same level. An effusive eruption will be treated as a very low magnitude event using the VEI index (due to the non existence of explosive products) even though the amount of lava involved might be very large. The dense rock equivalent (DRE) provides an estimate of the erupted volume using the amount of tephra and lava erupted. Future work could attempt to combine the 2 magnitude scales in order to define a more complete scale, including all types of erupted materials for large but also for small events, in order to determine the statistical characteristics of the different types of eruptions.

Expanding on the work of modeling eruption processes, future work would entail investigating the effect of heterogeneities in the crust and the effect of changes in the magma properties through time. Refining the ratio of  $d/h$  in order to match the distribution parameters describing the interevent time distribution of real volcanoes could also be another step towards better hazard models of the volcanoes considered.

## References

- P. Bak, K. Chen, and C. Tang. A forest fire model and some thoughts on turbulence. *Phys. Lett. A*, 147:297–300, 1990.
- C. Bonadonna and A. Costa. Plume height, volume, and classification of explosive volcanic eruptions based on the weibull function. *Bull. Volcanol.*, 75(8):1–19, 2013.
- S. De la Cruz-Reyna. Poisson-distributed patterns of explosive eruptive activity. *Bull. Volcanol.*, 54(1):57–67, 1991. doi: 10.1007/BF00278206.
- J.R. Grasso and P. Bachelery. Hierarchical organization as a diagnostic approach to volcano mechanics: Validation on Piton de la Fournaise. *Geophys. Res. Lett.*, 22(21):2897–2900, 1995.
- F. Lahaie and J.R. Grasso. A fluid-rock interaction cellular automaton of volcano mechanics: Application to the Piton de la Fournaise. *J. Geophys. Res.*, 103(B5):9637–9649, 1998. ISSN 0148-0227.
- P. W. Lipman. Calderas. In H. Sigurdsson, B. F. Houghton, S. R. McNutt, H. Rymer, and J. Stix, editors, *Encyclopedia of Volcanoes*, pages 643–662. Academic Press, San Fransisco, 2000.
- B.G. Mason, D.M. Pyle, and C. Oppenheimer. The size and frequency of the largest explosive eruptions on earth. *Bull. Volcanol.*, 66(8):735–748, 2004.
- P.J. Mouginis-Mark and S.K Rowland. The geomorphology of planetary calderas. *Geomorphology*, 37:201–223, 2001.
- C. G. Newhall and S. Self. The volcanic explosivity index (VEI) – An estimate of explosive magnitude for historical volcanism. *J. Geophys. Res.*, 87(C2):1231–1238, 1982.
- Y. Ogata. Detection of precursory relative quiescence before great earthquakes through a statistical-model. *J. Geophys. Res.*, 97(B13):19845–19871, 1992.
- Z. Olami, H.J.S. Feder, and K. Christensen. Self-organized criticality in a continuous, nonconservative cellular automaton modeling earthquakes. *Phys. Rev. Lett.*, 68(8):1244, 1992.

- L. Sanchez and R. Shcherbakov. Scaling properties of planetary calderas and terrestrial volcanic eruptions. *Nonlin. Proc. Geophys.*, 19(6):585–593, 2012.
- T. Simkin. Terrestrial volcanism in space and time. *Annu. Rev. Earth Planet. Sci.*, 21:427–452, 1993.

## Appendix A Tables of Volcanic Eruptions Time Series

Group	#eruptions	#volcanoes
Alaska	69	3
Aleutian Islands	122	13
Central America	381	23
Iceland	100	7
Indonesia	561	34
Japan	239	18
Kamchatka	278	11
New Zealand	175	4
South America	416	34

Table A.1: Summary of the eruption data used for the interevent time analysis for the world regions

Volcano	#eruptions	time span	$\tau_n$ [days]	volcano type
Pavlof	39	1790 – 2007	$2086.9 \pm 341.2$	Strato
Trident	13	1913 – 1974	$1852.7 \pm 1034.8$	Strato
Veniaminof	20	1838 – 2008	$3259.4 \pm 1011.7$	Strato

Table A.2: Summary of the data used for the Alaska region with the number of eruptions, the time span, the mean interevent time and the type of volcano.

Volcano	#eruptions	time span	$\tau_n$ [days]	volcano type
Akutan	32	1865 – 1992	$1501.8 \pm 312.5$	Strato
Amukta	5	1878 – 1997	$10836.0 \pm 6933.8$	Strato
Bogoslof	8	1796 – 1992	$10236.1 \pm 4017.2$	Submarine
Cleveland	13	1986 – 2010	$733.2 \pm 211.7$	Strato
Fisher	3	1795 – 1830	$6407.0 \pm 5017.0$	Strato
Gareloi	9	1873 – 1989	$5301.9 \pm 2219.3$	Strato
Kiska	4	1962 – 1990	$3451.7 \pm 2088.0$	Strato
Korovin	6	1987 – 2006	$1441.2 \pm 692.2$	Strato
Okmok	16	1805 – 2008	$4943.7 \pm 1317.9$	Shield
Seguam	6	1891 – 1993	$7413.6 \pm 5081.9$	Strato
Shishaldin	23	1922 – 1999	$1268.6 \pm 275.7$	Strato
Vsevidof	3	1817 – 1878	$11140.0 \pm 6392.0$	Strato
Westdahl	7	1795 – 1991	$11956.3 \pm 7680.4$	Strato

Table A.3: Summary of the data used for the Aleutian islands with the number of eruptions, the time span, the mean interevent time and the type of volcano.

Volcano (region)	#eruptions	time span	$\tau_n$ [days]	volcano type
Acatenango (Guatemala)	3	1924 – 1972	$8748.0 \pm 8157.0$	Strato
Atitlan (Guatemala)	7	1826 – 1853	$1613.3 \pm 543.6$	Strato
Cerro Negro (Nicaragua)	23	1850 – 1999	$2478.9 \pm 658.3$	Cinder cones
Colima (Mexico)	51	1519 – 1997	$3494.6 \pm 708.7$	Strato
Concepcion (Nicaragua)	31	1883 – 2009	$1542.4 \pm 234.4$	Strato
Cosiguina (Nicaragua)	3	1835 – 1859	$4491.5 \pm 2033.5$	Strato
Fuego (Guatemala)	23	1880 – 2002	$2017.5 \pm 630.6$	Strato
Izalco (El Salvador)	48	1770 – 1937	$1300.5 \pm 166.4$	Strato
Masaya (Nicaragua)	26	1852 – 2008	$2279.8 \pm 718.9$	Caldera
Momotombo (Nicaragua)	12	1736 – 1905	$5596.3 \pm 2688.1$	Strato
Pacaya (Guatemala)	9	1846 – 2004	$7234.6 \pm 3513.0$	Complex
Pico de Orizaba (Mexico)	6	1545 – 1846	$21987.6 \pm 10010.1$	Strato
Poas (Costa Rica)	44	1880 – 2009	$1098.6 \pm 163.5$	Strato
Popocatepetl (Mexico)	10	1919 – 2005	$3485.7 \pm 1797.0$	Strato
Rincon de la Vieja (Costa Rica)	13	1922 – 1998	$2308.7 \pm 1317.5$	Complex
San Cristobal (Nicaragua)	13	1997 – 2010	$413.2 \pm 61.7$	Strato
San Miguel (El Salvador)	31	1510 – 2002	$5984.5 \pm 2340.0$	Strato
San Salvador (El Salvador)	4	1572 – 1917	$41994.7 \pm 25128.0$	Strato
Santa Ana (El Salvador)	8	1722 – 2005	$14780.0 \pm 7774.5$	Strato
Santa Maria (Guatemala)	3	1902 – 1922	$3590.5 \pm 3340.5$	Strato
Tacana (Mexico)	3	1878 – 1986	$19648.0 \pm 6458.0$	Strato
Telica (Nicaragua)	32	1927 – 2008	$953.5 \pm 156.4$	Strato

Table A.4: Summary of the data used for Central America with the number of eruptions, the time span, the mean interevent time and the type of volcano.

Volcano	#eruptions	time span	$\tau_n$ [days]	volcano type
Askja	9	1875 – 1961	$3963.6 \pm 2027.9$	Strato
Hekla	16	1510 – 2000	$11921.3 \pm 1920.9$	Strato
Katla	9	1580 – 1918	$8643.0 \pm 7534.2$	Subglacial
Krafla	12	1724 – 1984	$15439.1 \pm 2364.14$	Caldera
Kverkfjoll	6	1655 – 1968	$22871.8 \pm 13325.6$	Strato
Vestmannaeyjar	4	1637 – 1973	$40823.33 \pm 27558.7$	Submarine

Table A.5: Summary of the data used for Iceland with the number of eruptions, the time span, the mean interevent time and the type of volcano.

Volcano	#eruptions	time span	$\tau_n$ [days]	volcano type
Agung	3	1808 – 1963	$28239.5 \pm 15456.5$	Strato
Batur	26	1804 – 1999	$2844.6 \pm 810.5$	Caldera
Bur Ni Telong	5	1837 – 1937	$9109.5 \pm 4910.4$	Strato
Cereme	6	1698 – 1951	$18486.2 \pm 8695.7$	Strato
Dempo	27	1817 – 2009	$2683.2 \pm 572.1$	Strato
Dieng Volcanic Complex	21	1786 – 2009	$4076.85 \pm 1093.5$	Complex
Egon	4	2004 – 2008	$512.7 \pm 326.2$	Strato
Galunggung	5	1822 – 1984	$14724.3 \pm 6069.8$	Strato
Gede	20	1832 – 1957	$2394.0 \pm 748.1$	Strato
Guntur	21	1800 – 1847	$863.7 \pm 143.2$	Complex
Ijen	8	1796 – 1999	$10591.4 \pm 4685.3$	Strato
Iliboleng	20	1885 – 1993	$2071.3 \pm 569.7$	Strato
Iliwerung	12	1870 – 1999	$4279.6 \pm 1352.3$	Complex
Kaba	11	1833 – 2000	$6090.2 \pm 1776.9$	Strato
Kelut	21	1716 – 2007	$5317.9 \pm 932.3$	Strato
Kerinci	30	1838 – 2009	$2150.6 \pm 531.5$	Strato
Krakatau	41	1883 – 2010	$1163.6 \pm 400.7$	Caldera
Lamongan	41	1799 – 1898	$900.3 \pm 124.5$	Strato
Lewotobi	21	1861 – 2003	$2594.5 \pm 666.0$	Strato
Lewotolo	7	1819 – 1951	$8063.2 \pm 1876.5$	Strato
Papandayan	4	1772 – 2002	$28032.0 \pm 14152.0$	Strato
Perbakti Gagak	6	1923 – 1939	$1157.6 \pm 434.14$	Strato
Peuet Sague	7	1918 – 2000	$5021.3 \pm 3472.3$	Complex
Raung	55	1815 – 2008	$1301.7 \pm 216.8$	Strato
Rinjani	15	1847 – 2009	$4217.1 \pm 1144.2$	Strato
Salak	5	1780 – 1938	$14389.0 \pm 10121.8$	Strato
Sirung	8	1934 – 1970	$1880.9 \pm 566.2$	Complex
Slamet	41	1772 – 2009	$2161.3 \pm 527.8$	Strato
Sorikmarapi	5	1892 – 1986	$8594.3 \pm 4024.9$	Strato
Sundoro	9	1806 – 1971	$7548.1 \pm 3543.2$	Strato
Talang	13	1833 – 2007	$5300.8 \pm 2705.9$	Strato
Tangkubanparahu	16	1826 – 1983	$3821.1 \pm 1210.3$	Strato
Tandikat	3	1889 – 1924	$6412.0 \pm 2819.0$	Strato
Tengger	58	1804 – 2010	$1321.5 \pm 174.1$	Strato

Table A.6: Summary of the data used for Indonesia with the number of eruptions, the time span, the mean interevent time and the type of volcano.



Volcano	#eruptions	time span	$\tau_n$ [days]	volcano type
Adatarara	3	1899 – 1996	$17718.5 \pm 17391.5$	Strato
Akita Komaga Take	4	1890 – 1970	$9715.0 \pm 2873.0$	Strato
Akita Yake Yama	11	1867 – 1997	$4752.8 \pm 1814.2$	Strato
Chokai	4	1800 – 1974	$21092.3 \pm 14975.9$	Strato
Iwo Tori Shima	8	1796 – 1968	$8963.7 \pm 2616.5$	Complex
Kikai	9	1934 – 2004	$3171.3 \pm 2396.6$	Caldera
Kirishima	55	1524 – 2010	$3285.5 \pm 613.3$	Shield
Kuchinoerabu Jima	13	1840 – 1980	$4268.6 \pm 2148.4$	Strato
Kurikoma	5	1726 – 1950	$20411.8 \pm 17689.9$	Strato
Kusatsu Shirane	19	1882 – 1983	$2048.8 \pm 585.3$	Strato
Nasu	5	1846 – 1963	$10711.0 \pm 5838.7$	Strato
Niigata Yake Yama	12	1852 – 1998	$4829.1 \pm 3014.6$	Lava dome
Nikko Shirane	5	1872 – 1952	$7316.8 \pm 5274.2$	Shield
Sakura Jima	30	1468 – 1955	$6137.1 \pm 2214.1$	Strato
Suwanose Jima	18	1921 – 2004	$1780.6 \pm 526.1$	Strato
Unzen	5	1663 – 1996	$30393.8 \pm 17725.8$	Complex
Yake Dake	26	1907 – 1995	$1273.7 \pm 548.8$	Strato
Zao	25	1620 – 1896	$4195.5 \pm 1579.8$	Complex

Table A.7: Summary of the data used for Japan with the number of eruptions, the time span, the mean interevent time and the type of volcano.

Volcano	#eruptions	time span	$\tau_n$ [days]	volcano type
Avachinsky	19	1737 – 2001	$5360.5 \pm 1283.4$	Strato
Bezymianny	53	1955 – 2010	$386.9 \pm 54.0$	Strato
Gorely	11	1828 – 2010	$6647.5 \pm 2188.5$	Caldera
Karymsky	32	1771 – 2001	$2714.3 \pm 932.8$	Strato
Kliuchevskoi	99	1697 – 2009	$1163.1 \pm 156.0$	Strato
Koryaksky	3	1926 – 2008	$14976.0 \pm 4039.0$	Strato
Maly Semiachik	5	1804 – 1952	$13553.25 \pm 7812.1$	Caldera
Mutnovsky	18	1848 – 2000	$3265.7 \pm 1174.5$	Complex
Shiveluch	19	1854 – 1999	$2952.1 \pm 756.6$	Strato
Tolbachik	24	1904 – 1975	$1127.4 \pm 418.8$	Shield
Zhupanovsky	6	1882 – 1959	$5624.6 \pm 2689.4$	Compound volcano

Table A.8: Summary of the data used for Kamchatka with the number of eruptions, the time span, the mean interevent time and the type of volcano.

Volcano	#eruptions	time span	$\tau_n$ [days]	volcano type
Okataina	21	1886 – 1981	$1732.9 \pm 549.8$	Lava dome
Ruapehu	58	1861 – 2007	$937.8 \pm 206.0$	Strato
Tongariro	68	1839 – 1977	$754.6 \pm 96.4$	Strato
White Island	28	1909 – 2001	$1241.5 \pm 256.7$	Strato

Table A.9: Summary of the data used for New Zealand with the number of eruptions, the time span, the mean interevent time and the type of volcano.

Volcano (region)	#eruptions	time span	$\tau_n$ [days]	volcano type
Calbuco (Chile)	12	1893 – 1972	$2644.1 \pm 604.2$	Strato
Carran-los Venados (Chile)	3	1907 – 1979	$13151.5 \pm 4489.5$	Pyroclastic cones
Cerro Azul (Chile)	8	1906 – 1967	$3188.4 \pm 1086.9$	Strato
Cerro Azul (Galapagos)	10	1932 – 2008	$3080.7 \pm 850.8$	Shield
Cerro Hudson (Chile)	4	1740 – 1991	$30571.0 \pm 13828.6$	Strato
Copahue (Chile/Argentina)	9	1867 – 2000	$6072.3 \pm 3082.6$	Strato
Cotopaxi (Ecuador)	58	1532 – 1940	$2612.0 \pm 1108.1$	Strato
Fernandina (Galapagos)	22	1819 – 2009	$3300.7 \pm 940.4$	Shield
Galeras (Colombia)	29	1535 – 2010	$6198.1 \pm 1335.7$	Complex
Guagua Pichincha (Ecuador)	18	1582 – 2002	$9031.2 \pm 4213.4$	Strato
Guallatiri (Chile)	3	1913 – 1960	$8660.5 \pm 8154.5$	Strato
Huequi (Chile)	6	1890 – 1920	$2191.4 \pm 757.5$	Strato
Isluga (Chile)	7	1863 – 1913	$3038.5 \pm 1508.8$	Strato
Lascar (Chile)	27	1848 – 2006	$2216.7 \pm 508.9$	Strato
Lautaro (Chile)	9	1876 – 1979	$4676.5 \pm 2230.5$	Strato
Llaima (Chile)	53	1640 – 2008	$2584.2 \pm 884.7$	Strato
Llullaillaco (Chile/Argentina)	3	1854 – 1877	$4240.5 \pm 1076.5$	Strato
Lonquimay (Chile)	4	1853 – 1988	$16545.0 \pm 2282.6$	Strato
Minchinmavida (Chile)	3	1742 – 1835	$16918.0 \pm 16831.0$	Strato
Nevado del Huila (Colombia)	3	2007 – 2008	$307.5 \pm 9.5$	Strato
Nevado del Ruiz (Colombia)	8	1805 – 1985	$9417.9 \pm 4313.6$	Strato
Nevado del Tolima (Colombia)	4	1822 – 1943	$14649.5 \pm 14011.7$	Strato
Planchon-Peteroa (Chile)	10	1878 – 2010	$5364.3 \pm 1899.5$	Strato
Purace (Colombia)	23	1816 – 1977	$2668.2 \pm 484.2$	Strato
Puyehue-Cordon Caulle (Chile)	11	1759 – 2011	$9201.4 \pm 4550.6$	Strato
Reventador (Ecuador)	28	1541 – 2008	$6321.7 \pm 1649.5$	Strato
Sabancaya (Peru)	7	1750 – 2003	$15405.8 \pm 11848.0$	Strato
Sangay (Ecuador)	3	1628 – 1934	$55854.5 \pm 19331.5$	Strato
San Jose (Chile/Argentina)	7	1822 – 1960	$8377.2 \pm 3732.8$	Strato
Sierra Negra (Galapagos)	12	1813 – 2005	$6384.4 \pm 1791.4$	Shield
Tupungatito (Chile/Argentina)	16	1889 – 1987	$2396.2 \pm 604.7$	Strato
Ubinas (Peru)	16	1662 – 2006	$8369.7 \pm 2627.7$	Strato
Wolf (Galapagos)	9	1797 – 1982	$8449.5 \pm 5356.3$	Shield
Yucamane (Peru)	5	1780 – 1902	$11132.0 \pm 4429.2$	Strato

Table A.10: Summary of the data used for South America with the number of eruptions, the time span, the mean interevent time and the type of volcano.

Volcano	#eruptions	time span	$\tau_n$ [days]
Acigol Nevsehir	6	7810 BC – 2080 BC	$523209.8 \pm 185702.2$
Aniakchak	13	5250 BC – 1931	$218562.1 \pm 79540.8$
Batur	26	1804 – 1999	$2844.6 \pm 810.5$
Campi Flegrei	20	8480 BC – 1538	$192583.6 \pm 79317.0$
Chacana	5	8050 BC – 1773	$896944.5 \pm 509545.6$
Crater Lake	5	5900 BC – 2850 BC	$278497.3 \pm 199780.0$
Cuicocha	4	2550 BC – 650	$389592.0 \pm 159670.6$
Gorely	11	1828 – 2010	$6647.5 \pm 2188.5$
Kikai	9	1934 – 2004	$3171.3 \pm 2396.6$
Krakatau	41	1883 – 2010	$1163.6 \pm 400.7$
Krashenninnikov	31	8050 BC – 1550	$116877.6 \pm 16230.6$
Kutcharo	6	5800 BC – 1320	$520105.4 \pm 149939.1$
Maly Semiachik	5	1804 – 1952	$13553.25 \pm 7812.1$
Masaya	26	1852 – 2008	$2279.8 \pm 718.9$
Mashu	7	5550 BC – 1080	$403593.0 \pm 119506.6$
Narugo	5	4400 BC – 837	$478185.0 \pm 238765.4$
Nemo Peak	11	7550 BC – 1938	$346546.2 \pm 86916.2$
Opala	4	3500 BC – 1776	$642378.0 \pm 110437.3$
Pululagua	4	4800 BC – 290	$619694.7 \pm 443867.5$
Towada	8	9490 BC – 915	$542906.9 \pm 124161.2$
Yellowstone	4	7400 BC – 1350 BC	$736572.3 \pm 183330.3$

Table A.11: Summary of the data used for the eruption of major calderas on Earth with the number of eruptions, the time span and the mean interevent time.

## Appendix B Curriculum Vitae

### Publications:

Sanchez, L. and Shcherbakov, R. (2012), Scaling properties of planetary calderas and terrestrial volcanic eruptions, *Nonlinear Proc. in Geoph.*, 19(6):585-593

Sanchez, L. and Shcherbakov, R. (2014), Statistical Analysis of the Size Distribution of Impact Craters, *submitted to Earth and Planetary Science Letters*

Sanchez, L. and Shcherbakov, R. (2012), Temporal Scaling of Volcanic Eruptions *J. Volcanol. Geotherm. Res.*, 247-248:115121, 2012.

### Conference Presentations:

Sanchez, L. and Shcherbakov, R., (2013) *Modeling the statistical behavior of volcanic eruptions using a cellular automaton*, EGU General Assembly, April 2013, Vienna.

Sanchez L., Shcherbakov R., (2012), *A cellular automaton to model magma/crust interactions and volcanic eruptions*, AGU Fall meeting, December 2012, San Francisco

Sanchez L., Shcherbakov R., (2011), *Lattice gas cellular automaton to model volcanic eruptions*, AGU Fall meeting, December 2011, San Francisco

Sanchez L., Shcherbakov R., (2010), *Statistical analysis of planetary calderas terrestrial volcanic eruptions*, AGU Fall meeting, December 2010, San Francisco

Sanchez L., Scanlan K., Shcherbakov R., (2010), *Statistical analysis of terrestrial and planetary volcanoes*, CGU annual meeting, June 2010, Ottawa

---

**Name:** Laura Sanchez

**Post-Secondary Education and Degrees:** University Joseph Fourier  
Grenoble, France  
2003 - 2006 B.Sc.

University Joseph Fourier  
Grenoble, France  
2006 - 2008 M.Sc.

University of Western Ontario  
London, ON  
2009 - 2014 PhD

**Honours and Awards:** Ontario Graduate Scholarship  
2012-2013

Graduate Thesis Research Fund  
2013

Best Student Paper Award, AGU  
2011

Geophysics Travel Scholarship  
2010-2011

**Related Work Experience:** Course Instructor  
The University of Western Ontario  
Fall 2013

Teaching Assistant  
The University of Western Ontario  
2009 - 2013